12-2016

Defects in Graphene: Electrochemical, Magnetic, and Optical Properties

Jingyi Zhu
Clemson University, jzhu2@g.clemson.edu

DEFECTS IN GRAPHENE: ELECTROCHEMICAL, MAGNETIC, AND OPTICAL PROPERTIES

A Dissertation
Presented to
the Graduate School of
Clemson University

In Partial Fulfillment
of the Requirements for the Degree
Doctor of Philosophy
Physics

---

by
Jingyi Zhu
December 2016

Accepted by:
Dr. Apparao M. Rao, Committee Chair
Dr. Jian He
Dr. Shiou-Jyh Hwu
Dr. Mark E. Roberts

ABSTRACT

Graphene has attracted tremendous attention due to its unique properties, such as its two-dimensional structure, zero-band-gap, and linear dispersion relation of its electronic band structure, which are all very interesting from a fundamental standpoint. In addition, its ultra-light weight, high surface area, exceptional electrical and thermal conductivities, as well as robust mechanical strength portends huge potential in diverse applications. Defects in the otherwise perfectly hexagonal lattice of graphene lead to lattice symmetry breaking, and the emergence of new fundamental properties of graphene. Therefore, to understand the role of defects in graphene and further to control the fundamental characteristics of graphene through quantity and configuration of defects (or defect-engineering), it is essential to develop effective synthesis methods. This thesis describes such synthesis methods and the role of controlled defects on the electrochemical, magnetic, as well as the optical properties of graphene.

Following the first two introductory Chapters, in Chapter 3 I describe the effects of vacancies and dopants on the electrochemical properties of graphene. Carbon is an excellent electrode material in high-energy and high-power density supercapacitors (SCs) due to its economic viability, high-surface area, and high stability. Although graphene has high theoretical surface area, and hence high double layer capacitance, the net amount of energy stored in graphene-SCs is much below the theoretical limits due to two inherent bottlenecks: i) their low quantum capacitance, and ii) limited ion-accessible surface area. We demonstrate that properly designed defects in graphene effectively mitigates these

bottlenecks by drastically increasing the quantum capacitance and opening new channels to facilitate ion diffusion in the otherwise inaccessible interlayer gallery space in few layer graphene. Our results support the emergence of a new energy paradigm in SCs with 150% enhancement in double layer capacitance beyond the theoretical limit. Furthermore, we demonstrate defect engineering in graphene foams as an example of prototype bulk SCs with energy densities of 500% higher than the state-of-the-art commercial SCs without compromising the power density.

Chapter 4 focuses on the magnetic properties of graphene when a dopant, such as a sulfur atom, is incorporated into the hexagonal framework of graphene. Bulk graphite is diamagnetic in nature, however, graphene is known to exhibit either a paramagnetic response or weak ferromagnetic ordering. Although many groups have attributed this magnetism in graphene to defects or presence of unintentional magnetic impurities, compelling evidence to pinpoint origin of magnetism in graphene was lacking. To address this issue, we systematically studied the influence of entropically necessary intrinsic defects (e.g., vacancies, edges) and extrinsic dopants (e.g., S-dopants) on the magnetic properties of graphene. We found that the saturation magnetization of graphene decreased upon sulfur doping suggesting that S-dopants demagnetized vacancies and edges. Our density functional theory calculations provided evidence for: i) intrinsic defect demagnetization by the formation of covalent bonds between S-dopant and edges/vacancies concurring with the experimental results, and ii) a net magnetization from only zig-zag edges, suggesting that the contradictory conclusions on graphene magnetism reported in the literature may stem from the magnetic properties due to different defect-

types. Interestingly, we observed peculiar local maxima in the temperature dependent magnetizations that suggest the coexistence of different magnetic phases within the same graphene samples.

Finally, in Chapter 5, we demonstrated the relation between defects in graphene and a Raman feature – the so-called *G** band which is present at 2450 cm^{-1}. Although most of the prominent Raman features in graphene are well understood within the double resonance (DR) picture, the origin of the *G** band still remains unclear. We performed detailed Raman studies of mechanically exfoliated and chemical vapor deposited single- and few-layer graphene using multiple laser excitations to unravel the origin of *G** band. Our study concludes that the *G** band arises from a combination of transverse optical (*iTO*) and longitudinal acoustic (*LA*) phonons, and its asymmetric lineshape is due to the presence of two different time-order phonon processes. As detailed in Chapter 5, we attribute the lower (/higher) frequency sub-peak to an *LA*-first (/*iTO*-first) process. Such time-ordered processes are necessary to rationalize the dispersion of the *G** band sub-peak frequencies with respect to the excitation energy. Our study also shows that defects in graphene induce new scattering channels and thereby weaken both the time-ordered combination modes. Finally, we also discuss that the effect of layer stacking on the structure of the *G** band and attribute its increasing asymmetry to multiple processes between electronic sub-bands, similar to the physics that is responsible for the *G'* band in multi-layer graphene.

DEDICATION

I dedicate my work to the memories of my dearest mom, Wenfeng Zhu, for bringing me to the world, for the moral, intellectual and physical education she has given me, for her unconditional love, support, and all the things she has done for me throughout my life.

I dedicate this work to my beloved father, Xisheng Dai, without whose encouragement and support none of my success would be possible.

I also dedicate this work to my fiancé, Min Zhang and his family for their understanding and accompanying during all my difficult times. I would like to take this opportunity to extend my sincere gratitude towards all my family and friends for their help and guidance.

ACKNOWLEDGEMENTS

I would like to express my sincere appreciation to my advisor, Dr. Apparao M. Rao, for providing me the great opportunity of working in his research group. His inspiration, guidance and encouragement has motivated me to overcome all the obstacles and accomplish my goal in these years. It would be impossible to complete this thesis without the insights and motivations from Dr. Ramakrishna Podila. I cannot count that how many discussions we've had for designing the experiments, analyzing the results and editing the manuscripts. I thank Dr. Jian He and Dr, Rahul Rao, for their valuable guidance and input on the magnetic and the Raman spectroscopy projects. Thanks for Dr. Malcolm Skove for his suggestions on my research, oral presentations and English writing. Also, I would like to thank the group of Dr. Mark Roberts for their help and collaboration on the electrochemistry porjects. I express my gratitude to the group of Dr. Anurag Srivastava (ABV-Indian Institute of Information Technology and Management), the group of Dr. John Wilkins (Ohio State University), the group of Dr. Anvar Zakhidov (The University of Texas at Dallas), Dr. Paola Ayala, and Dr. Ye Lin for their collaborations on theoretical calculations and sample measurements. Many thanks to my dissertation committee members Dr. Shiou-Jyh Hwu, Dr. Jian He, and Dr. Mark Roberts.

I would not have completed this dissertation without the support of my colleagues: Drs. Mehmet Karakaya, Deepika Saini and Sriparna Bhattacharya for their introduction and help of the equipments, techniques and material synthesis, Anthony Childress for his important help of sample preparation, and all my present and past lab mates at Clemson

Nanomaterials Institute (Herbert Behlow, Lakshman Ventrapragada, Yongchang Dong, Sai Mallineni, Fengjiao Liu, Achyut Raghavendra, Wren Gregory, Bishwambhar Senguptafor, Longyu Hu, Xueying Ge, Prakash Parajuli and Joseph Denison) for their encouragement and support.

I have to appreciate my aunts – Qingqiu Dai and Wennan Zhu, my uncle – Jingsheng Dai, my cousins – Hui Jin, Xing Jin, Zhenhao Hou, Xiaofeng Chen, Zhengyue Dai and their families. My gratitude to them for taking great care of my parents, for being always treating me as their child or sister, for their endless help and encouragements. I am always feeling be loved and getting spiritual support from all of you.

Finally, I would like to thank all my friends in China and US. Thank to my best friend Dr. Xueyan He for her encouragement during my PhD life. Particularly, thanks to my roommate Yamin Liu and her parents, Song and Milan, Tianhong, Yang Gao, Lin Li and Dan Du, Tianwei and Shasha, Menghan and Yufei, Zhe Zhang, Lin Wang, Xiaoyu (Bella), Fanchen, Yamei and Chuanchang for making my life in Clemson memorable.

TABLE OF CONTENTS

Table of Contents (Continued)

Page

Table of Contents (Continued)

Page

LIST OF TABLES

LIST OF FIGURES

List of Figures (Continued)

Figure Page

List of Figures (Continued)

Figure Page

List of Figures (Continued)

Figure Page

List of Figures (Continued)

Figure Page

List of Figures (Continued)

Figure Page

List of Figures (Continued)

Figure Page

List of Figures (Continued)

Figure Page

List of Figures (Continued)

Figure Page

List of Figures (Continued)

Figure Page

CHAPTER 1

DEFECTS IN GRAPHENE

Carbon nanomaterials, such as graphene, have attracted tremendous attention since their discovery. Garphene‘s unique properties, such as its one atom thickness, two-dimensional (2D) structure, zero energy band-gap, and the linear dispersion of its electronic band structure makes it a fundamentally important material. In addition, its ultra-light weight, high surface area per unit mass, exceptional electrical and thermal conductivities, as well as robust mechanical strength which stems from its covlent bonds makes graphene an ideal material for diverse applications. Several synthesis techniques have been reported for the growth of graphene, which include mechanical exfoliation, electric arc discharge, pulsed laser deposition, chemical exfoliation, chemical vapor deposition, etc. Usually, as-synthesized graphene contain defects, which lead to symmetry breaking and the emeregence of graphene’s novel electronic, magnetic and transport properties. For example, substitutional chemical doping is one way of introducing an electronic bandgap in otherwise semimetallic graphene. Therefore, tuning the fundamental properties of graphene by controlling the quantity and configuration of its defects, or in other words defect-engineering, is a growing research topic in carbon science and engineering. In this chapter, I briefly describe the structure-property relation in graphene in the presence and absence of defects, followed with an overview of the synthesis method to elucidate how controlled defects can be incorporated into the 2D lattice of graphene. A few applications and the limitation of graphene are also discussed.

1.1. Introduction to graphene

1.1.1. Structure of graphene

Elemental carbon has the unique ability to form covalently connected bulk and nanostructured materials with varying *sp* hybridized bonding states. While graphite and diamond represent the sp^2 and sp^3 hybridized bulk forms of carbon, carbon nanotubes and fullerenes represent nanostructured forms of carbon with intermediate hybridization sp^x, where $2 < x < 3$. Graphene, which is the most recent and widely studied form of nanostructured carbon, is a single sheet of carbon atoms that is isolated from the graphite bulk material. In other words, any of the shaded 2D sheets that compose graphite (**Fig. 1.1.1a**), when isolated from the bulk, acquire a new form, known as graphene (**Fig. 1.1.1b**). In each layer, the carbon atoms are sp^2 bonded and arranged in hexagonal lattice, as shown in **Fig. 1.1.1b**. The hexagonal lattice of graphene can be viewed as two inequivalent sublattices with two inequivalent atoms in a unit cell. Similar to graphite, in bi-layer or few layered graphene (BLG/FLG), the only force holding the layers together is the van der Waals force. In the in-plane hexagonal lattice the distance between neighboring carbon atoms is 1.42 Å.[1]

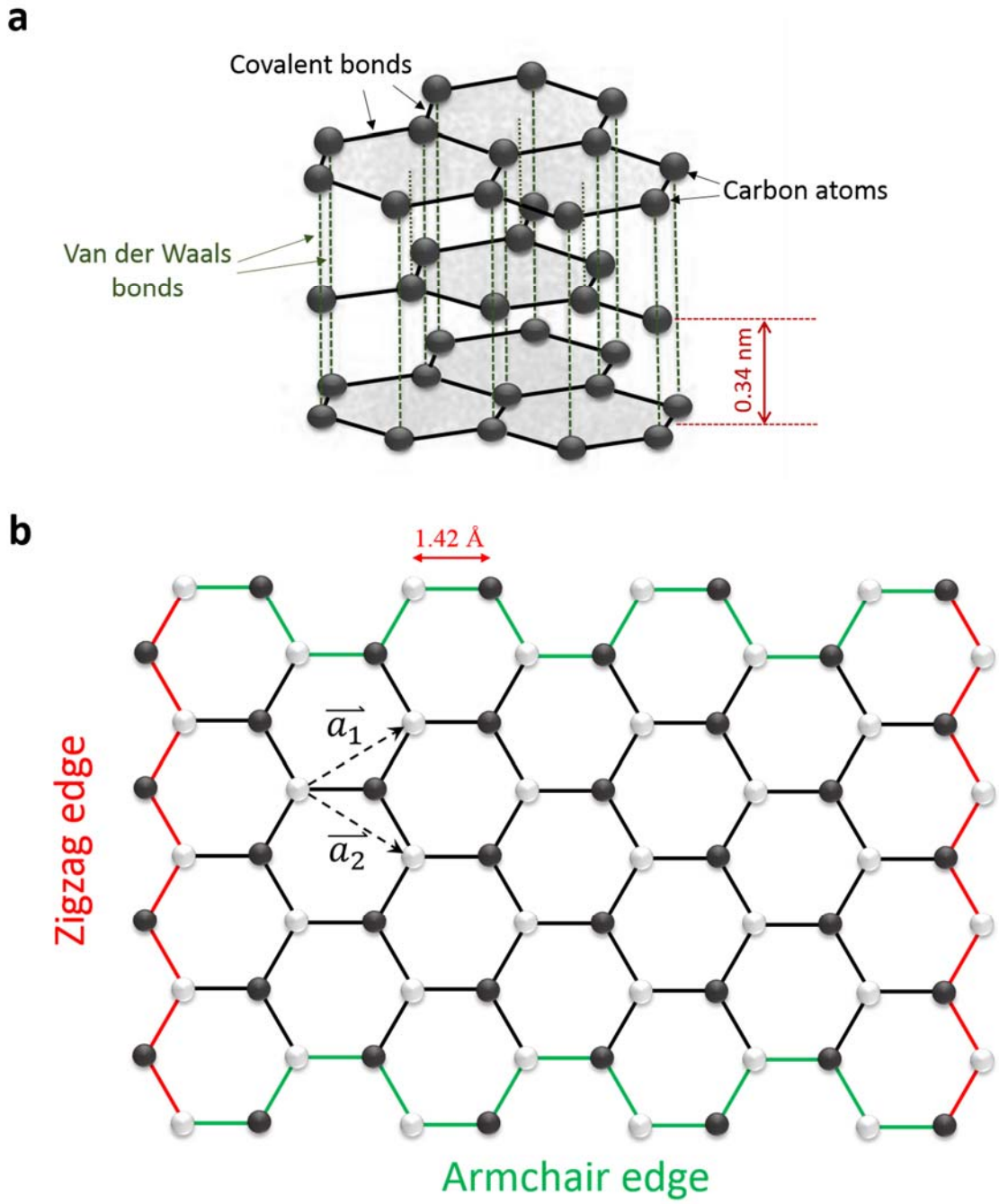

Figure 1.1.1: (a) Bulk graphite is composed of Van der Waals bonded graphene layers, and the black dots within each layer represent the carbon atoms. (b) The honeycomb lattice

of graphene. The grey and black colored dots represent the two inequivalent sublattices in the honeycomb lattice. The two unit vectors of graphene are represnted by the dash arrows. The top and bottom egdes represent the armchair edges (green), while the edges on the sides (red) represent the zigzag edges.

Each carbon atom in graphene forms three σ-bonds with its neighboring carbon atoms, which ensures graphene's high in-plane mechanical strength. The fourth bond of the carbon atom is a π-bond which is oriented perpendicular to the plane of graphene. The π-bonds hybridize together with σ-bonds into a sp^2 hybridized state and provide free electrons that move within the layer resulting in the excellent electron mobility of graphene.

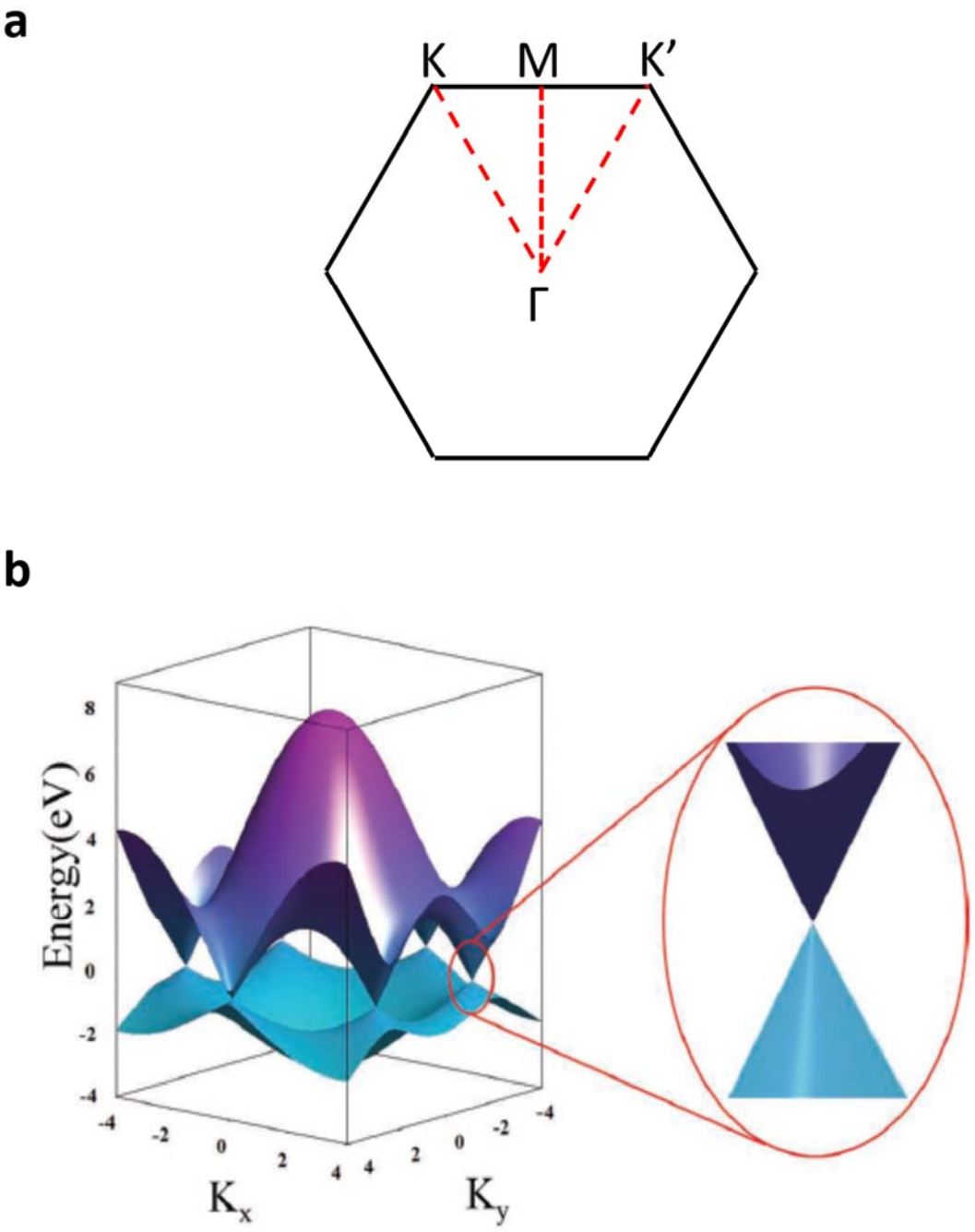

Figure 1.1.2: a) The first Brillouin zone of graphene. b) The electronic dispersion for graphene in the first Brillouin zone. [2]

The first Brillouin zone (BZ) of graphene is hexagonal (**Figure 1.1.2a**). At the corner it has two inequivalent points – *K* and *K*'. The *Γ* point denotes the center of the BZ, and the mid-point between the *K* and *K*' points is the *M* point. **Figure 1.1.2b** shows the electronic dispersion for graphene in the first BZ. Interestingly, its valence and conduction bands touch at the *K* and *K*' points, which makes graphene a semiconductor with a zero-band gap (or a semi-metal). In addition, unlike normal semiconductors, which usually exhibit a parabolic dispersion, graphene exhibits a linear energy band dispersion near the corners of its BZ (highlighted in **Figure 1.1.2b**). The linear dispersion leads to "massless" carriers in graphene, and results in an ultrahigh electron mobility.

1.1.2. Defects of graphene

Graphene is a host to several defects that are either intrinsic or extrinsic in nature. Intrinsic defects in graphene include the: i) Stone-Wales defect, which results from the lattice reconstruction and the formation of non-hexagonal rings in graphene, ii) vacancies, which arises from the removal of one or more carbon atoms from the honeycomb lattice, and iii) adatoms, by bonding extra carbon atoms to the lattice.[3] Usually vacancies and adatoms accompany locally reconstruction within the lattice. Irradiation with electrons or ions is effective for creating point defects in graphene.[4,5] Other types of intrinsic defects include the armchair and zigzag edges (cf. **Fig. 1.1.1**). Graphene when doped with foreign atoms such as N,[6,7] B,[7] S,[8] or F[9] results in the creation of extrinsic defects in graphene. In some cases, the dopant can be incorporated into the hexagonal lattice in

different configurations. For instance, N can be substitutionally doped in the so-called graphitic, pryridinic and pyrrolic configurations [10]. The defect configuration caused by the dopant can be controlled to some extent through the synthesis parameters. [10,11]

The presence of defects in graphene should not be viewed as a performance limiter. In general, the literature is replete with examples which demosntrate enhanced materials properties due ot the presence of specific defects. For example, specific types of dopants in graphene render it n-type or p-type characteristics. Therefore, to understanding the role of defects, and to elicit enhanced materials properties, synthesis methods to incorporate the right kind of defects in graphene are essential. In the following chapters, we will discuss the role of defects in graphene's electrochemical, magnetic and optical properties, and demonstrate how defect-engineered graphene are promoting practical applications.

1.2. Synthesis of graphene

Graphene was first synthesized in the lab by mechanically cleaving it from graphite flakes using the infamous Skotch tape method.[10] Since then, much progress has been achieved in the synthesis of single-layer graphene (SLG) as well as few-layer graphene (FLG). These synthesis methods include liquid phase exfoliation,[12] arc discharge,[13] reduction of graphene oxide,[14] and chemical vapor deposition (CVD). Among these methods, the mechanical cleavage method produces graphene with highest quality, and in Chapter 5 we will discuss their optical properties. However, the downside of the mechanical exfoliation method is its low productivity. On the other hand, owing to its

simplicity and high productivity, thermal CVD has been widely adopted for growing high quality graphene. Transition metal substrates such as Ni [15], Ru [16], and Cu [17] are ideal for the CVD growth of graphene. In the CVD method, the metal substrates are exposed to a hydrocarbon gas such as methane or acetylene. At high substrate temperatures (~ 1000 ^{o}C), the metal absorbs carbon upto its saturation point, which is typically less than 1 at.% at 1000 ^{o}C.[18,19] During the cooling cycle when the CVD reactor is turned off, the solubility of carbon in the metal substrate decreases, causing them to precipitate from the surface of the metal which forms a thin carbon layer, or graphene. Another advantage of CVD is the ease with which defects can be introduced into the honeycomb lattice of graphene during synthesis. In Chapter 3, I will discuss defect-engineered CVD grown graphene, and the role of defects in optimizing the electrochemcial properties of graphene for use as electrodes in energy storage devices.

Besides the CVD method, liquid phase exfoliation is another technique that is fairly simple and yields large quantity of graphene. In Chapter 4, I will describe the liquid exfoliation method and elucidate the effect of doping on the magnetic properties of graphene.

1.3. The use of graphene in energy storage devices

1.3.1. Supercapacitors

Supercapacitors (or ultracapacitors) are electrical energy storage devices, similar to batteries and capacitors. A conventional capacitor consists of two parallel conductive electrodes (usually metal) separate by a dielectric material, as shown in **Fig. 1.3.1a**. The capacitance of a conventional capacitor is calculated as:

$$C = \frac{\varepsilon A}{d}, \tag{1.1}$$

where A is the area of the conductive metal electrode, ε is the permittivity of the dielectric material, and d is the distance between the two electrodes, which usually equals to the thickness of the dielectric material. While batteries stores or release large amount of charge through chemical reactions, it takes a long time to charge or discharge them, and hence batteries deliver less power. Capacitors, on the other hand, could be charged at much higher rate as they store charge electrostatically, and thus are capable of delivering high power. However, capacitors store much less charge than present batteries.

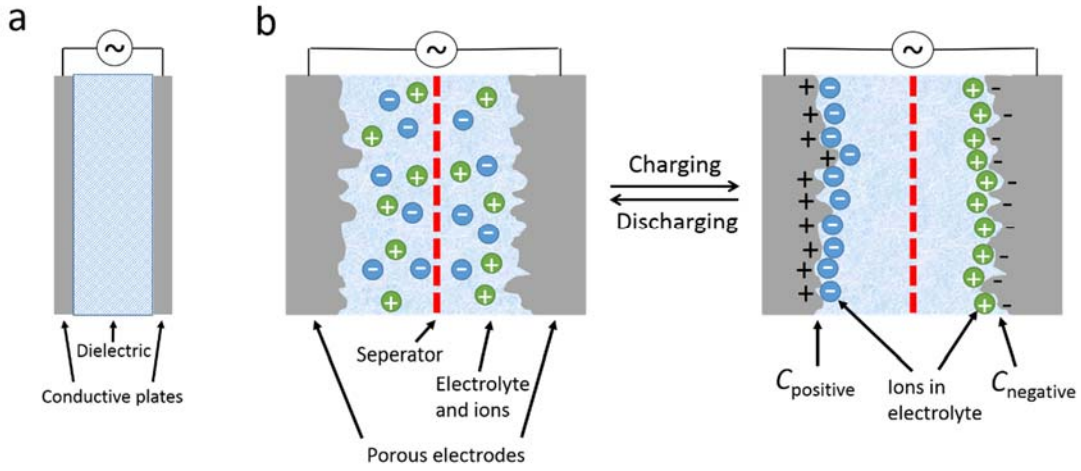

Figure 1.3.1: The schematic illustration of (a) conventional parallel plate capacitor, (b) the charging/discharging process in a supercapacitor.

Supercapacitors are different from parallel-plate capacitors. They consist of two conductive electrodes with electrolyte between them (instead of dielectric materials) as illustrated in **Fig. 1.3.1b**. An ion-permeable separator is usually placed in between the electrodes to prevent an electric short. When a voltage bias is applied to the electrodes, ions in the electrolyte move towards thr respective electrodes to form the electric double layers, i.e., the positive ions electrostatically adhere at the electrode/electrolyte interface of the negatively charged electrode, and *vise versa*. The total capacitance of the supercapacitor involves the capacitance of both electric double layers at the two electrodes, which forms two individual capacitors $C_{positive}$ and $C_{negative}$. Thus, the supercapacitors are also defined as an electrical double layer capacitor (EDLC), and the total capacitance is calculated as:

$$C_{total} = \frac{C_{\text{positive}} \cdot C_{\text{negative}}}{C_{\text{positive}} + C_{\text{negative}}} . \quad (1.2)$$

In the case of symmetric EDLC, C_{total} is usually half of the value of the capacitance on each electrode. Typically, the electrode materials of supercapacitors are highly porous, which provides more accessible surface area for ions and consequently have higher A in Eq. 1.1. In addition, due to the low d in each electrical double layer (~ diameter of ions), supercapacitors exhibits over 1000 times higher capacitance, and thus store much more charge than conventional capacitors.

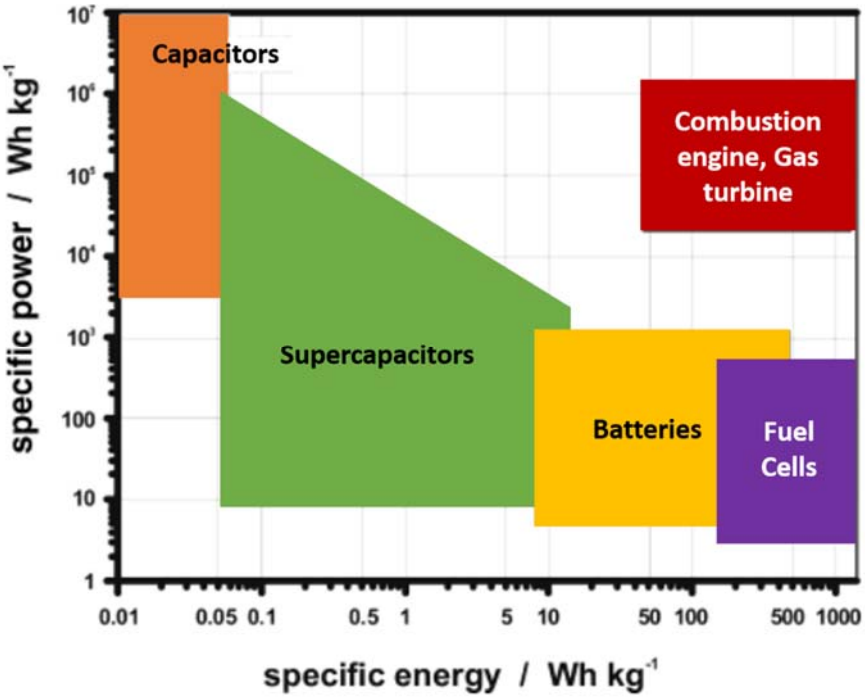

Figure 1.3.2: A Ragone plot of the specific energy and specific power densities of energy storage devices. The overarching goal is to increase both the energy density and power density of any of the storage device to match that of gasoline. [20]

In the Ragone plot (**Fig. 1.3.2**), it is clear that while supercapacitors exhibit higher energy density than capacitors, they also posses larger power density than batteries. Therefore, supercapacitors are energy storage devices that fill the gap between batteries and capacitors, and are attracting tremendous interest from researchers as well as industry.

1.3.2. Graphene as an ideal electrode material

Elemental carbon is the most suitable electrode material in supercapacitors because of its high specific surface area, light weight, good electric conductivity, and chemical stability. Many manifestations of carbon materials have been investigated as electrode materials for supercapacitors, e.g., activated carbon, carbon nanotubes, graphene, carbon fibres, etc. Because of its facile scalable production and highly porous structure, most supercapacitor manufacturers use electrodes made of activated carbon. The specific surface area of activated carbon usually ranges from 1000 – 2000 $m^2 g^{-1}$, allowing them to exhibit phenomenal electrical double layer capacitance.[21–24] However, the amorphous nature of activated carbon and the non-uniform pore size distribution (consist of micropores (<2 nm), mesopores (2–50 nm), and macropores (>50 nm)) leads to its poor electrical conductivity.[21,22] In addition, the need of an electrically conducting binder to coat activated carbon powders on to metal current collector (e.g., aluminum ribbons) results in a further increase in the internal resistance of the electrodes. Lastly, it should be noted that the microporisity (pore size < 2 nm), which lends high specific surface area to the activated

carbon, limits the number of ions from the electrolyte that can reach the metal electrode.[25] All of the above factors adversely affect the performance of activated carbon based electrodes in supercapacitors.

Graphene has a theoretical specific surface area ~ 2630 $m^2 g^{-1}$ as all atoms are on its surface, and can potentially yield a capacitance of 550 F g^{-1}. Owing to their high electrolyte accessibility, good electric conductivity and large specific surface area, graphene is considered as a promising electrode material for supercapacitors.[26]

1.3.3. Limitation of graphene in application of energy storage devices

One of the most important limitations of graphene comes from its limited electron density of states (DOS) at the Fermi level, which is related to a quantity called quantum capacitance (QC). Another limitation of graphene is its ion accessibility as explained below.

Quantum capacitance

The concept of QC was first introduced by Serge Luryi, who is an electrical engineer by profession.[27] The 2D transistor (**Fig. 1.3.3a)** in which the channel is a semiconductor can best explain the concept of QC. The two ends of the channel are electrically connected to the source and drain with the source being grounded and the drain held at a voltage V_D. The current I is measured as a function of V_D to determine the conductivity in the channel, and furthermore to derive the carrier concentration in the channel. In addition, a gate voltage V_G can be applied on top of the channel to tune the

Fermi level of the semiconductor (or the channel). Typically, an insulator is placed between the channel and the power supply (V_G) to ensure that no current flows across the insulator; V_G merely impresses a potential on the cairriers present in the channel. A positive V_G causes the conduction band minimum to be lowered by eV_G as shown in **Fig. 1.3.3b**. It is also equivalent to saying that the Fermi level (E_F) of the semiconductor is raised by the positive gate voltage.

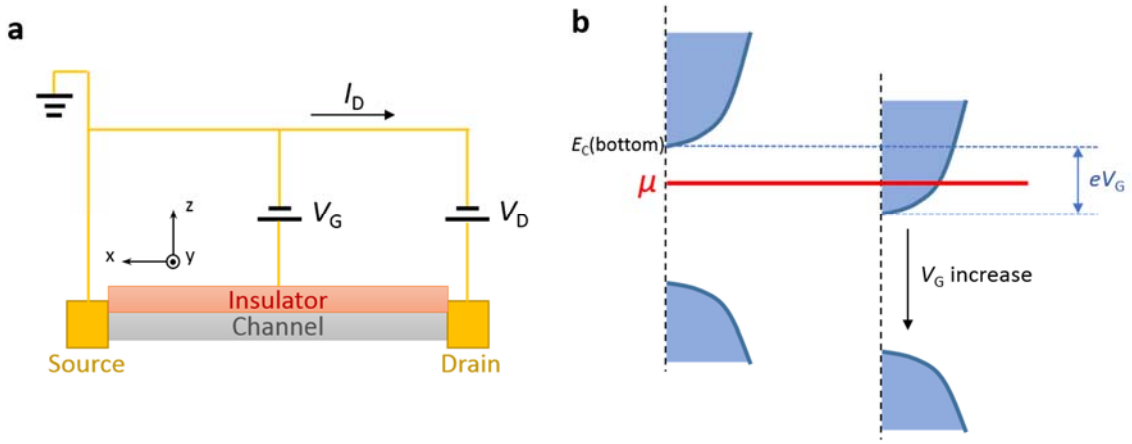

Figure 1.3.3: a) A schematic of a 2D transistor. b) A positive V_G causes the conduction band minimum to be lowered by eV_G.

Under this condition, the transistor conducts and if the thickness of the semiconductor is small (less than 10 nm), the electron motion is confined only in the x-y plane (2D electron gas) and the DOS of these electrons can be described as

$$\mathrm{DOS}(E) = \frac{m_e}{\pi\hbar^2}\,. \tag{1.3}$$

Here m_e refers to the effective mass of the electrons. The areal density of the electrons in the channel is

$$n = \int dE\mathrm{DOS}(E)f(E) = \frac{m_e}{\pi\hbar^2}\int_{E_c(bottom)}^{E} dEf(E)\,. \tag{1.4}$$

In Eq. 1.4, $E_c(bottom)$ is the energy at the conduction band minimum, E is the energy of the highest level to which electrons fill under a given V_G, and $f(E)$ is the Fermi-Dirac distribution function:

$$f(E) = \frac{1}{e^{\frac{E-\mu}{kT}}+1}\,. \tag{1.5}$$

Assume that $f(E)$ ~1 and combining Eqs. 1.4 and 1.5, we get:

$$n = \frac{m_e}{\pi\hbar^2}(\mu - (E_c(bottom) - eV_G))\,. \tag{1.6}$$

Therefore, it is expected that the areal electron density of the channel changes linearly with the gate voltage with a slope of

$$\frac{d(en)}{dV_G} = \frac{m_e}{\pi\hbar^2}e^2\,. \tag{1.7}$$

However, the experimentally observed slope, which represents a measure of how much the potential inside the channel changes for an applied gate voltage, is always lower than the value calculated from Eq. 1.7 (see **Fig. 1.3.4a**). The reason is because the channel is not an insulator since the Fermi level lies in the conduction band (cf. **Fig. 1.3.3b**), and to add an extra electron requires extra energy (called the charging energy) as there are a lot of electrons already present in the conduction band. Thus, the potential that is applied on the channel is not exactly equal to V_G, but less than V_G.

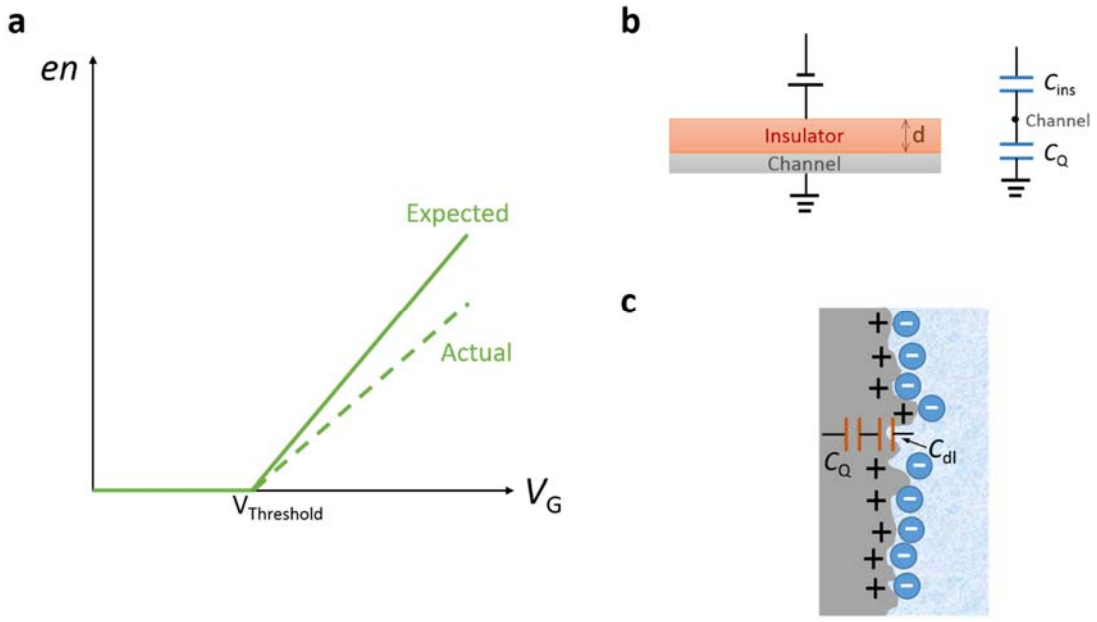

Figure 1.3.4: a) The expected and the actual dependence of the area charge density in the channel as a function of gate voltage. b) Schematic of the circuit that has quantum capacitance and the electrostatic capacitance connected in series. c) In EDLC the quantum capacitance and the double layer capacitance are connected in series.

Thus the reduced potential in the channel is due to the electrons present in the channel. In **Fig. 1.3.3a**, as an insulator is present above the channel, and the charge in the channel has induced a capacitor due to the insulator. The areal electrostatic capacitance C_{ins} across the insulator could be written in form of the parallel plate capacitor:

$$C_{ins} = \frac{\varepsilon}{d}, \tag{1.8}$$

where ε is of the dielectric constant of the insulator and d refers to the thickness of the insulating layer.

So the actual potential that is applied to the channel is:

$$V_c = V_G - \frac{ne}{C_{ins}} = V_G - \frac{ned}{\varepsilon}. \tag{1.9}$$

Therefore, we should replace the term V_G in Eq. 1.7, and consequently rewrite the equation of the slope:

$$\frac{d(en)}{dV_c} = \frac{m_e}{\pi\hbar^2} e^2 , \tag{1.10}$$

$$\frac{d(en)}{dV_G} = \frac{d(en)}{dV_c}\frac{dV_c}{dV_G}. \tag{1.11}$$

Combining Eqs. 1.10 and 1.11:

$$\frac{d(en)}{dV_G} = e^2 \frac{m_e}{\pi\hbar^2}\left(1 - \frac{1}{C_{ins}}\frac{d(en)}{dV_G}\right). \tag{1.12}$$

Define a quantity C_Q that:

$$C_Q = e^2 \frac{m_e}{\pi\hbar^2} = e^2 \mathrm{DOS}(E) \,. \tag{1.13}$$

We get the relation:

$$\frac{d(en)}{dV_G} = \frac{C_Q C_{ins}}{C_Q + C_{ins}} \,. \tag{1.14}$$

Clearly, $\frac{d(en)}{dV_G}$ has the dimensions of capacitance. Therefore, the system could be understand in a way that, the voltage V_G is applied on a capacitor with capacitance of $\frac{C_Q C_{ins}}{C_Q + C_{ins}}$, which is similar to a circuit with two capacitors with capacitance values C_Q and C_{ins} connected in series (see **Fig. 1.3.4b**), where C_Q is defined as the quantum capacitance. The portions of the voltage that are applied on the electrostatic capacitor and the quantum capacitance, depends on the ratio of C_{ins} to C_Q. According to Eq. 1.13, C_Q is proportional to DOS. When the channel has low DOS, C_Q is small and the corresponding impedance is high, resulting in a high voltage drop across C_Q, and *vice versa*.

In electrochemical systems, such as EDLCs and batteries, one can consider the total voltage V_{total} applied across the working electrode and the electrolyte as the gate voltage. Similar to the voltage applied on the electrostatic capacitance C_{ins}, only a portion of the voltage is applied at the surface of the electrode, between the electrons or holes in the electrode and the ions outside of the electrode. The quantum capacitance C_Q of the

electrode has taken away the rest part of the voltage. It could be also suitable to express the total capacitance of an electrode in the EDLC as follows:

$$C_{total} = \frac{C_Q C_{dl}}{C_Q + C_{dl}}. \quad (1.15)$$

Here C_{dl} is the double layer capacitance at the surface of the electrode. From Eq. 1.15 it is clear that a higher C_Q gives rise of higher C_{total}. Therefore, to achieve the maximum performance of an EDLC device, the voltage drop across the quantum capacitance C_Q is needed. Hence, it is expected that, a material with higher quantum capacitance C_Q, could be more suitable for the electrode in EDLC devices. However, as introduced previously, pristine graphene is a two dimentional, zero band gap semiconductor, with DOS equals to zero at its Fermi level. Hence, pristine graphene has a limited value of C_Q, which is considered as one of its bottlenecks for application in EDLCs. In Chapter 3, we will discuss the tuning of the DOS in graphene through methods of defect-engineering, such as introducing vacancies and doping, to improve the electrochemical performance of graphene.

Ion accessibility

For ease of synthesis, most graphene materials that are used in supercapacitors are FLG. The interlayer spacing in FLG is ~ 0.37 nm, which limits the accessibility of most kinds of ions. Therefore, although SLG has a high surface area ~ 2630 m^2g^{-1}, in FLG with average 5-6 layers, the area of ion accessible surface is reduced by more than 5 orders. The effective way to solve the limitation could be to *i*) find an optimized electrolyte whose ions

can readily access the interlayer spaces, or *ii*) create more pathways for the ions to enter into the interlayer spaces. Details of overcoming these limitations through defect-engineering is discussed in Chapter 3.

CHAPTER 2

CHARACTERIZATION TECHNIQUES

2.1. Electrochemistry Characterization

2.1.1. Potentiostat and electrochemistry cell setup

In this thesis, the electrochemisty characterizations were carried out by a Gamry Reference 3000AE potentiostat (**Fig. 2.1.1a**). Potentiostats are instruments which control the voltage difference between a working electrode and a reference electrode in the electrochemical cell by injecting current through the counter electrode. The potentiostat is attached to a electrochemical cell using working, working sense, counter, and reference electrode leads, in which the potential of the cell is measured between reference and working sense leads (see **Fig. 2.1.1b**). The current flow through the refernece and working sense electrodes are kept in minimum. The current flow through the cell is measured between the working and the counter electrodes.

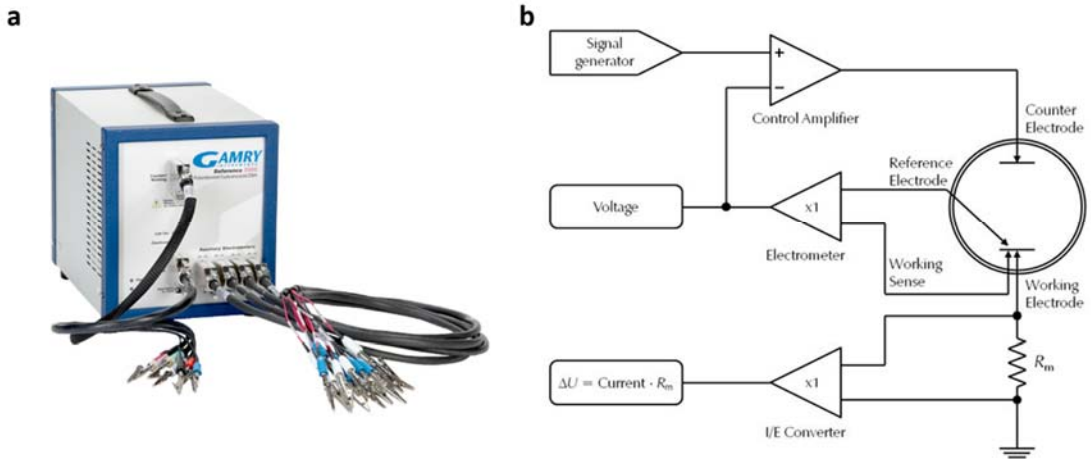

Figure 2.1.1: a) A picture of Gamry Reference 3000AE potentiostat. b) Simplified schematic of a potentiostat. (Figure source: Gamry instruments website)

A typical electrochemistry cell setup in electrochemistry measurements consists electrodes and electrolyte. The common designations for electrodes in the measurement are: working, reference and counter electrode. The working electrode is the electrode being studied in the experiment. The counter electrode is the other electrode which completes the current path in the cell. Reference electrodes serve as experimental potential reference. During the measurement, the reference electrodes should hold a constant potential.

The simplest cell setup is the two-electrode setup, in which the working current and sence leads in the potentiostat are connected to the working electrode, and the leads for reference and counter are connected together to the second electrode (**Fig. 2.1.2a**). A common EDLC device is a symmetric two-electrode cell, in which the two electrodes have same size, structure and electrochemistry properties.

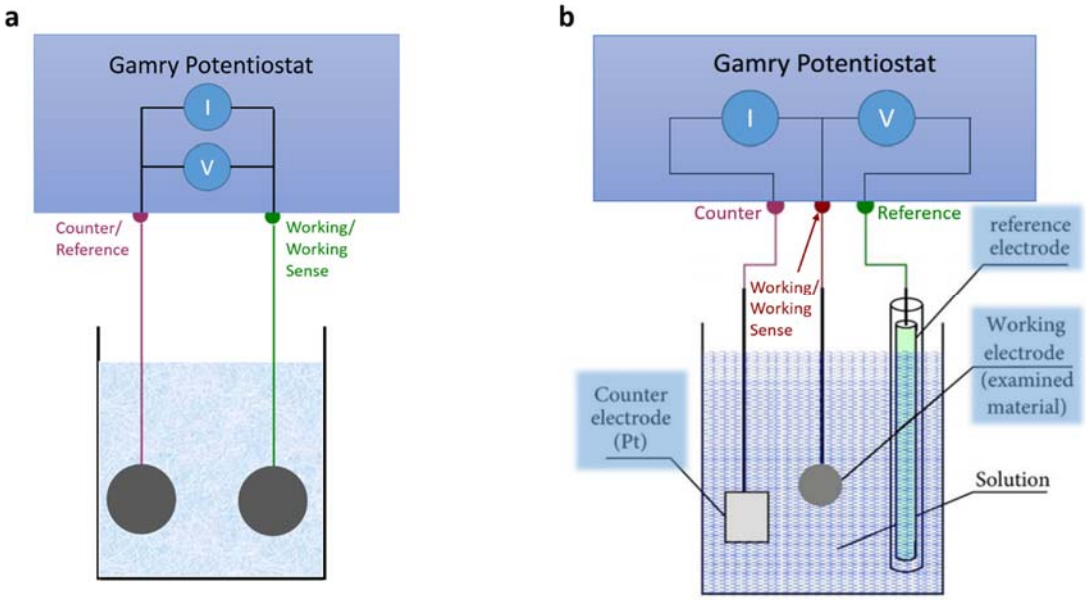

Figure 2.1.2: Schematics for a) two-electrode cell setup, b) three-electrode cell setup.

A two-electrode cell is good for measuring the performance of electrochemistry-energy devices, where the whole cell voltage is significant. However, for studying the electrochemical property of an electrode material, this cell setup has its limitations. In the two-electrode setup, there is a current flow through the counter electrode, which also serves as the reference, so it is not held at a constant potential and results in more complex data, and corresponding analysis. Therefore, a three-electrode setup is commonly utilized in electrochemistry characterizations.

In three-electrode cell setup, the Reference lead of the potentiostat is separated from the counter and connected to a standard reference electrode. The advantage of three-electrode setup is it measures the potential and current of half of the cell – only the working

electrode. **Figure 2.1.2b** shows the schematic of the three-electrode setup. The voltage of the working electrode is measured by a voltmeter in the potentiostat against the reference electrode, that is independent of the changes that may occurs on the counter electrode. This isolation allows for the study of a specific reaction with more accuracy. An ideal reference electrode should have little or no current flow through it which does not affect its potential. In this thesis, we used silver/silver chloride (Ag/AgCl) reference electrode for aqueous electrolyte, and silver/silver nitrate (Ag/Ag^{+}) reference electrode for non-aqueous electrolyte. The current is flowing through the working and counter electrodes and is monitored by the potentiostat. The counter electode in three-electrode cell is usually a good conductor which is chemically inerd in the electrolyte. We used a plantium mesh as counter electrodes in all the three-electrode measurements in this thesis.

2.1.2. Cyclic Voltammetry

Cyclic Voltammetry (CV) is a widely used electrochemical measurement technique for evaluating the performance of supercapacitors. In a CV measurement, an applied dc voltage is ramped linearly as function of time across the electrode whose electrochemical properties are being investigated (defined as "working electrode") and the reference electrode.

The current that flow through the electrochemical cell is recorded and plotted as a function of the applied voltage. As an example, **Fig. 2.1.3a** depicts the time dependence of the applied voltage in range of 0-2 V (2-0 V) at a scan rate of 100 mV/s during the charging

(discharging) cycle. A typical cyclic voltammogram of an electric double layer capacitor (EDLC) using two electrode setup with two symmetric activated carbon electrodes is shown in **Fig. 2.1.3b**.

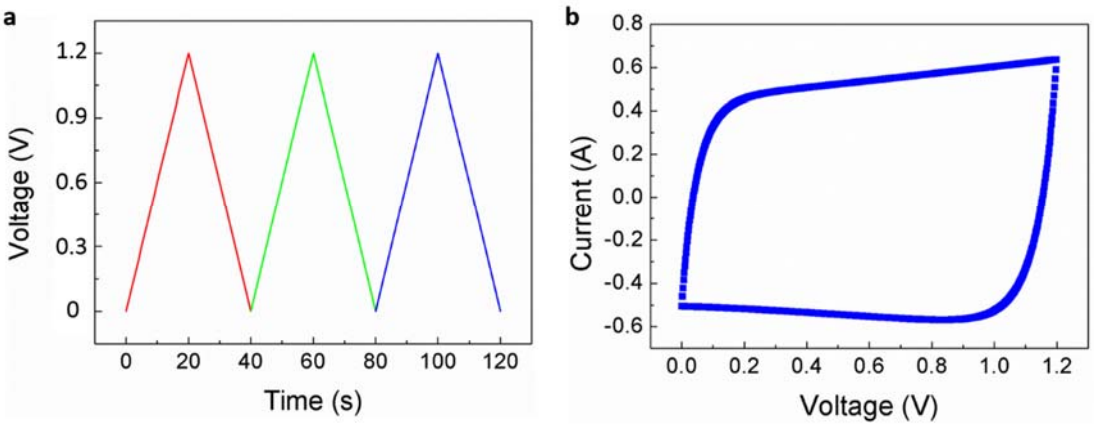

Figure 2.1.3: a) Three cycles of the time dependent applied voltage in a typical cyclic voltammetry study. The voltage is scanned in range of 0 – 1.2 V with a scan rate of 100 mV/s. b) A cyclic voltammogram is the plot of the response current at the working electrode to the applied excitation potential. A cyclic voltammogram over one charge-discharge cycle of a 6 F commercial electric double layer capacitor is shown.

A nearly rectangular shaped voltammogram connotes the absence of red-ox chemical reactions during the CV measurement. The total charge Q that passes through the working electrode in one complete CV scan can be calculated by the following equation:

$$Q = \int Idt = \int_{V1}^{V2} \frac{IdVdt}{dV} = \int_{V1}^{V2} \frac{IdV}{dV/dt} = \int_{V1}^{V2} \frac{IdV}{v}, \qquad (2.1)$$

where I is the current, V is the voltage and v is the set value of the scan rate for the CV measurement. It is clear that $\int_{V1}^{V2} IdV$ is the area enclosed by the voltammogram. Therefore, one can further determine the capacitance of the measured EDLC cell as

$$C = \frac{Q}{\Delta V} = \frac{\frac{Area}{v}}{2(V_2 - V_1)} . \quad (2.2)$$

Here in Eq. 2.2, $(V_2 - V_1)$ is corresponds to the voltage range of CV, and it is multiplied by 2 due to the fact that the voltage is swept back and forth in a complete CV scan.

Besides its utility in gauging performanace of capacitors, CV is in general an important tool for studying electrochemical reactions. Often one finds one or more peaks superimposed on the rectangular shaped EDLC response. **Fig. 2.1.4a** shows a voltammogram of 10mM $K_3Fe(CN)_6$ in aqueous 0.1 M NaCl solution at a Pt working electrode, the cell setup is three electrode with a Pt counter and an Ag/AgCl reference electrode. These peaks are signature of charge transfer reactions between the working electrode and the electrolyte, which occurs at the surface of the electrode.

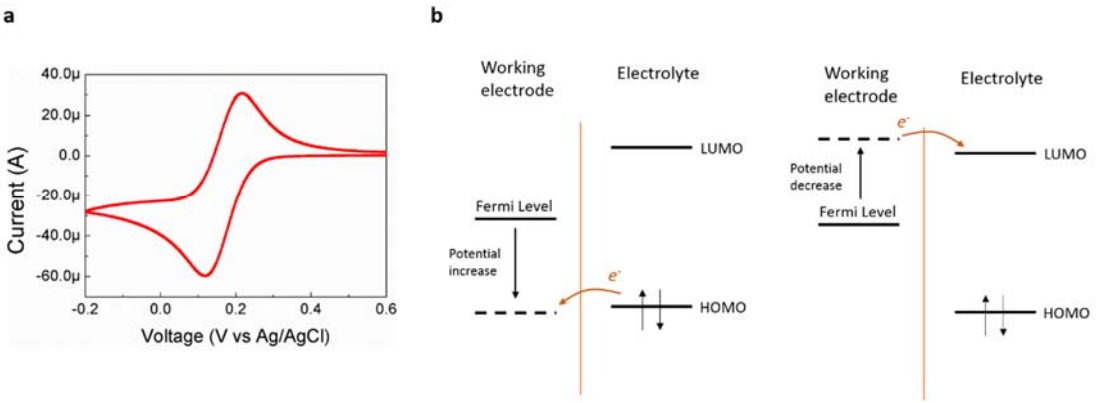

Figure 2.1.4: a) A cyclic voltammogram of 10 mM $K_3Fe(CN)_6$ at a Pt working electrode in aqueous 0.1 M NaCl solution. b) Schematics of the reduction/oxidation process of species from electrolyte during CV. (Figure from Ref. [28])

Since in a three electrode setup, the reference electrode has a constant makeup, its potential is fixed. Therefore, any changes in the cell are ascribed to the working electrode. We say that we observe or control the potential of the working electrode with respect to the reference, and that is equivalent to controlling the energy of the electrons within the working electrode. In **Fig. 2.1.4a**, the potential of the working electrode is first raised from -0.2 to 0.6 V, or the voltage is swept in the positive direction which reduces the energy of the electrons, i.e., the Fermi level of the working electrode is lowered. As shown in **Fig. 2.1.4b**, at a particular potential, the Fermi level of the working electrode reaches the value of the highest occupied molecular orbitals (HOMO) of species A in the electrolyte, and electrons will transfer from A to the electrode, resulting in an oxidation of A to A^+ as well as the appearance of peak in the current signal. Similarly, when the potential is driven

negatively from 0.6 to -0.2 V, the Fermi level of the working electrode increases and matches with the lowest unoccupied molecular orbitals (LUMO). At this potential reduction species A is reduced from A^+ to A and is accompanied by the appearance of a valley in CV. In the example of **Fig. 2.1.4a**, the species A/A^+ refers to $Fe(CN)_6^{4-}/Fe(CN)_6^{3-}$. The peak/valley in CV correspond to one reduction/oxidation reaction, and is defined as a redox couple. A redox couple in CV provides a lot of information for studying electrochemical reactions, such as determining the formal reduction potential and the reversibility of the reaction, calculating the equilibrium ratio, predicting the possible reaction as well as the intermediate reaction states, etc. [29] Therefore, CV has been widely used in the characterization of pseudocapacitors,[30] batteries,[31] biomolecular interactions,[32,33], etc.

2.1.3. Charge-discharge

In a charge-discharge measurement, the electrochemical cell is galvanostatically cycled at a fixed current density between the highest and the lowest voltage limits. It is a method which has been widely used to determine the cycle-life as well as capacitance (or capacity) of EDLCs or batteries.[31] A typical charge-discharge curve of an EDLC device in a two electrode setup with two symmetric carbon electrodes is presented in **Fig. 2.1.5**.

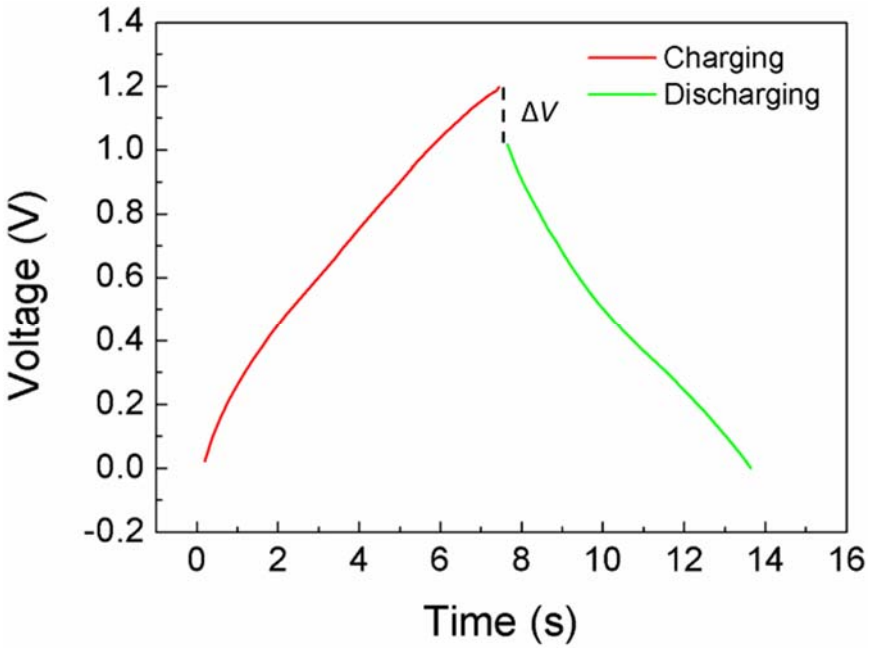

Figure 2.1.5: Charge-discharge curve of an EDLC device with two symmetric electrodes made of multiwall carbon nanotubes in 1 M $HClO_4$ aqueous electrolyte. Current density: 50 A/g.

In a system with no electrochemical reaction, the voltage increases/decreases linearly with time during the charge/discharge process. The specific capacitance of the EDLC device can be calculated from the slope of the discharge curve:

$$C = \frac{I}{\frac{dV}{dt}} = \frac{I}{|Slope|}, \tag{2.3}$$

where I is the discharge current density.

It is noteworthy that a voltage drop ΔV between the end of the charge cycle and the beginning of the discharge cycle may be present. This voltage drop can be used to calculate the equivalent series resistance (ESR) of the cell as

$$ESR = \Delta V / \Delta I \, . \tag{2.4}$$

In the equation $\Delta I = \left|I_{charge}\right| + \left|I_{discharge}\right|$ is the change of current density from charge to discharge.

From Eqs. 2.3 and 2.4, the energy density *E* as well as power density *P* of the EDLC can be estimated from the charge-discharge results as

$$P = \frac{V^2}{ESR} \, , \tag{2.5}$$

$$E = \frac{1}{2} C V^2 \, . \tag{2.6}$$

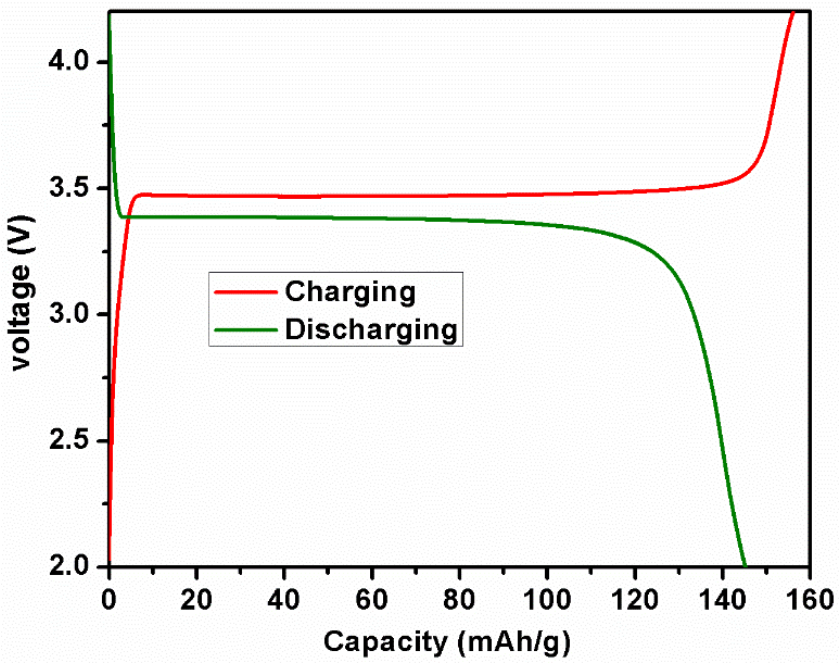

Figure 2.1.6: Charge-discharge curves of a Li-ion coin-cell battery (half cell) with lithium iron phosphate as cathode material and Li metal as the anode. Electrolyte: 1 M $LiPF_6$ in 1:1 Ethylene carbonate and diethyl carbonate organic solvent. Schematic shows the measurement setup for the cell.

Figure 2.1.6 shows a charge-discharge curve of a Li-ion battery with lithium iron phosphate as cathode material and Li metal as the anode. In the schematic shown in **Fig. 2.1.6**, a fixed current density is applied and the voltage is measured as shown. Due to the electrochemical reaction, the voltage of the cell does not change linearly with time. The plateaus on the charge/discharge curves corresponding to the oxidation/reduction of the ions at the cathode. The charging/discharging capacity of the battery is calculated by multiplying the fully charge/discharge time by the applied current density. It is also simple

to calculate the energy density E and power density P from the charge/discharge curves of a battery as

$$E = V \times Q \ , \tag{2.7}$$

$$P = E/t \ . \tag{2.8}$$

In the Eq. 2.8, with a fixed current density, V denotes the nominal voltage which is measured at the midpoint between fully charged and fully discharged states. Q is the capacity which the battery delivers, and t is the time used to fully discharge the battery.

2.1.4. Electrochemical impedance spectroscopy

When a circuit consists of elements which are not purely Ohmic, the current response does not change linearly with applied voltage due to the phase shift, and hence the system is non-linear (**Fig. 2.1.7a**). The impedance of the non-linear system is in a complex form, and frquency dependent. Electrochemical impedance spectroscopy (EIS) is a powerful tool to accurately unravel the non-linear processes and to study the dynamics of the electrochemical cells.

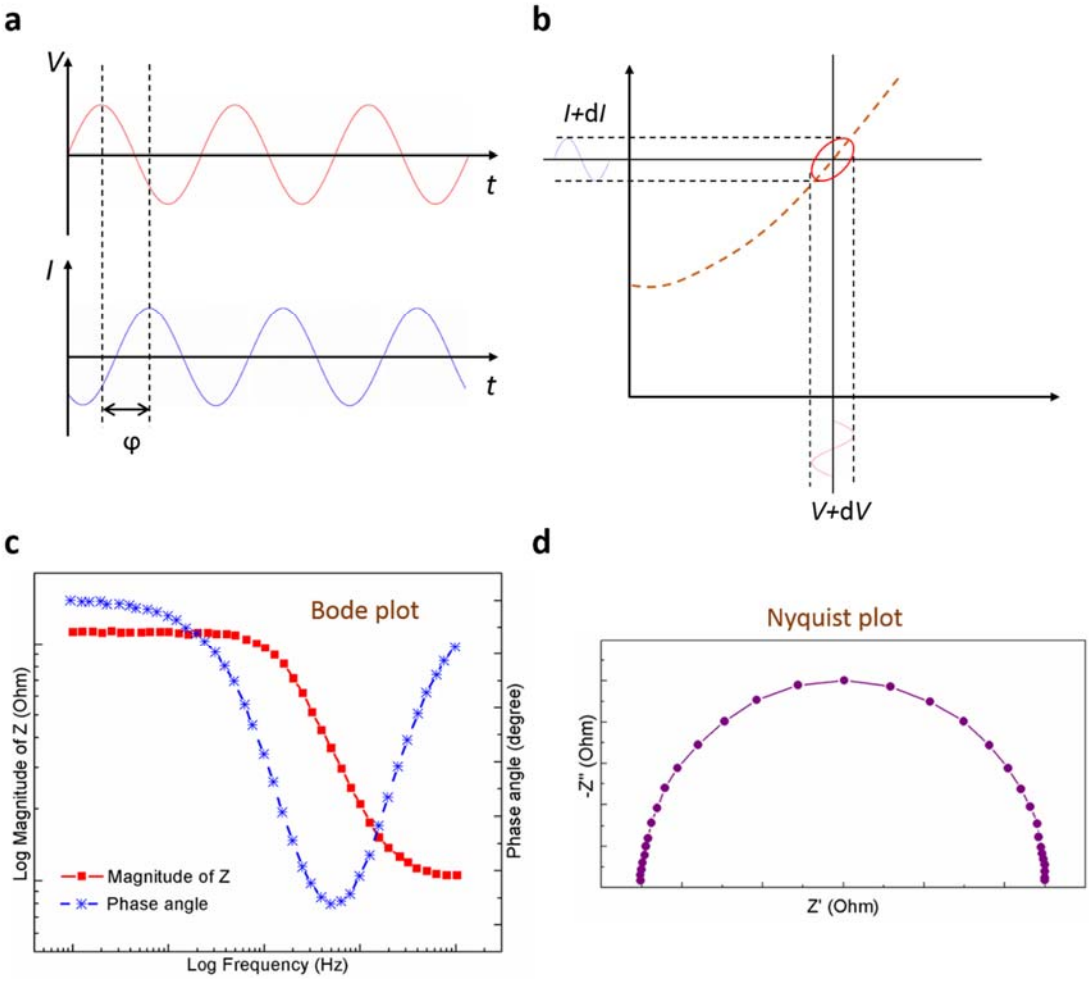

Figure 2.1.7: a) Phase shift between current and applied AC voltage in a non-linear system. b) In an EIS measurement, a small AC perturbation dV is applied. The AC current response of the circuit is phase shifted relative to that of dV, which results in the ellipitical shape shown in the panel b. The brown dash line clearly shows the non-linear current dependence to the DC voltage. However, when the investigated voltage range V is small enough (in range of dV), the DC current vs voltage curve can be considered as pseudo-linear. c, d) EIS may be present in two forms: c) Bode plot and d) Nyquist plot.

EIS measurements are usually carried out by applying a small AC perturbation signal with a fixed applied DC voltage to an electrochemical cell. The frequency of the perturbation signal is changed and the current through the cell is recorded. The amplitude of the AC signal is small enough so that the response of the cell can be considered as pseudo-linear (see **Fig. 2.1.7b**). As shown in **Fig. 2.1.7a**, for an electric circuit with complex form of impedance $Z = Z' + jZ"$, the response of its current, $I = I_0\sin(\omega t + \varphi)$, exhibits a phase-shift φ relative to the applied voltage signal $V = V_0\sin(\omega t)$. It can be seen from Eq. 2.9 that both the real and the imaginary parts of the impedance are frequency dependent and can be written in the form of Eq. 2.10 as

$$Z = \frac{V_0\sin(\omega t)}{I_0\sin(\omega t+\varphi)} = Z_0\frac{\sin(\omega t)}{\sin(\omega t+\varphi)}, \tag{2.9}$$

$$Z(\omega) = Z'(\omega) + Z"(\omega) = Z_0(\cos\varphi + j\sin\varphi) . \tag{2.10}$$

EIS typically has two output formats, while the Bode plots consist of two plots of the magnitude of impedance versus frequency as well as the phase angle φ versus frequency, the Nyquist plot is a plot of $Z"$ versus Z' (see **Figs. 2.1.7c and d**). An EDLC cell can be simply modeled by the Randles cell circuit (schematic in **Fig. 2.1.8a**).

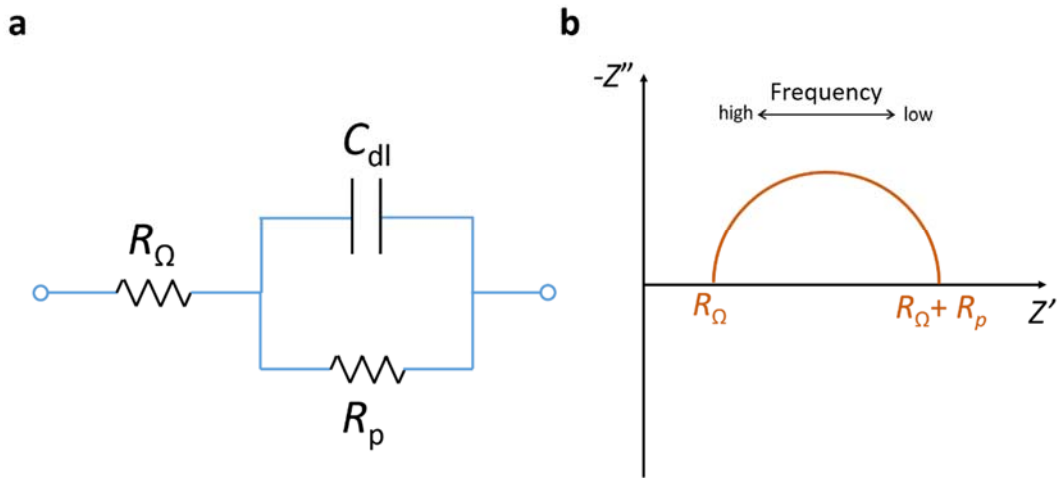

Figure 2.1.8: a) Schematic of Randles cell circuit. b) Theoretical Nyquist plot for Randels cell.

In **Fig. 2.1.8a**, the element R_Ω refers for the uncompensated resistance contributed by the wires, connections, resistance from the electrode materials as well as the solution. C_{dl} is the double layer capacitance and R_p is the polarization resistance attributed by the transition resistance between the electrode and the electrolyte. The impedance of the Randles cell is expressed as

$$Z = R_\Omega + \frac{1}{\frac{1}{R_p} + j\omega C_{dl}}, \tag{2.11}$$

from which it follows that

$$Z' = R_\Omega + \frac{R_p}{1 + (j\omega R_p C_{dl})^2}, \tag{2.12}$$

$$Z'' = -\frac{\omega R_p^2 C_{dl}}{1+(j\omega R_p C_{dl})^2}. \quad (2.13)$$

Clearly from Eqs. 2.12 and 2.13, the Nyquist plot of the Randles cell is a semicircle as shown in **Fig. 2.1.8b**. In the Randles cell circuit, the impedance from the element C_{dl} is frequency dependent which varies as $\sim\frac{1}{j\omega C_{dl}}$. At high frequency the impedance of C_{dl} is close to zero and it acts as a short, which and leaves only RΩ contribution to the total impedance. Also, the impedance of C_{dl} approaches infinity with frequency decreases and acts as an open circuit at low frequency. Therefore, the total impedance is equal to the value of R_Ω + R_p at the low frequency end, and the imaginary part of Z is zero at both high frequency and low frequencies.

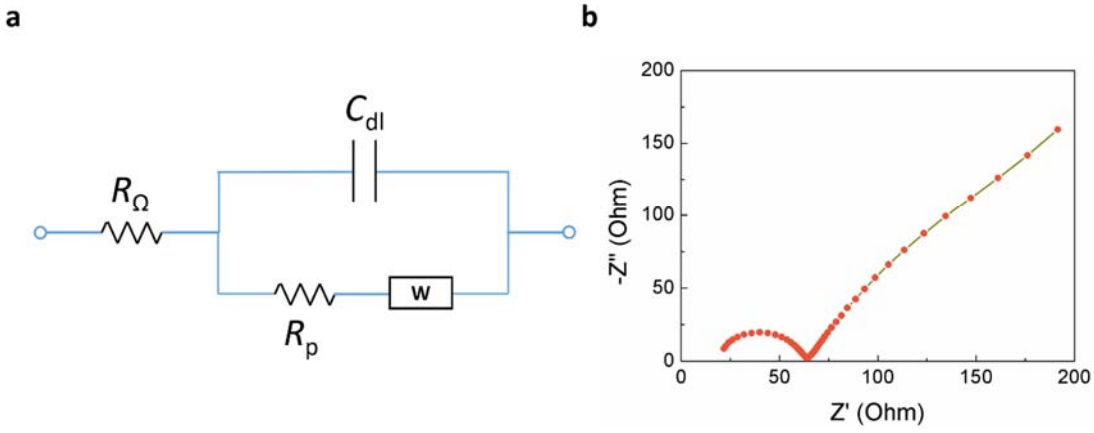

Figure 2.1.9: a) Schematic of Randles cell circuit including Warburg impedance. b) A Nyquist plot of a multiwall carbon nanotube electrode. The diagonal response whcih appears at the low frequency end of the semicircle is due to ion diffusion. Electrolyte: 1 M $TEABF_4$ in acetonitrile.

A more precise equivalent circuit can be used for modeling the EDLC cell by adding a Warburg diffusion element to the Randles cell in series of R_p (See **Fig. 2.1.9a**). The Warburg impedance is due to the diffusion of ions and is also frequency dependent (see Eq. 2.14).

$$Z_W = \sigma(\omega)^{-1/2}(1 - j) \; . \tag{2.14}$$

The Warburg impedance is small at high frequency since the diffusion path of ions are short. However, it increases at low frequency because the ions have to move further, which results in the appearance of diagonal response at the low frequency end of the semicircle (see **Fig. 2.1.9b**).

EIS has been frequently used for analyzing the resistance and diffusion information in capacitors and batteries.[34–37] Moreover, as it has variety of output formats and is applicable to many forms of electric circuit models, it is also considered as the most powerful and accurate method which has been applied in multiple areas such as diagnosing equivalent circuit,[38] investigating corrosion rate,[39,40] characterizing deposition mechanism,[41] studying the chemical reaction mechanism,[42] chemical synthesis,[42] semiconductors,[38,43], etc.

2.2. Raman Spectroscopy

2.2.1. Introduction of Raman

When a monochromatic light is shone on a medium (which could be in the form of a liquid, solid or gas), the scattered light is found to be shifted in energy when compared to the incident light energy. This phenomenon, which has been called the Raman effect, is attributed to the inelastic scattering of light from the medium. The inelastic scattering results from the interaction between the incident photons and the vibration of the molecules in the media, as shown schematically in **Fig. 2.2.1a**. The Raman effect was theoretically predicted by Adolf Smekal[44] and experimentally observed by Sir C. V. Raman[45].

In a Raman scattering experiment, the incident light (typically a monochromatic laser beam) is incident on the sample. Viewed in terms of energy levels, the electrons reside in the ground vibrational and electronic states before excitation. The monochromatic laser source excites the electrons to a virtual state, equal to the energy of the laser. When the electrons relax back to the ground electronic state, most go back to the ground vibrational state, giving back the same energy. This is Rayleigh (elastic) scattering. The other small portion that relaxes back to an upper or lower vibrational state is the Raman scattered light. The Raman scattered light that is adjusted up in wavelength is called the Stokes Raman scattering and that light which is adjusted down in wavelength is called the anti-Stokes Raman scattering (**Fig. 2.2.1b**). Stokes Raman scattering occurs when some energy is absorbed from the photon of the incident light into the molecule's rotational and vibrational energy and consequently a new photon of light with less energy is released. Anti-Stokes

scattering occurs when the new photon formed gains energy compared to the incident photon via the absorption of energy from a previously excited molecule. [46]

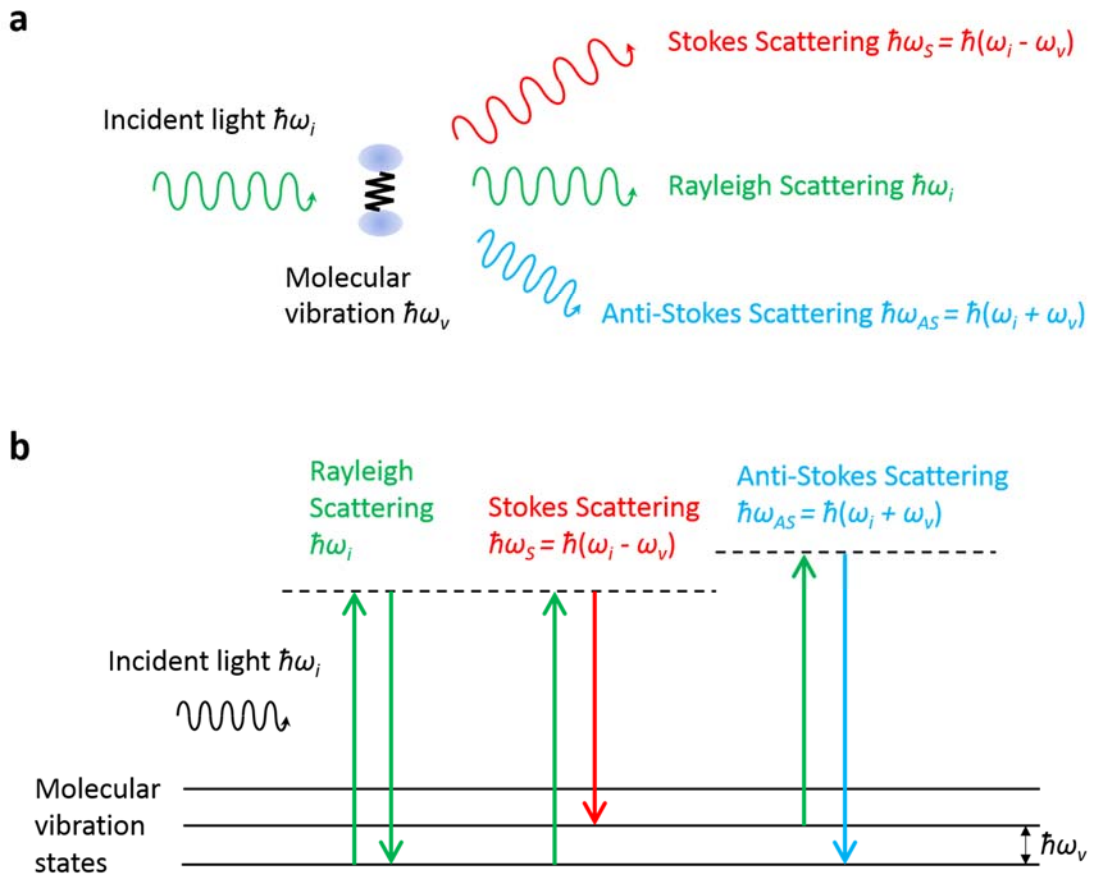

Figure 2.2.1: a) A schematic of incident light interacting with molecules, which results in elastic and inelastic scattering. b) Processes of Stokes and anti-Stokes scattering.

Fig. 2.2.1b demonstrates the Stokes and anti-Stokes processes, which are shifted in frequency relative to the incident laser energy. On the other hand, the Rayleigh scattered

light has same frequency as that of the incident laser and can be filtered out using a notch filter. **Fig. 2.2.2** shows Raman spectrum of sulfur with exciting laser wavelength 1064 nm. The anti-Stokes scattering has much less cross-section than that of the Stokes scattering, owing to the fewer probabilities of the existence of the excited molecules.

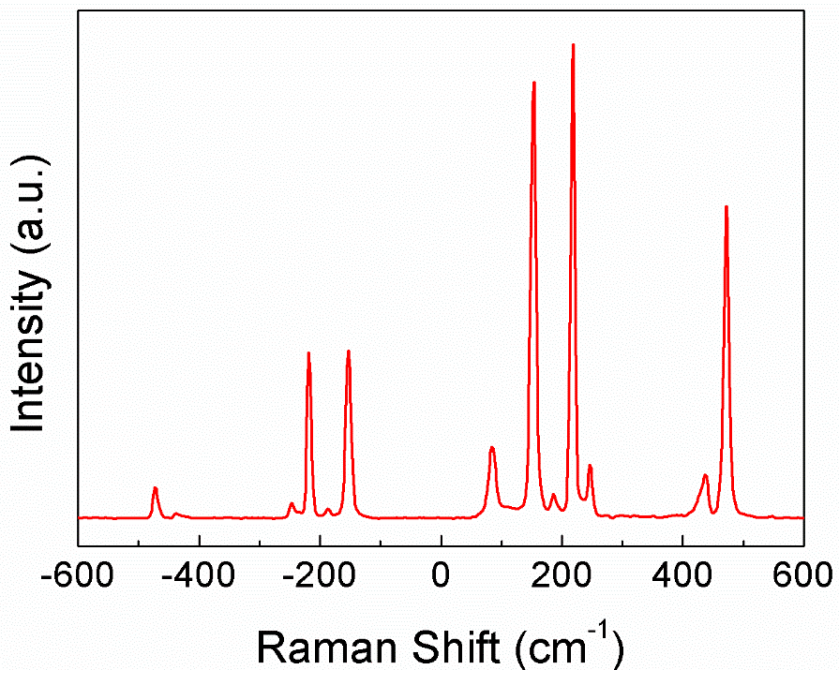

Figure 2.2.2: Raman spectrum of sulfur with exciting laser wavelength 1064 nm. The peaks with positive/negative Raman shift are from Stokes/anti-Stokes scattering. It can be seen that the (*i*) frequency positions of the anti-Stokes peaks are symmetric to those of the Stokes peaks, and (*ii*) intensity of anti-Stokes peaks are much weaker compared to the Stokes peaks.

Clearly, Raman spectroscopy provides information of molecular vibration, which can be used as a "fingerprint" to identify materials and to analyze the molecule structure, symmetry, or chemical bonds. In addition, Raman spectroscopy is not moisture sensitive and can be performed easily under ambient conditions. Raman spectroscopy has evolved into an indispensable characterization tool for graphene, which will be introduced in next section.

2.2.2. Phonon dispersion in graphene

The phonon dispersion relation provides a full picture of the molecular vibration of graphene, as shown in **Fig. 2.2.3**. As introduced in Chapter 1, graphene has two atoms in each of its unit cell. Each atom contributes 3 phonon branches. Therefore, there are totally 6 phonon branches of graphene. Three of the phonon branches are acoustic, which are denoted as: longitudinal acoustic (*LA*), in-plane transverse acoustic (*iTA*) and out-of-plane transverse acoustic (*oTA*). Similarly, the other 3 phonon branches are optic and they are denoted as longitudinal optic (*LO*), in-plane transverse optic (*iTO*) and out-of-plane transverse optic (*oTO*).[47] Starting from the center of the Brillouin Zone (BZ) (i.e., the Γ point), the momentum of the phonon vary from 0 to $\frac{4\pi}{3a_0}$, here a_0 refers to the length of the unit vector in the graphene lattice, and equals to $\sqrt{3}a \sim 0.26$ nm.

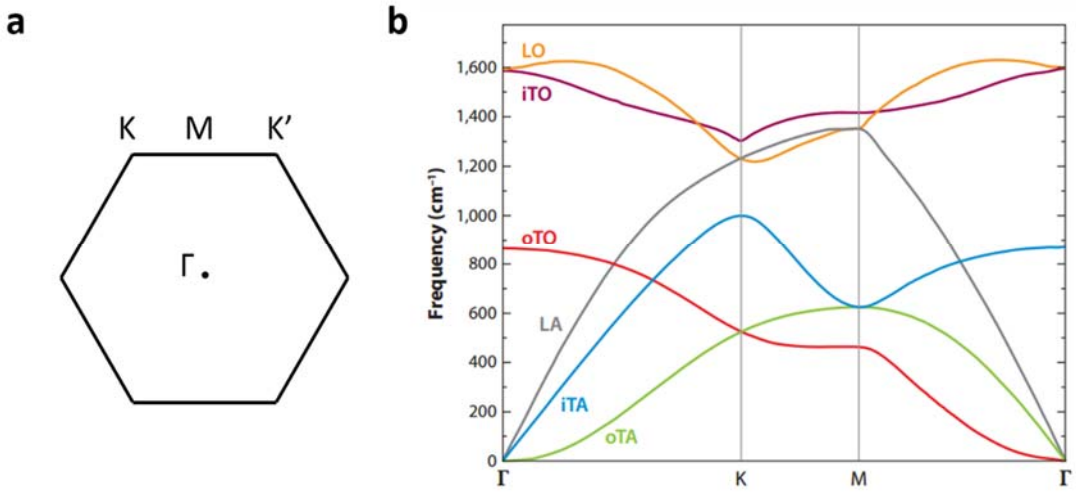

Figure 2.2.3: a) Brillouin zone of graphene in which the center point Γ is the point where momentum is zero. b) The phonon dispersion relation of graphene. [48]

The momentum of a photon is equal to $\frac{2\pi}{\lambda}$, where λ is the wavelength of the light. The laser light that is used in a typical Raman experiment is usually in range of visible or IR light with wavelength ranging from ~ 200 to 1100 nm. Therefore, the momentum of the photons are much smaller than that of the maximum dimension of graphene's BZ. Considering the momentum conservation law, the only allowed modes that could be detected by Raman spectroscopy are phonons with momenta close to the Γ point, or zone-center phonons. Since acoustic phonons have nearly zero energy at the Γ point, and the *oTO* phonon mode is not Raman active, according to the phonon dispersion relation in **Fig. 2.2.3b**, only one peak is expected in graphene's Raman spectrum ~ 1600 cm^{-1}, which corresponds to the doubly degenerate *LO* and *iTO* phonon modes at the Γ point.

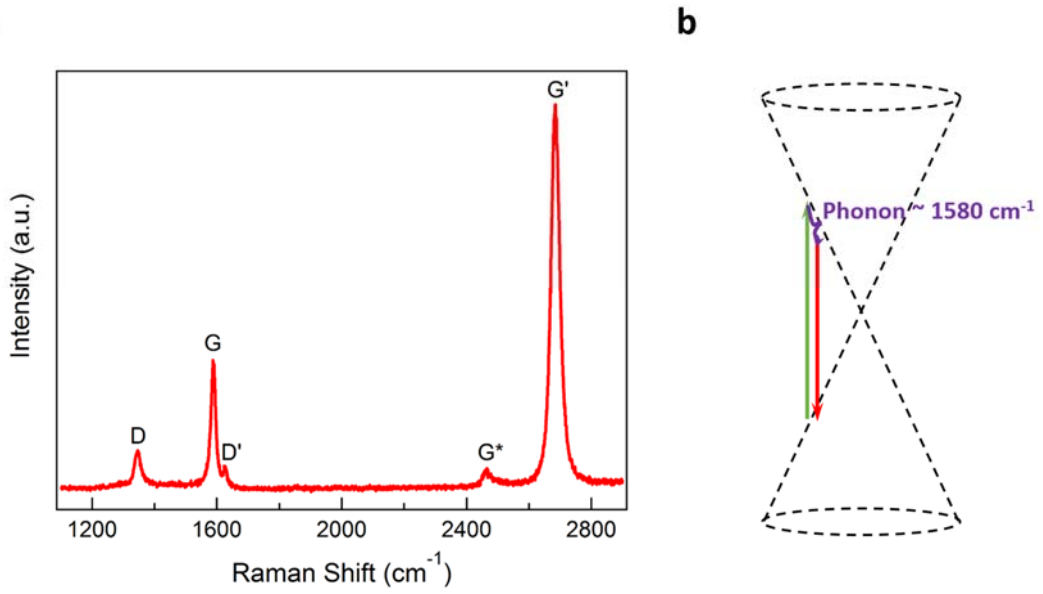

Figure 2.2.4: a) Raman spectrum of a CVD grown single layer graphene at room temperature, the laser wavelength is 532 nm. b) Schematic of the Raman process for the *G*-band in graphene.

From the Raman spectrum of the single layer graphene (**Fig 2.2.4a**), clearly a dominant peak ~ 1580 cm^{-1} is present, which matches with our prediction. This band is denoted at graphitic band, or *G*-band. **Fig. 2.2.4b** presented the schematic of the *G*-band Raman process. The electrons from ground state were first excited by the incident photon to an excited state (represented by the green arrow). The excited electrons are then scattered by a phonon (with zero momentum) which carry away a portion of the energy to the electrons. Consequently, the electrons relax to their original state and emit a photon

with less energy (Stokes scattering). Nevertheless, in addition to the *G*-band, additional peaks are also present in **Fig. 2.2.4.** These peaks are the so-called *D*-band ~ 1350 cm^{-1}, *G*'-band ~ 2700 cm^{-1}, *D*'-band ~ 1610 cm^{-1}, *G**-band ~ 2450 cm^{-1}, and so on [47]. These peaks do not match with any phonon branch at the Γ point and seem to violate the law of momentum conservation. As explained in next section the origin of these additional peaks can be understood within the framework of the double-resonance (DR) Raman process.

2.2.3. Double-resonance process in graphene

In a typical Raman scattering process, there are normally three steps: *i*) the incident light excites electrons from the valence band of the medium to a state with higher energy (the state could be either a real or a virtual state). *ii*) the excited electrons interact with phonons in the medium and emit or absorb phonons, and *iii*) the electrons relax back to the valence band by emitting a photon. In the above process *ii*), if the excited electron happens to be in a real energy state before or after its interaction with the phonons, a resonant Raman scattering occurs, and the scattering cross-section can be $>10^3$ times larger than that of the non-resonance Raman scattering.[49] Thus, resonant Raman spectroscopy is well suited for characterizing samples which are available in limited quantity.[50] However, typically limited laser excitation energies as available, which prevents the possibility of characterizing all materials through resonance Raman scattering.

As discussed in Chapter 1, graphene has non-zero band gap at the *K* and *K*' points in its electronic band structure, and exhibits a linear dispersion above and below its Fermi

level. This unique electronic band structure allows the possibility of probing graphene through resonant Raman scattering with any incident excitation. In graphene, the *G*-band originates from a first-order process, as previous explained in **Fig. 2.2.4b**. There could also be higher-ordered Raman processes, which allows the excited electrons to interact with phonons with momentum $q \neq 0$ without violating the momentum conservation law. For instance, in a second-order process, an excited electron could at first interact with a phonon with momentum q, following by another interaction with a phonon with momentum of $-q$. The chance of higher-order Raman processes are very limited unless they match the resonance conditions. Hence, in graphene, a material with electronic band structure that is conducive for resonant Raman process, we can expect to see higher-order Raman bands. In **Figure 2.2.3**, peaks *D*, *D*' and *G*' are known to come from second-order resonance Raman processess, which is also called DR Raman process.

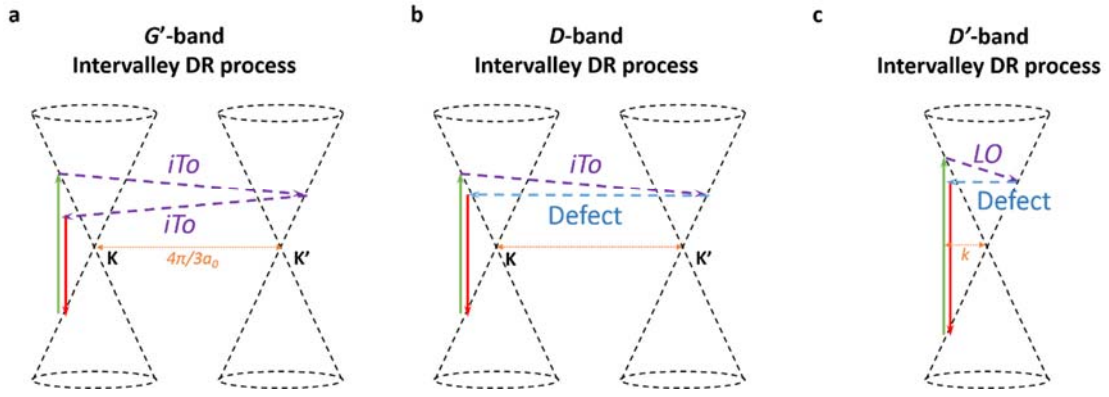

Figure 2.2.5: a, b) The intervalley double-resonance picture of a) *G*'-band, b) *D*-band. c) The intravalley double-resonance picture of the *D*'-band.

The *G*' band has the highest intensity and originates from a two-phonon double resonance process. From **Fig. 2.2.3b**, one can notice that the peak position of *G*'-band ~ 2700 cm^{-1} , which is twice the frequency of the *iTO* phonon near *K* point (i.e. phonon momentum $q \sim \frac{4\pi}{3a_0}$). Indeed, *G*' is an overtone of two *iTO* phonons with $q \sim \frac{4\pi}{3a_0}$ due to an intervalley DR process (see **Fig. 2.2.5a**).

The *D*-band, which has frequency equal to one *iTO* phonon near the *K* point also originates from the intervalley DR resonance (**Fig. 2.2.5b**) in which the excited electron experiences one inelastic scattering by the *iTO* phonon with moment $q \sim \frac{4\pi}{3a_0}$ followed by another elastic scattering by a defect, with momentum -*q*. It is important to note that the *D*-band manifests in the Raman spectrum only when defects (missing carbon atoms, dopants, etc.) or edges (zig-zag edges) are present in graphene. The intensity ratio of *D*-band to *G*-band is inversely proportional to the average in-plane crystal size of graphene [51] and can be expressed as

$$L_a \text{ (nm)} = (2.4 \times 10^{-10} \text{ nm}^{-3})\, \lambda^4_{laser}\ (nm^4)\ (I_D/I_G)^{-1} . \qquad (2.15)$$

Therefore, I_D/I_G had been widely used for identifying the defect concentration and the quality of graphene.

Another defect dependent peak in the Raman spectrum of graphene is the *D*'-band which is found next to the *G*-band. As shown in **Fig. 2.2.5c**, the *D*'-band comes from an

intravalley DR process, involves two scattering events: by an *LO* phonon with $q = 2k$ and a defect, respectively.

Beside the above discussesion of zone-centered and off-zone-centered Raman bands, other weaker Raman peaks with that arise from higher-order processes (combination or overtone of two or more phonons) have also been reported in graphene [47,52–54]. One of them is the *G**-band ~ 2450 cm^{-1} whose origin remains unclear, and whose asymmetric lineshape continues to intrigue carbon researchers. In Chapter 5, we will elucidate the origin of *G**-band, and discuss in detail the role of defects on the *G**-band.

CHAPTER 3

ROLE OF DEFECTS AND DOPANTS ON THE ELECTROCHEMICAL PROPERTIES OF GRAPHENE

3.1. Introduction

Supercapacitors (SCs) are novel electrochemical devices that store energy through reversible adsorption of ionic species from an electrolyte on highly porous electrode surfaces. SCs are highly durable (lifetime >10,000 cycles) with power densities (10 kW/kg), that are an order of magnitude larger than achievable power density in batteries. But the low energy density (10 Wh/kg) of SCs[55] relative to batteries limits their use in practical applications despite their ability to withstand >10,000 cycles. Graphene-based nanocarbons are ideal electrode materials for SCs due to their low cost, high stability, and high specific surface area. Indeed, an outstanding characteristic of single-layer graphene is its high specific surface area of ~2675 m^2/g, which sets an upper limit for electrical double layer capacitance (C_{dl}) ~21 $\mu F/cm^2$ (~550 F/g).[55–58] Notwithstanding this desirable attribute, there are two intrinsic bottlenecks that impede the emergence of high energy density SC devices: i) typically only 50-70% of the theoretical surface area is accessible to ionic species present in the electrolyte,[55,56] which limits the overall capacitance (10-15 $\mu F/cm^2$) and leads to a low energy density, and ii) although the total energy that can be harnessed from a SC device depends predominantly on ion-accessible surface area, it is not

the only factor. The presence of a so-called quantum capacitance (C_Q), which is (i) small and in series with C_{dl}, and (ii) arises from the low electronic density of states at the Fermi level (DOS(E_F)) for nanocarbon electrodes, overwhelms the high C_{dl} further reducing the already limited capacitance and low energy density.[59–61]

While efforts to increase the energy density have been focused either on increasing the active surface area or the pseudo-capacitance through the inclusion of redox active materials, pragmatic methodologies to resolve the inherent bottlenecks described above are still lacking. In this chapter, I experimentally show that engineered defects in graphene can alleviate these bottlenecks resulting in a new paradigm for energy storage beyond the predicted theoretical limits.

Defects are often perceived as performance limiters in bulk materials, and this perception is all the more exacerbated in 2D materials such as graphene. Yet, my experimental findings conclusively demonstrate that controllably induced defects in specific configurations can achieve 150% enhancement (~50 μF/cm^2) in measurable capacitance of few-layer graphene (FLG). A detailed density function theory (DFT) calculations performed by my collaborators show that the nitrogen dopants in the pyrrolic configuration result in a high DOS(E_F) and thereby mitigate the influence of C_Q. Furthermore, access by the electrolyte ions (e.g., tetraethylammonium (TEA^+) ions) to the inter-layer gallery space in FLG can be effectively enhanced through defect-induced pores in graphene, leading to an increased charge storage capacity. More importantly, I show that these high-capacitances can be extended to coin-cell devices based on FLG foams that

result in energy densities that are at least five times higher than the conventional activated carbon-based SCs.

3.2. Experiment and Calculation Methods

3.2.1. Calculation methods

The geometry optimization of bilayer graphene with electrolyte molecule and the three types of dopant configurations along with their electron density profiles were performed using a DFT based atomistic tool kit virtual nano lab.[62] The optimization was performed at mesh cut off 150 Rydberg. Local Density Approximation (LDA with Perdew-Zunger) has been used as exchange correlation functional with Double Zeta Polarized basis set. The structure was optimized until the net force on every atom became less than 0.01 eV/ Å. Sampling of the Brillion zone for structure relaxation was taken as 1x3x3 using Monkhorst-Pack Scheme.

3.2.2. Synthesis of N-doped few-layer graphene and graphene foam

FLG and graphene foams on Ni substrates were synthesized through a chemical vapor deposition (CVD) method.[63] Doping of nitrogen atoms in FLG and graphene foams was achieved during the CVD synthesis by the introduction of benzylamine and acetonitrile in varying proportions to yield the pyridinic, pyrrolic, and graphitic configurations in FLG (see schematic in **Figure 3.2.1)**. Ni foils with thickness of 25 μm

were placed away from the center of a 24 mm diameter tube furnace. The furnace was maintained at 900 °C under a flow of 200 sccm Ar and 120 sccm H_2. Ni foils were moved to center of the furnace after 90 minutes, and the furnace was reset to 850 °C. Under these CVD conditions, decomposing ~10 sccm of methane for 10 min yielded the FLG on the Ni foils. To dope FLG with nitrogen, additional Ar (~50 sccm) was bubbled through a mixture of benzylamine and acetonitrile (3:1, 1:1, and 0:1 for samples N1, N2, and N3, respectively), as shown in **Fig. 3.2.1**. After 10 mins, the methane flow was switched off and the samples were moved away from the center of the furnace, and the furnace temperature was ramped down to 400 °C at a rate of 5 °C/min. Next, the H_2 flow was shut off and the furnace was maintained at 400 °C for an additional 90 min. Finally, the samples were cooled to room temperature under Ar flow. For each N-dopant configuration, at least three sister samples were used in our spectroscopic studies. FLG samples were also Ar^+ plasma etched using a reactive ion etching unit (Hummer 6.2) at multiple powers from 10-120 W for 2 min to induce defects. Dopant and defect concentration were quantified using Raman spectroscopy and X-ray photoelectron spectroscopy.

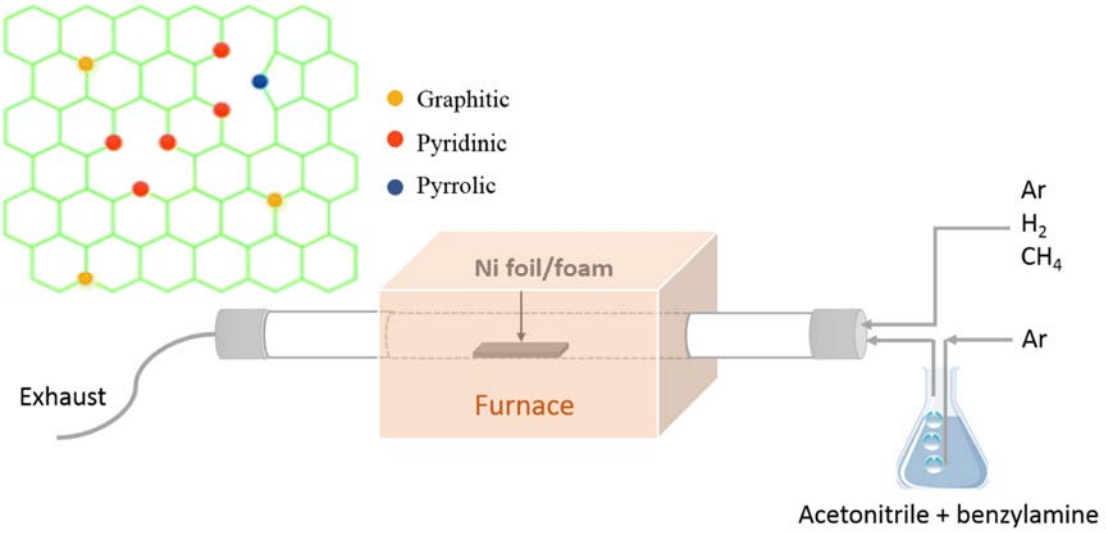

Figure 3.2.1: Schematic of the CVD setup for the growth of pristine and N-doped graphene. The inset figure shows the pyridinic, pyrrolic, and graphitic configurations in which nitrogen atoms are incorporated into the graphene lattice. [64]

The pristine graphene foams (GFs) used in this study were grown on Ni foams using the thermal CVD method, similar to the FLG. After the growth of GFs on Ni foams, the latter were etched away by submersing the GF/nickel foam in a 1:4 (by volume) 12 M hydrochloric acid: 15.8 M nitric acid solution. The free-standing GF was then rinsed with DI water and allowed to dry. Some of these GFs were also subjected to a 120 W Ar^+ plasma for 2 minutes at 120 mtorr. Post nitrogen doping of free-standing GFs was accomplished by annealing them in a tube furnace at 600°C for 1 hr under a 500 sccm flow of argon which was bubbled through acetonitrile.

3.2.3. Structural and electrochemical characterizations

A Dilor XY triple grating monochromator was used for collecting the micro-Raman spectra of all samples with the 532 and 633 nm excitation. X-ray photoelectron spectroscopy (XPS) studies were performed using a Kratos Axis Ultra DLD instrument and spectra were calibrated by the C 1s line at 284.6 eV. The morphology of the samples was observed using scanning electron microscopy (SEM, Hitachi S4800) with an accelerating voltage of 20 kV and tunneling electron microscopy (TEM, Hitachi H9500).

The electrochemical properties of samples were characterized in a Gamry reference 3000 electrochemical potentiostat. The electrolytes were 0.25 M tetraethylammonium tetrafluoroborate ($TEABF_4$, >99%) or tetrabutylammonium hexafluorophosphate ($TBAPF_6$, >99%) in acetonitrile (ACN). Two systems were used for electrochemical characterization: a 3-electrode setup for single electrode characterization, and a 2-electrode cell (coin cell apparatus, MTI Corp) for symmetric supercapacitor measurements. In the 3-electrode cell, the FLG on Ni foils were used as working electrodes, a Pt mesh was used as the counter electrode and a silver/silver ion electrode (Ag/Ag^+) was used as the reference electrode. In the 2-electrode cell, EDLC devices were tested using symmetric GFs as the electrodes with a Celgard (2325) trilayer separator. The electrodes and separator were soaked overnight (~20 hours) in 0.25 M $TEABF_4$-ACN electrolyte prior to the cell assembly. Cyclic voltammetry (CV) was measured from -0.4 to 0 V (0 – 2.5 V) for FLG (GF) samples with scan rate of 1000 mV/s. The electrochemical impedance spectroscopy

(EIS) measurements were carried out with a perturbation signal of 10 mV in the frequency range of 100 kHz to 0.1 Hz.

3.3. Effects of ion etching induced defects and type of electrolytes on electrochemical properties of graphene

3.3.1. Identification of best-suited electrolyte

It has been observed that the best performance of SCs can be realized when the average micropore size in nanostructured bulk electrodes (e.g., carbide-derived carbon) matches the size of the ions in the electrolyte[65–73]. It is expected that such a resonant effect is true even for defect-induced pores in quasi-two dimensional FLG (**Fig. 3.3.1a**). Accordingly, in order to identify the best-suited electrolyte, we theoretically studied the interactions of two different ions – tetraethylammonium (TEA^+) and tetrabutylammonium (TBA^+) with defect-induced pores in FLG. The rationale in choosing these ions lies in the fact that organic electrolytes such as tetraethylammonium tetrafluoroborate ($TEABF_4$) and tetrabutylammonium hexafluorophosphate ($TBAPF_6$) exhibit a wider voltage range, yet are not highly expensive unlike the ionic liquids. In our density functional theory (DFT) calculations, we started with an initial pre-optimized configuration of bilayer graphene with a 1 nm pore (See **Fig. 3.3.2**). Upon the introduction of TEA^+ ion into the interlayer spacing through the 1 nm pore, no significant changes were observed in the optimized bilayer geometry (**Fig. 3.3.1b**) and the edge carbons did not show any chemical

bonding/interactions with the TEA^+ ion. However, a large deformation in the structure of graphene sheets and an increase in the inter-layer spacing was observed in the presence of TBA^+ ion. In particular, we observed that the edge-carbons in the nanopore strongly interact with TBA^+ ion through chemical bonding preventing it from diffusing through the nanopore (**Fig. 3.3.1c**). By analyzing the charge density plots, we found that the TBA^+ ion in our simulations loses two H atoms from its methyl group and subsequently attaches to dangling edge C atoms in the pore through electron sharing C-C bonds. Such an observation may be rationalized in terms of the relatively larger size of TBA^+ (~0.8 nm) compared to TEA^+ ion (~0.45 nm).[35]

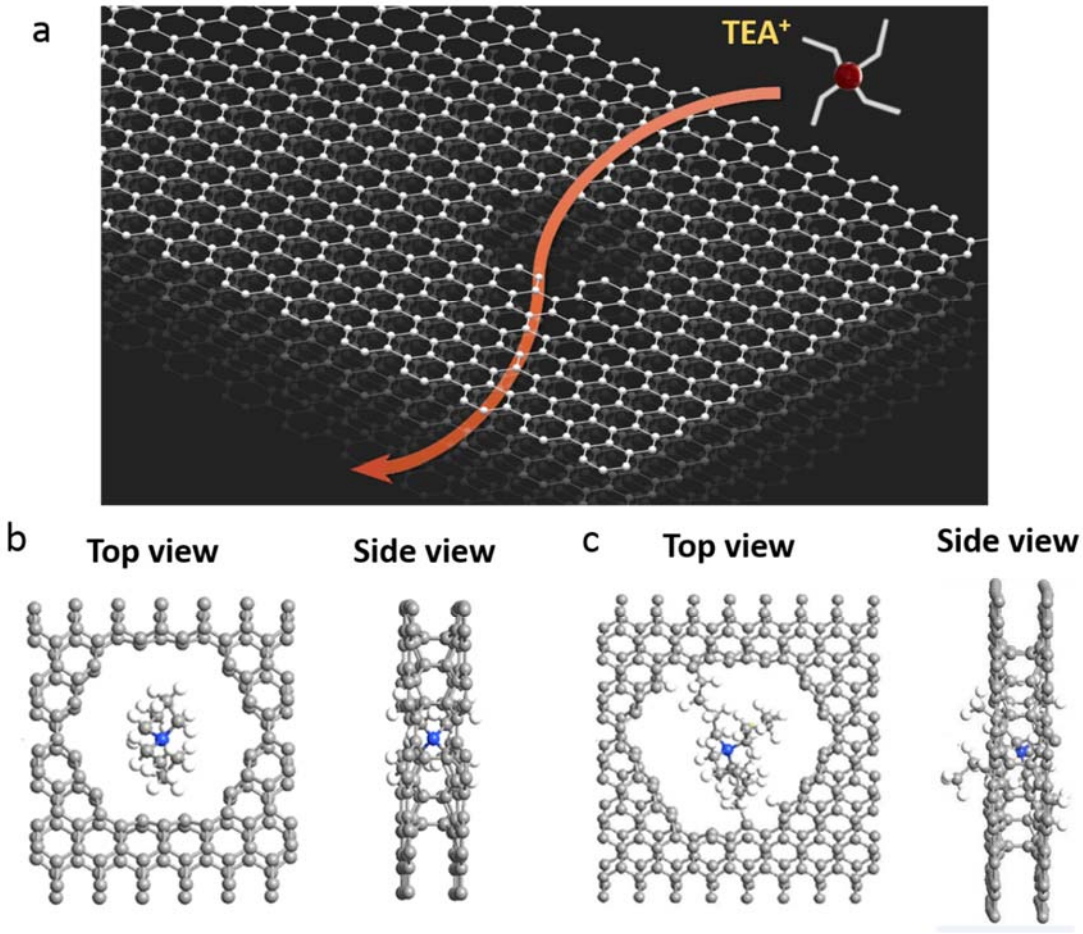

Figure 3.3.1: The interaction of electrolyte ions with defect-induced pores. (a) Defect-induced pores in FLG open otherwise inaccessible surface area by transporting electrolyte ions (e.g., tetraethylammonium (TEA^+)) to inter-layer gallery space. Density functional theory calculations showed that the intercalation of TEA^+ is more favorable (b) compared to tetra-n-butylammonium (TBA^+) (c). In (b) and (c) gray, blue, and white spheres represent carbon, nitrogen, and hydrogen atoms, respectively.

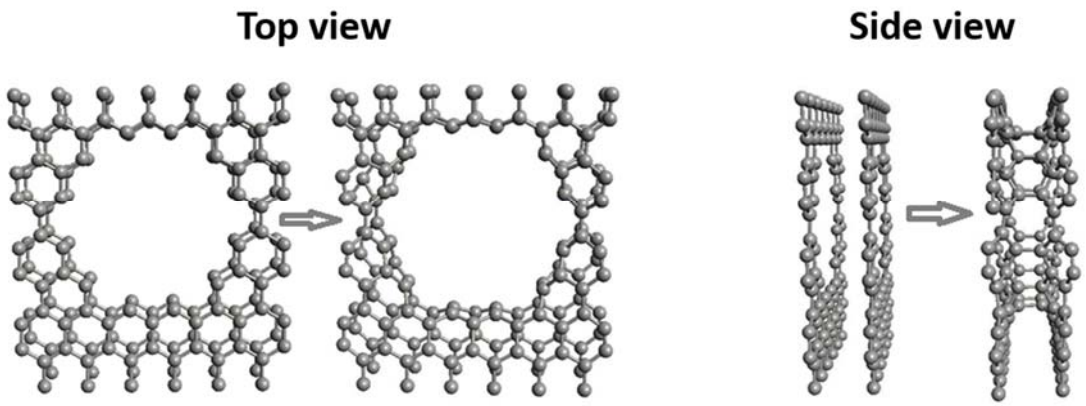

Figure 3.3.2: Structure of bilayer graphene before and after optimization.

3.3.2. Experimental validation of ion-pore size resonance effects

We synthesized FLG and graphene foams on Ni foils through chemical vapor deposition (CVD) using as described above. We used Ar^+ plasma etching and N-doping to induce defects in the FLG.[59] The defect-formation energy for extended defects is much lower compared to single- and di-vacancies, and thus we observed the formation of nanosized pores in FLG upon Ar^+ exposure (**Fig. 3.3.3a**). In the Raman spectrum of graphene, the peak present at ~1350 cm^{-1} (or the so-called *D*-band) arises from the presence of defects such as nanopores, and its normalized intensity has been widely used to quantify defect density.[59,74] Accordingly, the defects in our FLG were quantified using the normalized Raman intensity ratio (I_D/I_G) of the *D*-band to the graphitic or *G*-band present at ~1580 cm^{-1}.[75] We varied the Ar^+ plasma power to produce FLG with different defect densities or I_D/I_G, and as expected, I_D/I_G was found to increase linearly with the Ar^+ plasma

power (see inset of **Fig. 3.3.3b**). We performed cyclic voltammetry (CV) using a three-electrode electrochemical cell to study the electrochemical response of different electrolytes, viz., 0.25 M $TEABF_4$ or $TBAPF_6$ dissolved in acetonitrile (ACN). The presence of C_Q in series with C_{dl} is expected to result in a total measured capacitance $C_{meas}= (C_{dl}^{-1}+C_Q^{-1})^{-1}$. We found that C_{meas} in defected FLG increased for either electrolyte, which may be rationalized in terms of the higher C_Q (= e^2*DOS (E_F), where e is 1.6 x 10^{-19} C), resulting from a dopant-induced increase in DOS(E_F).[59] Although C_{meas} increased for either electrolyte, $TEABF_4$ showed a much higher enhancement than $TBAPF_6$ (almost twice for the highest defect concentration). Such an observation concurs with our DFT calculations, which showed that TEA^+ ions are more suitable for accessing the interlayer spacing in FLG through nanopores. It should be noted that the nanopores in plasma-treated FLG (**Fig. 3.3.3a**) are sufficiently large to allow both TEA^+ and TBA^+ ions. However, the relatively smaller size of TEA^+ (0.45 nm) compared to TBA^+ (~0.8 nm) facilitates easier access to the inter-layer space in FLG, resulting in a higher capacitance.

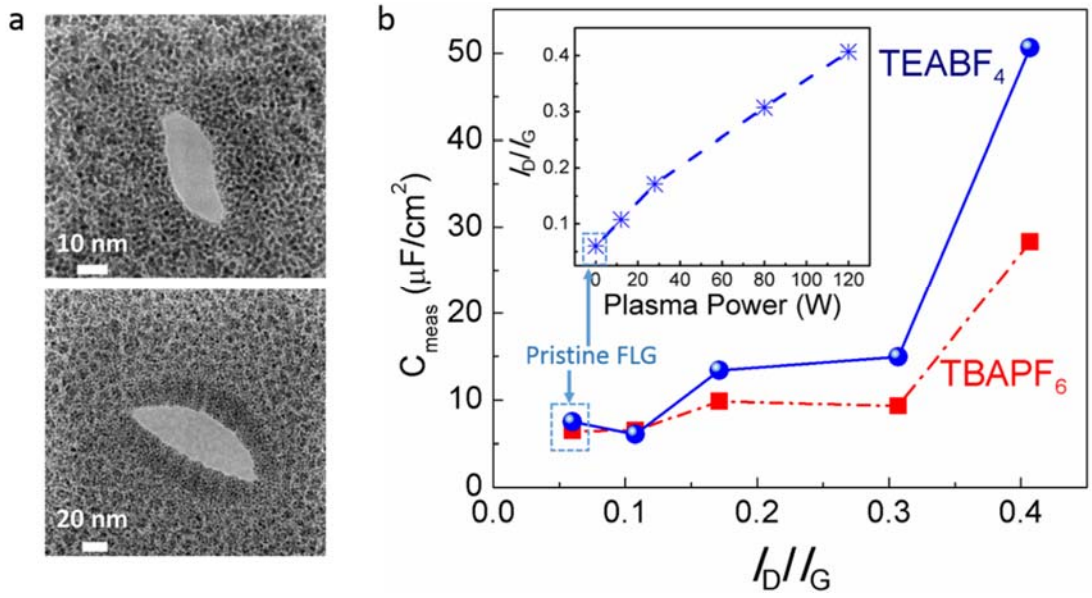

Figure 3.3.3: The experimental validation of DFT results. (a) Transmission electron microscopy (TEM) images of the nanopores created in FLG by exposure to Ar^+ ions for 2 min (power varied from 0 - 120 W). (b) The change in total measured capacitance (C_{meas}= $(C_{dl}^{-1}+C_Q^{-1})^{-1}$) as a function of defect densities (measured by I_D/I_G ratio, where I_D and I_G represent the integrated areas of the Raman *D*- and *G*-bands, respectively) for FLG samples in the presence of: i) 0.25 M tetraethylammonium tetrafluoroborate ($TEABF_4$) in acetonitrile (blue dots and solid line), ii) tetrabutylammonium hexafluorophosphate ($TBAPF_6$) in acetonitrile (red squares and dash line). Inset: I_D/I_G as a function of the Ar^+ plasma power shows a nearly linear dependence.

3.4. Effects of N-doping on electrochemical properties of graphene

3.4.1. N-doping for improved power and energy density

While the plasma etching of FLG significantly improves the measured capacitance and the energy density (= $0.5C_{meas}V^2$, where V is the voltage), the increased I_D/I_G compromises the power density due to an increase in the Warburg resistance (see **Fig. 3.1.1**). Furthermore, the presence of pores in the graphene severely weakens its structural integrity and thereby deteriorates the durability of the electrodes, and will be discussed later in **Fig. 3.5.1**. Alternatively, the rich chemistry between carbon and nitrogen could be used to introduce N-dopants into graphene lattice in order to increase C_Q, C_{meas}, and energy density similar to nanopores, and yet retain intrinsic electrical conductivity and structural integrity of graphene. We prepared three different N-doped FLG using the CVD method (see **Section 3.2.2**) for achieving SCs with high energy and power densities. As shown in **Fig. 3.4.2a**, N-dopants can be found in at least three different configurations, viz., graphitic, pyridinic, and pyrrolic. We analyzed the configuration stability, electron density, and DOS profiles (see **Fig. 3.4.2b**) for all configurations using DFT calculations. We and others previously showed that all the configurations exhibited positive formation energy values (i.e., energy released upon the formation of the structure from free atoms) suggesting that the doped sheets are stable.[62,76] The introduction of the dopants changed the symmetry of the lattice and resulted in drastically different DOS(E_F) for all the three configurations (**Fig. 3.4.2b**). Specifically, the DOS(E_F) for the pristine sample is negligible due to its semi-metallic nature while all other samples showed non-zero DOS(E_F), with a very high

DOS(E_F) for pyrrolic configuration. The increase in DOS(E_F), in addition to the fact that the pyrrolic type defects mimic the behavior of nanopores through extended defects (e.g., multiple vacancies) is useful for increasing both energy and power density of SC electrodes.

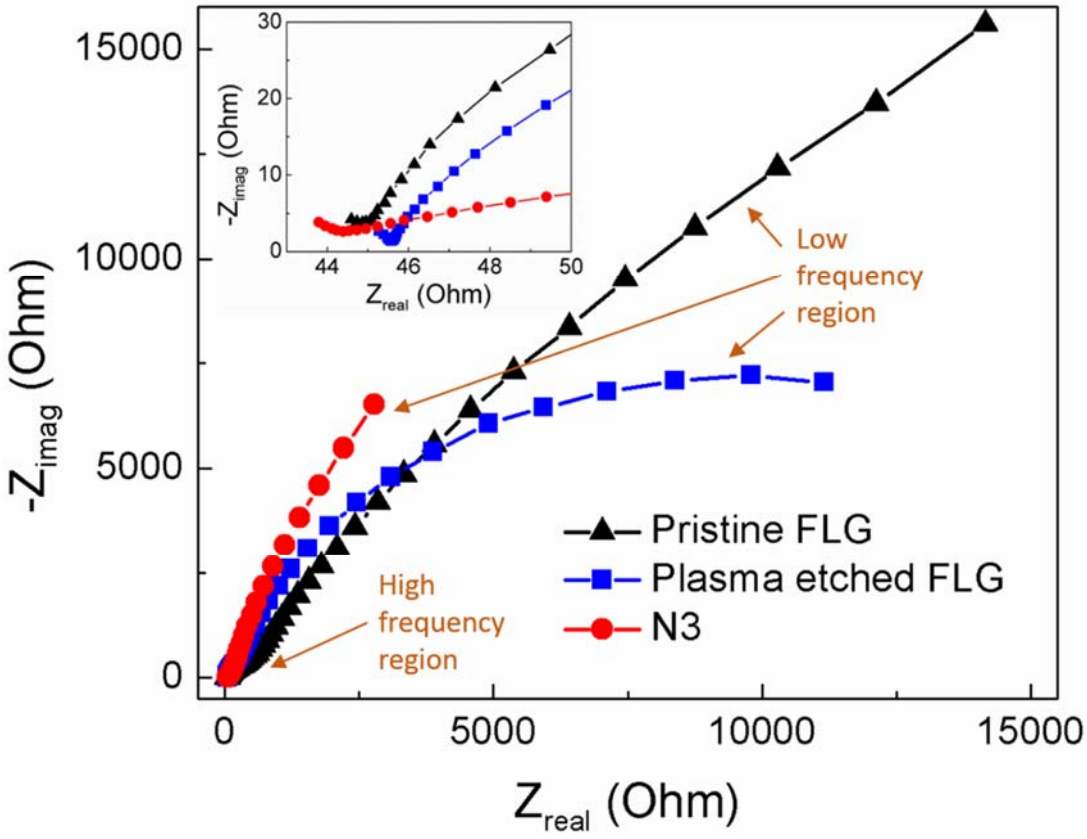

Figure 3.4.1: Nyquist plots of electrochemical impedance spectroscopy (EIS) for pristine FLG, Ar^+ plasma etched FLG, and N3 (or pyrrolic N-doped graphene) measured from 0.1 Hz to 100 kHz. Electrolyte: 0.25 M tetraethylammonium tetrafluoroborate ($TEABF_4$) in acetonitrile. Inset: Magnified Nyquist plots for the high frequency region. It can be seen

that the plasma etched FLG has slightly higher equivalent series resistance (indicated by the first intercept of the Nyquist plots on the real axis[77]) and interfacial charge transfer resistance (represented by the radius of the semi-circle at the high frequency region) from the high frequency region. Interestingly, the slope of data in the low frequency region, which depends on the electrolyte diffusion resistance (Warburg resistance R_w), is different for all three samples.[78,79] The higher slope indicates better ion diffusion within the electrodes.[56,80] Clearly, the plasma etched samples exhibit high Warburg resistance, which could be attributed to the tortuous diffusion path of ionic species through defect-induced pores. However, sample N3 exhibits lower R_w due to the presence of N-dopants in the pyrrolic configuration.

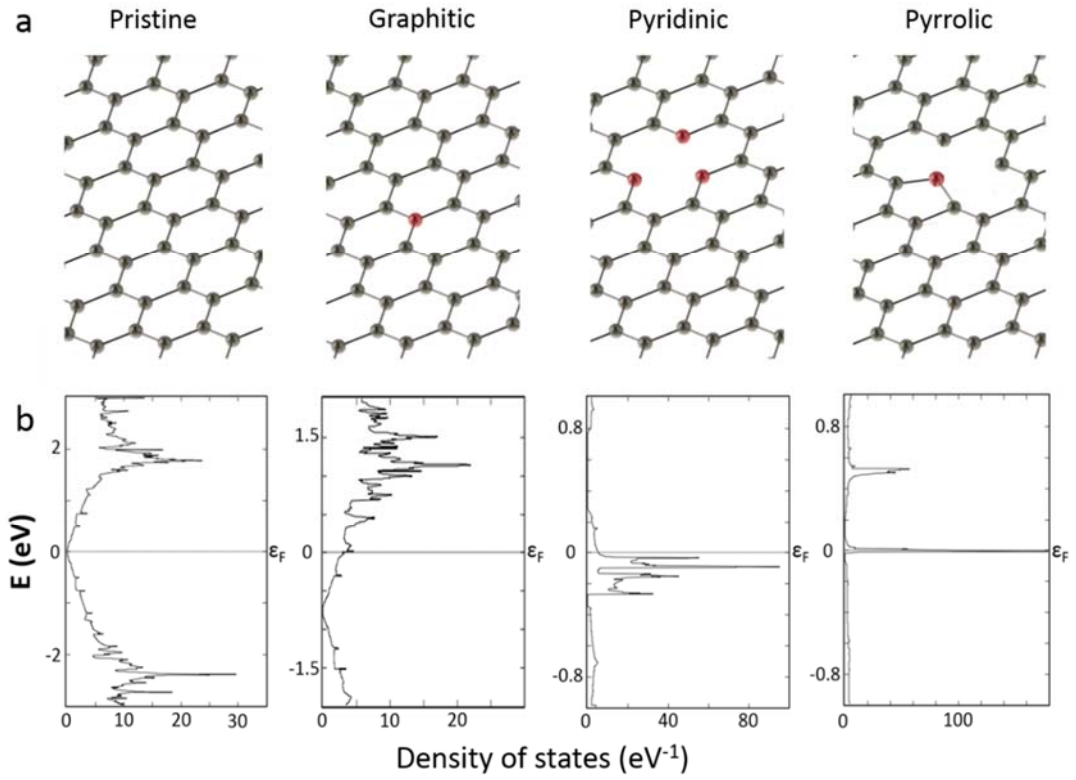

Figure 3.4.2: The influence of N-doping on the electronic density of states. (a) A schematic of different N-dopant configurations in graphene. The black and red spheres represent the carbon and nitrogen atoms, respectively. (b) The electron density of states (DOS) for pristine, graphitic, pyridinic, and pyrrolic graphene (5x5 unit cells) derived from the density functional theory. The DOS at the Fermi level (0 eV) is negligible for pristine graphene while it is very high for pyrrolic graphene.

3.4.2. Characterization of N-doped FLG structures

As shown in **Fig. 3.4.3,** the C *1s* line in the x-ray photoelectron spectroscopy (XPS) data of FLG exhibited a peak maximum at the binding energy of 284.45 eV. Upon N-

doping, the C *1s* line was observed to broaden and upshift (0.15–0.35 eV). The presence of different doping configurations was confirmed by deconvolution of the N *1s* line using Voigtian components. The peak located at 401.7 eV (**Fig. 3.4.3b**) is identified with substitutionally doped nitrogen in the graphitic bonding configuration (in sample N1-N3). The peaks present at 398.6 (in sample N1 and N2) and 400.1 eV (in sample N3) arise from nitrogen bonded in the non-graphitic configuration, and were previously attributed to pyridinic and pyrrolic doping configurations, respectively.[10] Based on our XPS studies, we estimated the N-dopant concentrations in our samples to be ~2 at.%. Although the samples N1-N3 have all three dopant configurations (viz., graphitic, pyridinic, and pyrrolic), it should be noted that graphitic (/pyrrolic) configuration is predominant in N1 (/N3). We found that both pyridinic and graphitic configurations are predominant in N2. In addition to XPS confirmation, the Raman spectrum of N-doped graphene (**Fig. 3.4.4**) showed clear evidence for intense *D* & *D*'-bands for N2 and N3 samples, unlike the graphitic dopants in N1, due to the presence of extended defects and vacancies. Previously, we showed that the electron and phonon renormalization in N-doped graphene increases the Fermi velocity (v_F) and thereby influences lattice vibrations locally near a dopant.[10] Indeed, a combination of micro-XPS and micro-Raman spectroscopy revealed that the local renormalization effects in N-doped graphene resulted in an effectively downshifted Raman 2*D* band (**Fig. 3.4.5**) with a large shift for N2 and N3 samples and a negligible shift of N1 in agreement with our previous studies. [10]

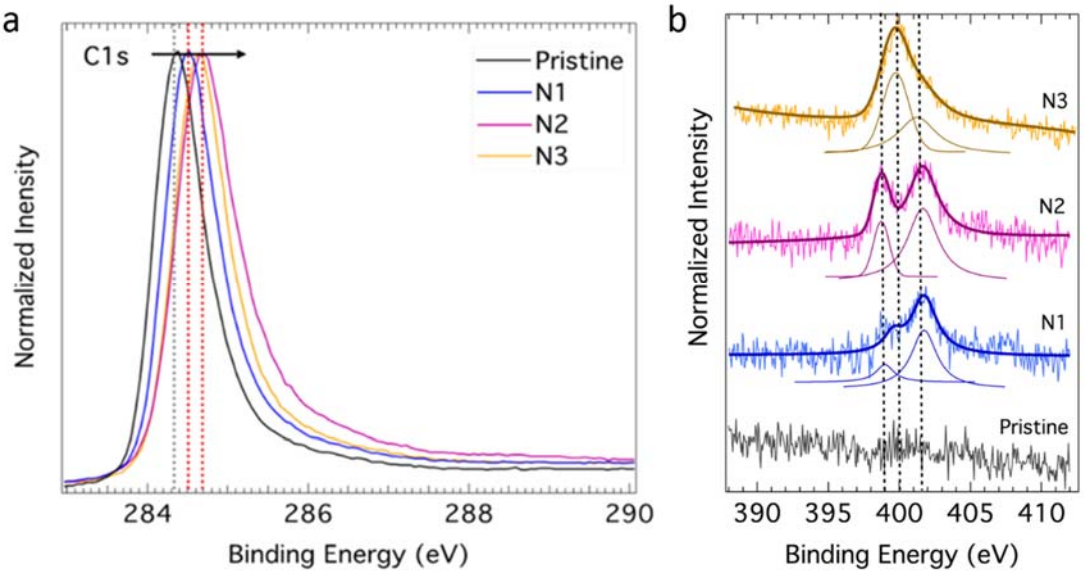

Figure 3.4.3: X-ray photoelectron spectroscopy for pristine and N-doped graphene, a) C 1s line, and b) N 1s line.

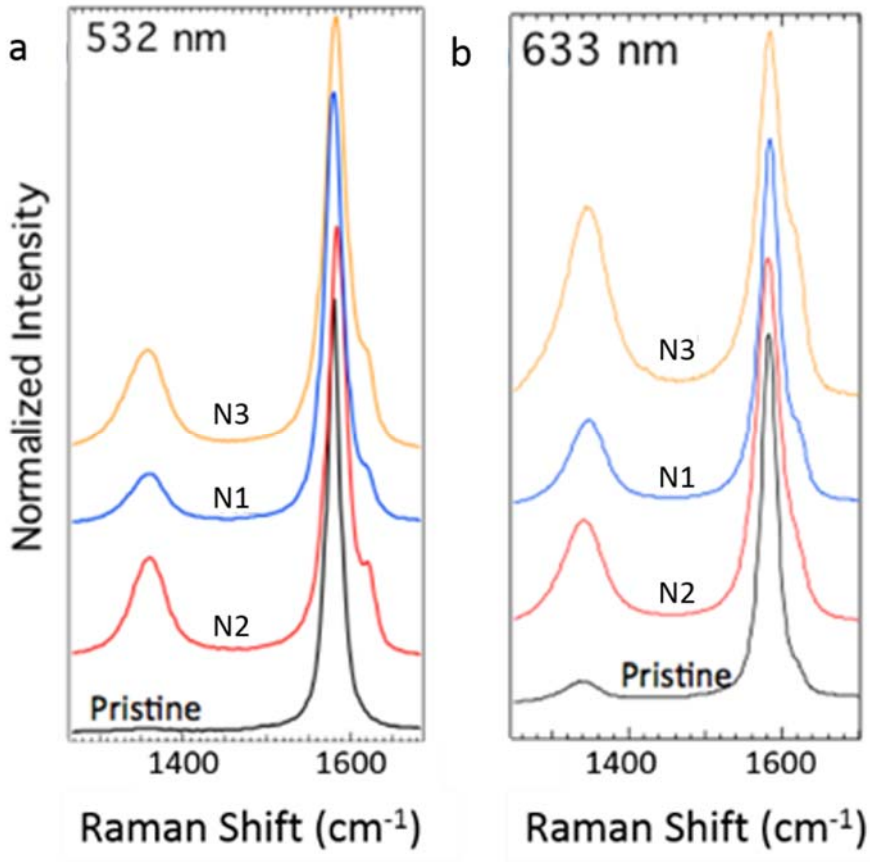

Figure 3.4.4: The *D* and *D*'-bands for pristine and N-doped few layer graphene (grown using chemical vapor deposition) at excitations a) 532 nm and b) 633 nm. The *D* and *D*′ bands are intense for samples N2 and N3 (non-graphitic doping configuration). The *D* band for N1 (graphitic doping configuration) is, however, relatively less intense.

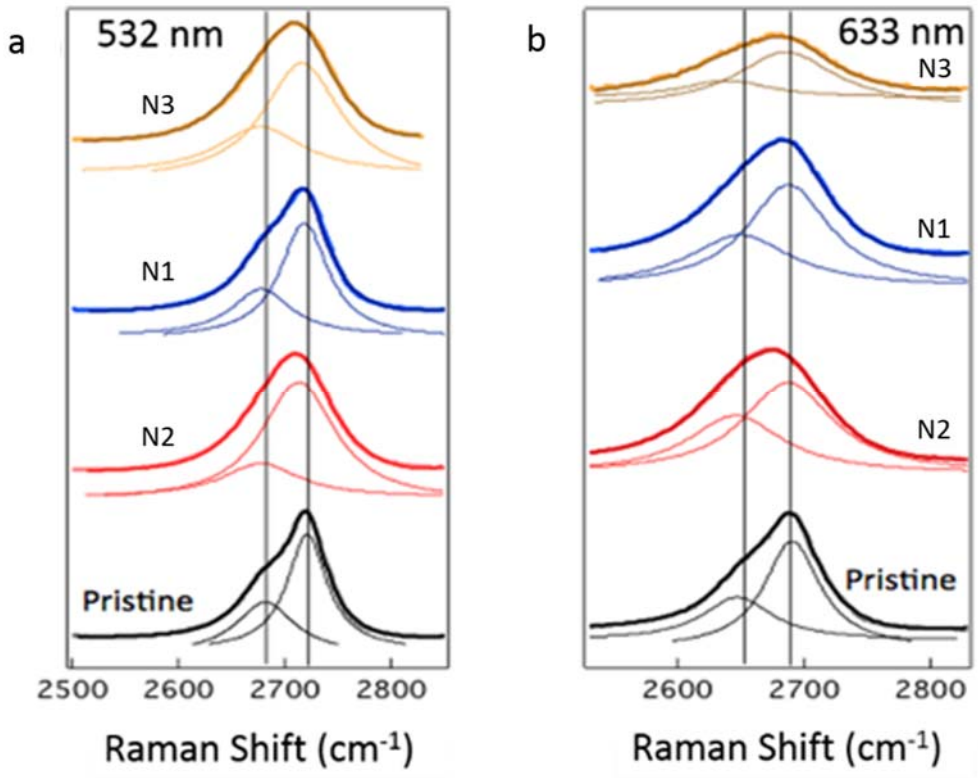

Figure 3.4.5: The 2*D*-band for pristine and N-doped few layer graphene (grown using chemical vapor deposition) at excitations a) 532 nm and b) 633 nm. The vertical lines in both panels serve as a guide to the eye. The electron-phonon-renormalization upon doping leads to a net down-shift in the 2*D*-band peak position for samples with a non-graphitic doping configuration. The traces below each spectrum indicate the deconvoluted peaks used for fitting. Clearly, sample N1 retains intense peaks in the 2*D*-band with little downshift at both excitations.

3.4.3. Electrochemical characterization of N-doped FLG

For elucidating the influence of dopant configuration on C_{meas}, we performed CV measurements on the pristine, N1, N2, and N3 samples in the three-electrode setup with previously identified 0.25 M $TEABF_4$ in ACN. As shown in **Fig. 3.4.6a**, the absence of redox peaks in the CV plots indicate the lack of specific reactions and pseudocapacitance arising from charge transfer at the N-doped graphene /electrolyte interface. Clearly, we observed that the C_{meas} values for N-doped FLG were higher than that of pristine FLG, and sample N3 (pyrrolic) was significantly different from samples N1 and N2, as predicted by our DFT calculations (see **Fig. 3.4.6b**). We measured at least 5 different sets of samples to confirm the results presented in **Fig. 3.4.6**. The controlled growth of a specific dopant configuration is highly difficult. Thus, to validate the hypothesis that the increase in C_{meas} originates from pyrrolic configuration, we annealed the plasma etched FLG samples with nanopores in a 1" quartz tube furnace at 400 °C for 1 hr in Ar bubbled through ACN (see **Section 3.2.2** for more details) into the furnace, or only Ar. We found that the Ar-annealed FLG exhibited a slight decrease in C_{meas} due to a decreased I_D/I_G upon annealing, as shown in **Fig. 3.4.7**. However, Ar-ACN annealed FLG showed a marked increase in C_{meas} and concomitant decrease in resistivity due to the introduction of N-dopants. It is noteworthy that pristine FLG annealed in Ar or Ar-ACN did not show any changes in C_{meas} suggesting that the initial defects in the form of nanopores facilitated the introduction of N-dopants. Our detailed XPS characterization of Ar-ACN samples also revealed the presence of non-graphitic dopants similar to CVD grown samples (see **Fig. 3.4.8**). Specifically, we observed

the presence of N-dopants in pyrrolic and pyridinc configurations, which resulted in increase of DOS(E_F) similar to CVD grown N-doped samples (N1-N3).

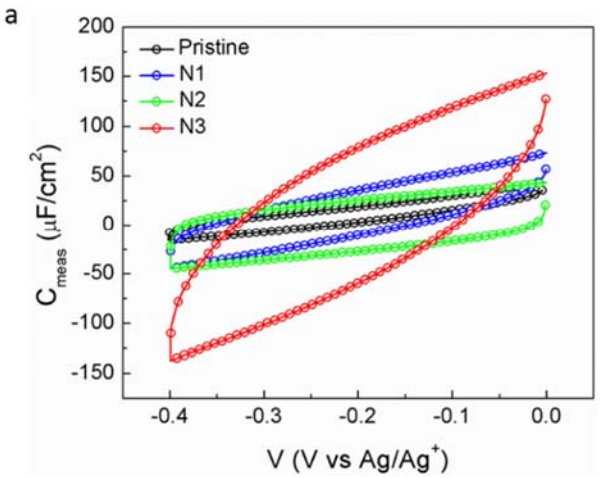

b

Sample	C_{meas} (μF/cm^2)
Pristine	7.5
N1	20.5
N2	24.6
N3	56.6

Figure 3.4.6: N doping leads to increased capacitance. (a) Cyclic voltammetry (CV) curves (normalized by scan rate = 1000 mV/s) for pristine and different N-doped FLG obtained in 0.25 M tetraethyl ammonium tetrafluoroborate ($TEABF_4$) in acetonitrile. b) The total value of C_{meas} for different FLG structures derived from (a).

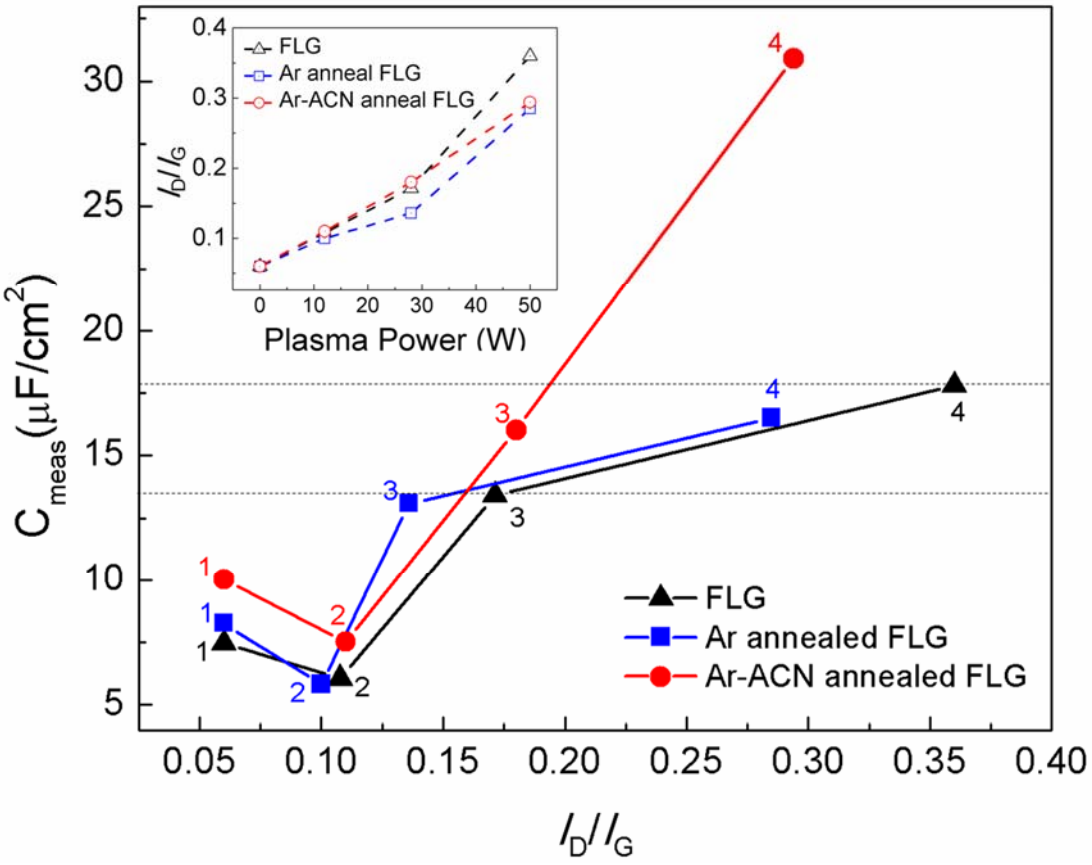

Figure 3.4.7: The change in total measured capacitance (C_{meas}) as a function of Ar^+ plasma power for FLG, Ar annealed FLG and Ar-ACN annealed FLG in the presence of 0.25 M tetraethylammonium tetrafluoroborate ($TEABF_4$) in acetonitrile. The numbers 1-4 denote FLGs treated by plasma power of 0, 12, 28, 50 W respectively, prior to annealing or electrochemical measurements. Inset: The ratio of intensity of *D*-band to the intensity of *G*-band (I_D/I_G) as a function of plasma power.

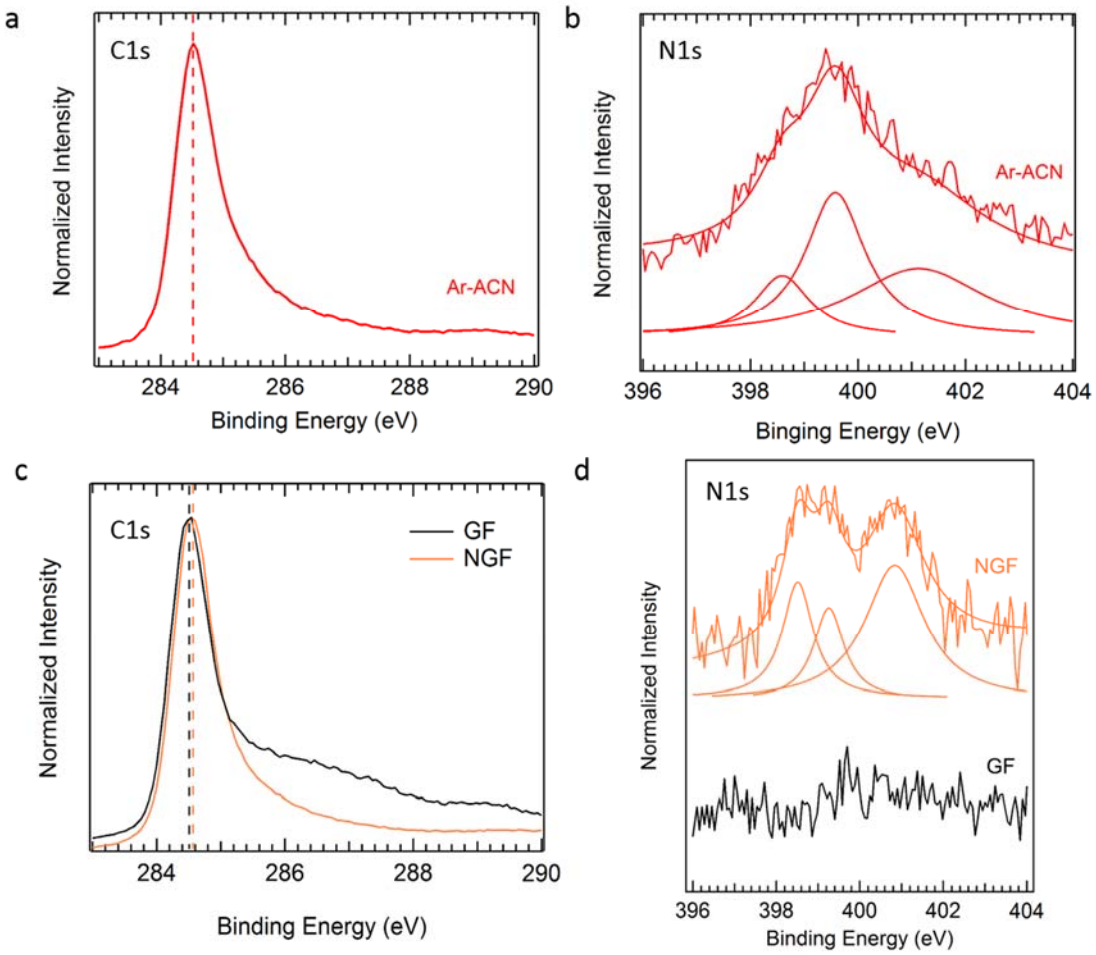

Figure 3.4.8: X-ray photoelectron spectroscopy for (a, b) Ar-ACN annealed FLG treated by 50 W Ar^+ plasma etching, and (c, d) pristine and N-doped GFs. We estimated the N-dopant concentrations in our samples to be ~2.5 at. %.

3.5. Realization of high energy and power densities SC devices with defect-engineered graphene electrode

Building on the improved performance of the N-doped FLGs, we successfully constructed a coin-cell made of CVD grown graphene foams. It should be noted that SC devices based on CVD grown graphene have been limited to substrate-based micro-capacitors.[81,82] For the first time, to overcome this limit for bulk device applications, we synthesized large quantities of pristine FLG foams on Ni foam using the CVD method (see **Section 3.4.2**). The obtained GFs were etched through the Ar^+ plasma processing (for convenience, referred to as PGFs in **Fig. 3.5.1**) at 120 W for 2 min for inducing nanopores (*cf.* **Fig. 3.3.3)** and subsequently subjected to a post doping process through Ar-ACN annealing for producing N-doped GFs (NGFs in **Fig. 3.5.1**). We fabricated symmetric coin cells with GF electrodes with a polymer separator placed in between the two electrodes. The GF electrode-separator-electrode sandwiched structures were assembled in a coin cell apparatus, as shown in the inset of **Fig. 3.5.1a**. The CV profiles of the as-assembled coin cells (with three different electrodes viz., pristine GFs, PGFs, and NGFs) with 0.25 M $TEABF_4$ electrolyte are shown in **Fig. 3.5.1a**. Clearly, while the PGFs showed a two-fold increase in C_{meas} over pristine GFs, NGFs exhibited a five-fold increase. Galvanostatic charge-discharge measurements were carried out to calculate the energy and power density of the coin cells using $W = 1/2C_{meas}V^2$, where W is the energy density and V is the cell voltage, and $P = dW/dt$, where P is the power density and dt is the discharge time. The charge–discharge characteristics of N-doped GF coin cells at 5 mA/cm^2 are shown in **Fig.**

3.5.2. The specific energy and power densities are calculated by normalizing the *W* and *P* value by the total coin cell volume of the two electrodes shown in a Ragone plot (**Fig. 3.5.1b**). The energy and power density values (**Fig. 3.5.1b**) for the pristine and PGF devices are on par with the traditional SCs (e.g., commercially available activated carbon SCs),[83] indicating our CVD grown GF is applicable in real energy storage devices. As shown in the Ragone plot in **Fig. 3.5.1b**, the power density of PGF cells did not show much improvement and is indeed lower than pristine GF cells at low energy density due to increased resistance. On the other hand, NGF devices exhibited an enhanced energy density (~5 times over activated carbon SCs) without compromising power density, which brings them closer to Li-ion thin film batteries in performance.[81]

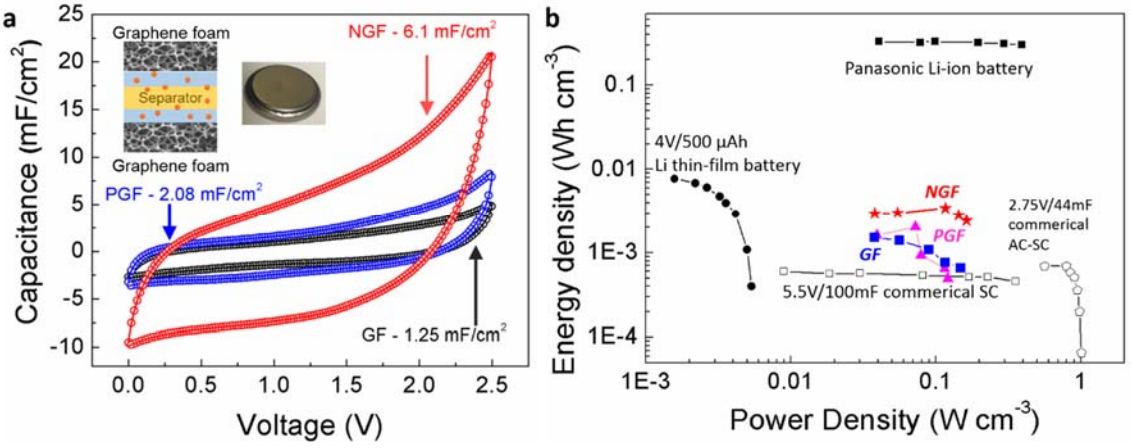

Figure 3.5.1: N-doped graphene foam-based coin cells with high-energy and power-densities. (a) Cyclic voltammetry (CV) curves (normalized by scan rate = 1000 mV/s) for pristine, PGF and NGF coin cell devices obtained in 0.25 M tetraethyl ammonium

tetrafluoroborate (TEABF4) in acetonitrile (ACN). (b) Ragone plot comparing the performance of GF coin cell devices with 0.25 M $TEABF_4$-ACN electrolytes to conventional supercapacitors, Li-thin film batteries, and other energy storage devices. [81,83]

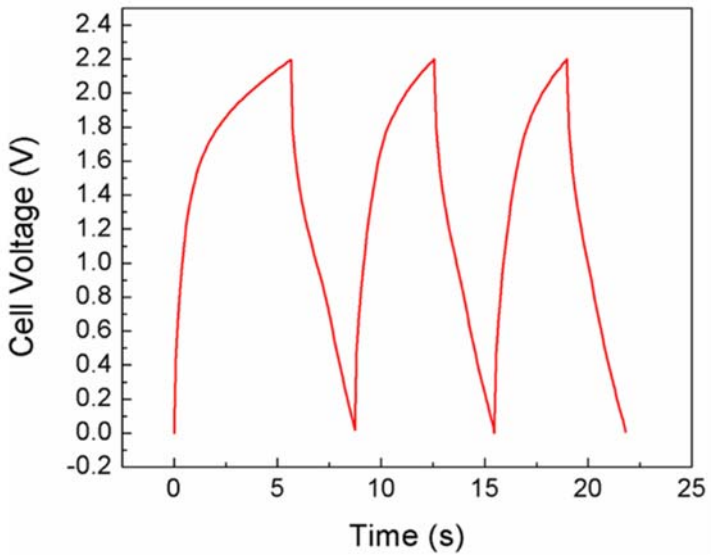

Figure 3.5.2: The charge–discharge characteristics of N-doped GF coin cells at 5 mA/cm^2.

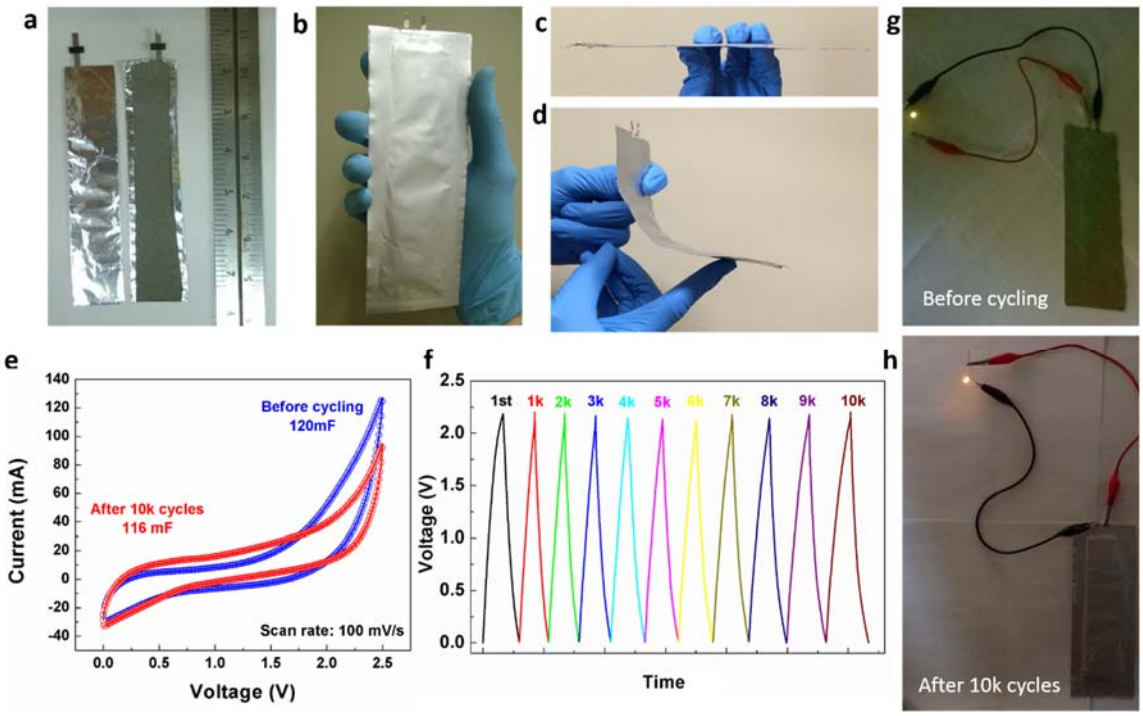

Figure 3.5.3: Graphene foam-based pouch cells for realistic applications. (a-d) Photographs showing flexible and compact graphene foam based pouch cells with high form factor and (e, f) high cycle stability. The pouch cells showed only an insignificant drop in total capacitance <4% after 10,000 cycles and can be used for practical applications such as LED lighting (g, h).

One of the bottlenecks in the integration of SCs into pocket-sized and compact instruments has been their form factor [84]. In this regard, flat, thin, and flexible SCs with rectangular or square in shape are of interest to the industry. As shown in **Fig. 3.5.3**, we fabricated flexible and compact pouch cell devices (total capacitance >100 mF) for realistic applications such as LED lighting using only graphene foams prepared via a scalable CVD

process[85] (**Figs. 3.5.3a-d**). We observed that the performance of the SC pouch cells comprised of both pristine and doped graphene foams was stable for over ten thousand cycles (unlike PGFs) with an insignificant drop of <4% in performance (**Figs. 3.5.3e and f**).

3.6. Conclusions

Defects are generally perceived as material performance limiters.[86–88] Contrary to this established notion, we demonstrated that the appropriate defect configuration could indeed alleviate roadblocks in harnessing the true energy storage potential of FLG. From a theoretical standpoint, defects in FLG break the crystal symmetry and thereby change the DOS(E_F), which in turn significantly increases C_Q.[59] The small C_Q is an intrinsic limitation that impedes FLG-based SCs from delivering high-energy density.[59–61] In addition to the increase in C_Q, the choice of the right electrolyte could enable the transport of ionic species through nanopores allowing access to otherwise unused interlayer spaces in FLG. [65–72] In this work, we used a simple plasma etching process to induce defects in CVD-grown FLG structures and experimentally demonstrated an increase in C_{meas}. Although the C_{meas} in defected FLG is increased by 150% (from 21 μF/cm^2 to ~50 μF/cm^2)[55], the presence of defects in FLG severely weakens the structural integrity and compromises the power density. Indeed, we found that the defected FLGs cannot be cycled beyond 100-500 cycles, which is a serious limitation for SC devices. To overcome this challenge, we used the rich carbon and nitrogen chemistry to induce N-dopants into

graphene lattice. Our comprehensive characterization and theoretical calculations showed that the non-graphitic dopants increase C_Q by changing DOS(E_F) and yet retain the necessary electrical conductivity and structural integrity. In the case of pyrrolic N-dopants, we achieved a significant enhancement in C_{meas} ~56 μF/cm^2 without using any pseudo-capacitive materials. The validity of our results is further reinforced by the experiments on ACN annealed defected FLG structures. The nanopores in defected FLG acted as a site for incorporating N-dopants into the graphene lattice and thereby exhibited an increase in C_{meas}, conductivity, and durability similar to CVD grown *in situ* doped N-doped FLGs.

While these results are exciting from a fundamental physics perspective, these developments would be futile if they cannot be extended to real-time devices with clear scalable manufacturing strategies. In this regard, we used CVD to synthesize GFs in bulk quantities and prepared coin and pouch cell devices. We induced pores in GFs through plasma etching and subsequently annealed them in ACN to achieve NGF-based coin cells with significantly higher energy and power densities than commercial SC devices. The CVD growth, plasma etching, and subsequent annealing are amenable for roll-to-roll production and are already being used for graphene production at industrial scales. Our results show new ways to tackle the inherent limitations of energy storage in nanocarbons by increasing C_Q and accessible surface area through defect engineering without compromising the intrinsic properties of graphene, which opens a new paradigm for energy storage.

CHAPTER 4

ROLE OF DEFECTS AND DOPANTS ON THE MAGNETIC PROPERTIES OF S-DOPED GRAPHENE

4.1. Introduction

Carbon nanomaterials are regarded as one of the best-suited platforms for spintronics due to their low density, inherently low spin-orbit coupling, and large spin-flip scattering lengths [89,90]. Ideally, any sp^2 carbon system is expected to exhibit diamagnetic behavior due to the existence of π-electron orbital magnetism [91]. However, the origin of anomalous ferromagnetic ordering and paramagnetic response in sp^2 carbon systems has puzzled researchers for many decades [92–94]. This unexpected presence of magnetic ordering in nanocarbons is a major impediment for realizing long spin-flip scattering lengths required for spintronic applications. Although there have been many efforts to understand the presence of magnetism in pure carbon-based nanomaterials [95–100], many of them have been either controversial or irreproducible. This is likely due to the presence of unintentional magnetic impurities (e.g., residual Fe catalyst particles in carbon nanotubes), poorly characterized defects, and intrinsic topology (e.g., curvature in C_{60} and nanotubes). Graphene, a two-dimensional atom-thick layer of sp^2 carbon, is well suited for elucidating the origin of magnetism due to its fairly simple honeycomb lattice with unique electronic and optical properties [26,101]. Furthermore, the properties of many

carbon nanomaterials (e.g., fullerenes, carbon nanotubes, graphite, and some polycyclic aromatic molecules) are often theoretically derived from their underlying graphene lattice.

Many theoretical studies have predicted that point defects in graphene exhibit a non-zero magnetic moment, which can possibly interact with each other resulting in a long-range ferromagnetic ordering [95–97,102–106]. Nair *et al.* reported a purely paramagnetic behavior in highly defective fluorinated and ion-irradiated graphene, implying the absence of any defect-defect interactions leading to ferromagnetic (FM) ordering [9,107]. On the contrary, others have observed signatures of FM in defected graphene indicating possible interactions between defect-induced magnetic moments [108–110]. Collectively, both intrinsic defects (e.g., vacancies and edges) and extrinsic dopants (e.g., fluorine dopants, ion-irradiation induced pores, and unintentional magnetic impurities) have been proposed to increase paramagnetic response of graphene, and in some cases even cause FM ordering through defect-defect interactions. As we and others have previously shown, the nature of defects plays a critical role in an unexpected magnetic ordering in many nanostructured materials (particularly, nanograined oxides) derived from non-magnetic bulk, for example ZnO [111–114]. Accordingly in this chapter, we report controllably doped graphene nanoplatelets (GnPs) with sulfur (an extrinsic defect) to tune different magnetic interactions between intrinsic (e.g., between vacancies) and extrinsic defects (e.g., vacancy and S-dopant). Our X-ray photoelectron spectroscopy (XPS) studies as well as density functional theory (DFT) clearly evince the formation of covalent bonds between S dopants and intrinsic defects. While we observed that pristine GnPs prepared using the chemical

exfoliation method exhibited a weak FM ordering due to the presence of intrinsic defects, we found that the FM ordering systematically decreased with increasing S dopants suggesting that the interactions between S-dopants and intrinsic defects demagnetize GnPs.

4.2. Experiment and calculation methods

4.2.1. Synthesis of S-doped graphene

Grade M GnPs (xGnP-M-5, 99.95 at. % carbon and 0.05 at. % sulfur, see **Table 4.2.1**) were purchased from XG Sciences, Inc. (Michigan, USA). Pristine GnPs consist of short stacks of graphene sheets with an average thickness of approximately 6-8 nm and average size of 5 μm (see **Fig. 4.2.1**). The elemental composition of grade M GnPs from XG Sciences materials safety data sheet are shown in **Table 4.2.1**. The S-dopded GnPs were prepared in two steps, chemical exfoliation process and then sulfur doping process. The schematic of the experimental purcedures are shown in **Fig. 4.2.2**.

Ingredient	CAS #	Wt. %
Graphite	7782-42-5	95 - 100
Sulfur, elemental	7704-34-9	1-5

Table 4.2.1: Elemental composition of grade M GnPs. Source: XG Sciences materials safety data sheet.

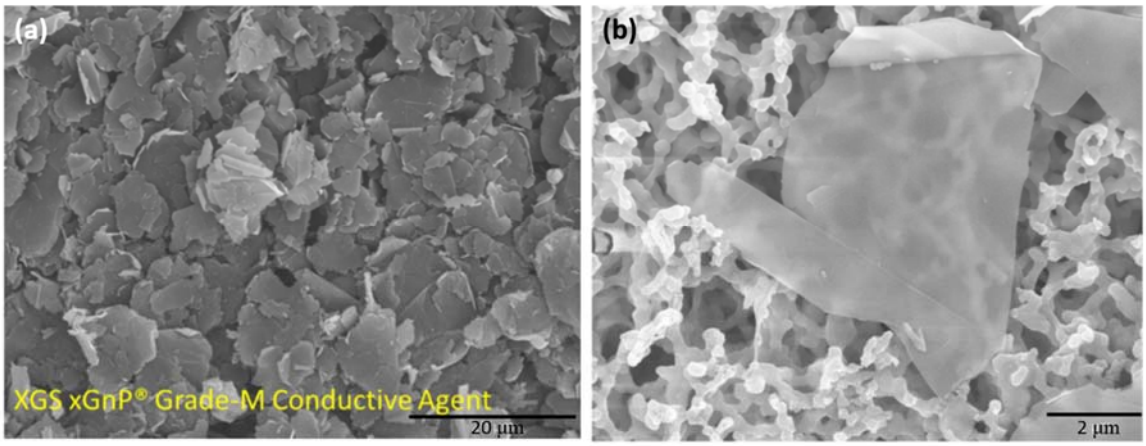

Figure 4.2.1: Scanning electron micrographs of grade M GnPs XG Sciences, Inc. (a) Bulk powder, and (b) Single platelet. Source: XG Sciences materials safety data sheet.

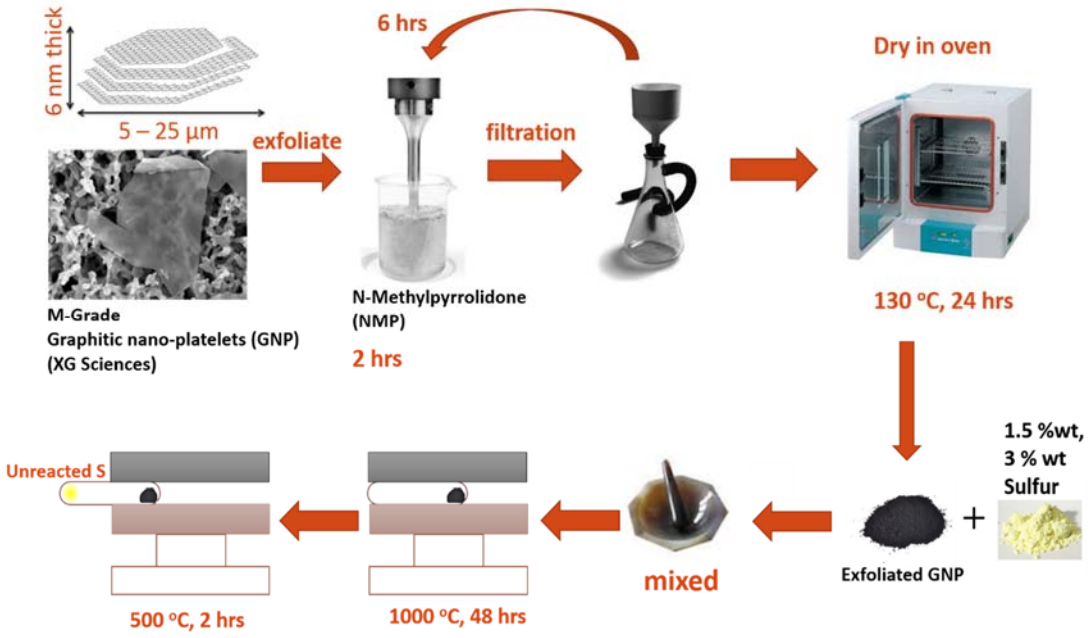

Figure 4.2.2: Schematic of the synthesis purcedure for preparing S-doped graphene.

In the chemical exfoliation process, as-received GnPs (5 g) were exfoliated in 100 ml of N-Methylpyrrolidone (NMP) for 2 hours using a 1/8" tip sonicator at 120 W, and then vacuum filtered using a 0.45µm nylon membrane. Subsequently, the collected "cake" was re-sonicated using a fresh portion of NMP for 6 hours and vacuum filtered. Finally, the vacuum filtered GnPs were washed in water thrice and oven dried at 130 °C for 24 hours.

In the sulfur doping experiment, three 100 mg samples of the exfoliated GnP powders were mixed with 99.5% elemental sulfur, (100 mesh, Alfa Aesar) at nominal concentrations of 1, 1.5 and 3 wt.% of S using a mortar and pestle (labeled as pristine GnP,

1wt.% S GnP, 1.5 wt.% S GnP and 3 wt.% S GnP). The mixed GnP-S samples were vacuum-sealed in quartz tubes (¼" diameter and 6" in length) and annealed in a furnace at 1000 ^{o}C for 24 hours. After cooling down to room temperature, the quartz tubes containing the samples were gently shaken by hand to homogenize the sample, and then reheated again at 1000 ^{o}C for another 24 hours. Subsequently, the furnace was cooled to 440 ^{o}C for 2 hrs and the sealed quartz tubes were partially pulled out of the furnace to facilitate condensation of any unreacted sulfur at the opposite cold end of the sealed tubes.

4.2.2. Charcterization of structure and magnetic properties

The magnetic properties of samples used in this study were measured using a Quantum Design® vibrating sample magnetometer (VSM) and a superconducting quantum interference device (SQUID) magnetometer. The DC temperature dependent magnetic susceptibility was measured both in zero-field-cooled (ZFC) and field-cooled (FC) conditions with temperature ranging from 3 to 150 K. A Dilor XY triple grating monochromator was used for collecting the micro-Raman spectra of all samples with the 514.5 nm excitation from an Ar^{+} ion laser. XPS studies were performed in a Phi spectrometer equipped with a monochromatic Al K_{α} source (1486.6 eV), which has an overall resolution of 0.5 eV.

The samples were tested for magnetic impurities such as Fe through inductively coupled plasma mass spectrometry (ICP-MS) measurements (X series II, Thermo Scientific) using an internal standard containing Li, Y, and In with a detection limit of 0.05

ppb (corrected for sample dilution). For the measurements, 10 mg of sample was dissolved in 10 ml of 70% nitric acid for 24 hrs under constant stirring. Subsequently, HNO_3 containing graphene was centrifuged, and the supernatant was removed and diluted into 2% HNO_3 for evaluating the presence of Fe impurities.

4.2.3. Calculation methods

The calculations are performed using the projected augmented wave formalism [115,116] of DFT as implemented in the Vienna *ab initio* simulation package [117,118]. The exchange correlation potential is approximated by a generalized gradient approximation using the Perdew-Burke-Ernzerhof functional [119]. The DFT orbitals are expanded in plane wave basis with a relatively high energy cutoff of 600 eV. The vacancies and vacancy clusters are modeled in $10 \times 10 \times 1$ supercells of the two atom unit-cell of graphene (lattice constant: 2.468 Å), with a 15 Å vacuum in the vertical direction. We used a relatively large supercell to reduce the undesired interaction between vacancies and their images arising from periodic boundary conditions. The reciprocal space is sampled with $5 \times 5 \times 1$ *k*-point mesh equivalent to the $50 \times 50 \times 1$ *k*-point mesh for the two-atom unit cell. The same density of *k*-points is used for simulated nano-ribbons with zigzag- and armchair-edges modeled in 160- and 168-atom computational cells, respectively. All the atomic configurations are optimized with spin-polarized DFT.

4.3. Magnetic properties of pristine and S-doped graphene nanoplatelets

As shown in **Fig. 4.3.1**, finite areas of hysteresis loops provide a clear evidence for FM in both pristine and doped GnP samples at 300 and 5 K, with saturation values (M_s) ~0.06 (pristine), 0.017 (1.5 wt.% S GnP), and 0.043 emu/g (3 wt.% S GnP). The FM is embedded in a large diamagnetic (DM) background (see insets in Figs. 3.3.1a and b), which arises from the underlying graphene lattice. Although graphite/graphene is diamagnetic, the presence of defects (as it will be discussed later) induce weak FM, similar to nanograined oxides [111–114]. The observed saturation of FM at relatively low fields (~1.2 kOe at 300 K) for both pristine and doped samples indicates: i) the presence of moderately large spin-clusters, and ii) that the average size of spin-clusters was not affected by doping. The magnetic coercivity (H_c) increased significantly for all samples at 5 K (see **Table 4.3.1**) implying that room temperature thermal activation energy ~25 meV is sufficient to induce spin-flip in all GnP samples. Interestingly, the percent increase in H_c at 5 K (relative to H_c at 300 K) is highest for pristine samples (~250%) and considerably small in doped samples (~20%). Such observations, when juxtaposed with our DFT calculations, could be attributed to dopant-induced passivation of thermal spin fluctuations in unsaturated edge-states of GnPs. Lastly, we observed a non-monotonic decrease of M_s in S-doped samples (see **Table 4.3.1**) confirming that the S-dopants demagnetized GnP samples. Our detailed ICP-MS analysis (**Table 4.3.2**) confirmed that the magnetic response (shown in **Fig. 4.3.1**) is not from magnetic impurities such as Fe, which were found to be < 20 ppb in both pristine and doped samples.

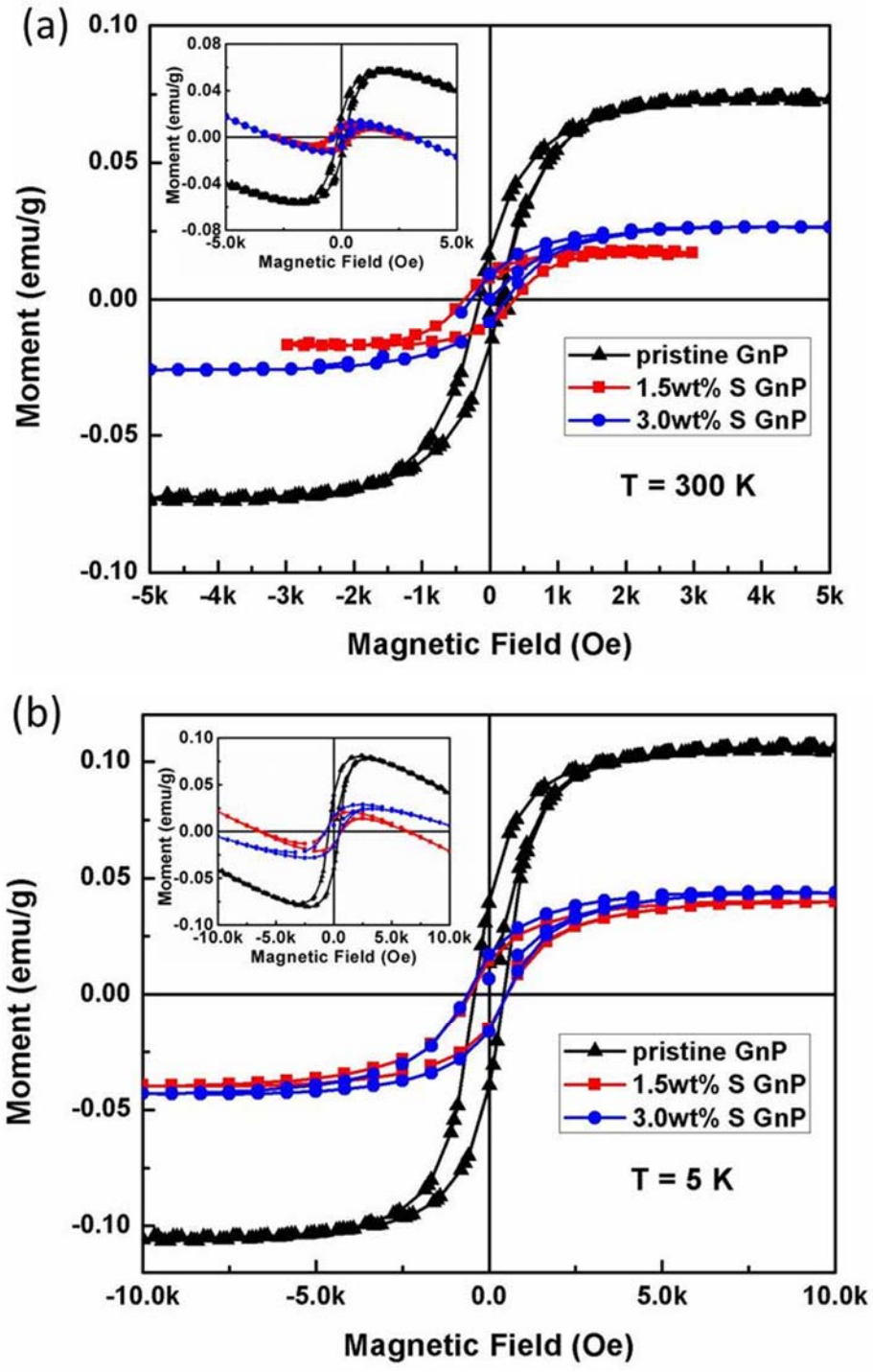
(a)
Moment (emu/g)
Magnetic Field (Oe)
pristine GnP
1.5wt% S GnP
3.0wt% S GnP
T = 300 K
(b)
Moment (emu/g)
Magnetic Field (Oe)
pristine GnP
1.5wt% S GnP
3.0wt% S GnP
T = 5 K

Figure 4.3.1: M-H curves for graphitic nanoplatelets (after accounting for the background diamagnetism) with various S doping concentration measured at (a) 300 K, and (b) 5 K. The insets show the as-measured M-H data.

	T = 300 K			T = 5 K		
	Pristine GnP	1.5 wt.%S GnP	3.0 wt.%S GnP	Pristine GnP	1.5 wt.%S GnP	3.0 wt.%S GnP
M_S (10^{-2} emu/g)	7.3	1.7	2.6	10.6	4.0	4.3
M_r (10^{-2} emu/g)	1.8	0.9	0.9	4.0	1.5	1.7
H_c (10^2 Oe)	1.6	4.6	3.5	5.7	5.5	4.3

Table 4.3.1: The value of saturated magnetization M_S, remnant magnetization M_r and coercivity H_c for pristine, 1.5 wt.% and 3.0 wt.% S doped GnPs under 5 K and 300 K obtained from hysteresis loops. The non-monotonic variation of M_S could result from sample-to-sample variations, and does not affect our conclusion that S-dopants demagnetized GnP samples.

	Pristine GnP	1.5 wt.%S GnP	3.0 wt.%S GnP
Iron concentration (ppb)	17.73	9.39	12.17

Table 4.3.2: ICP-MS analysis of pristine and doped graphene showed only ppb levels of Fe contained in all samples ruling out Fe impurities as a possible cause for the observed magnetic response.

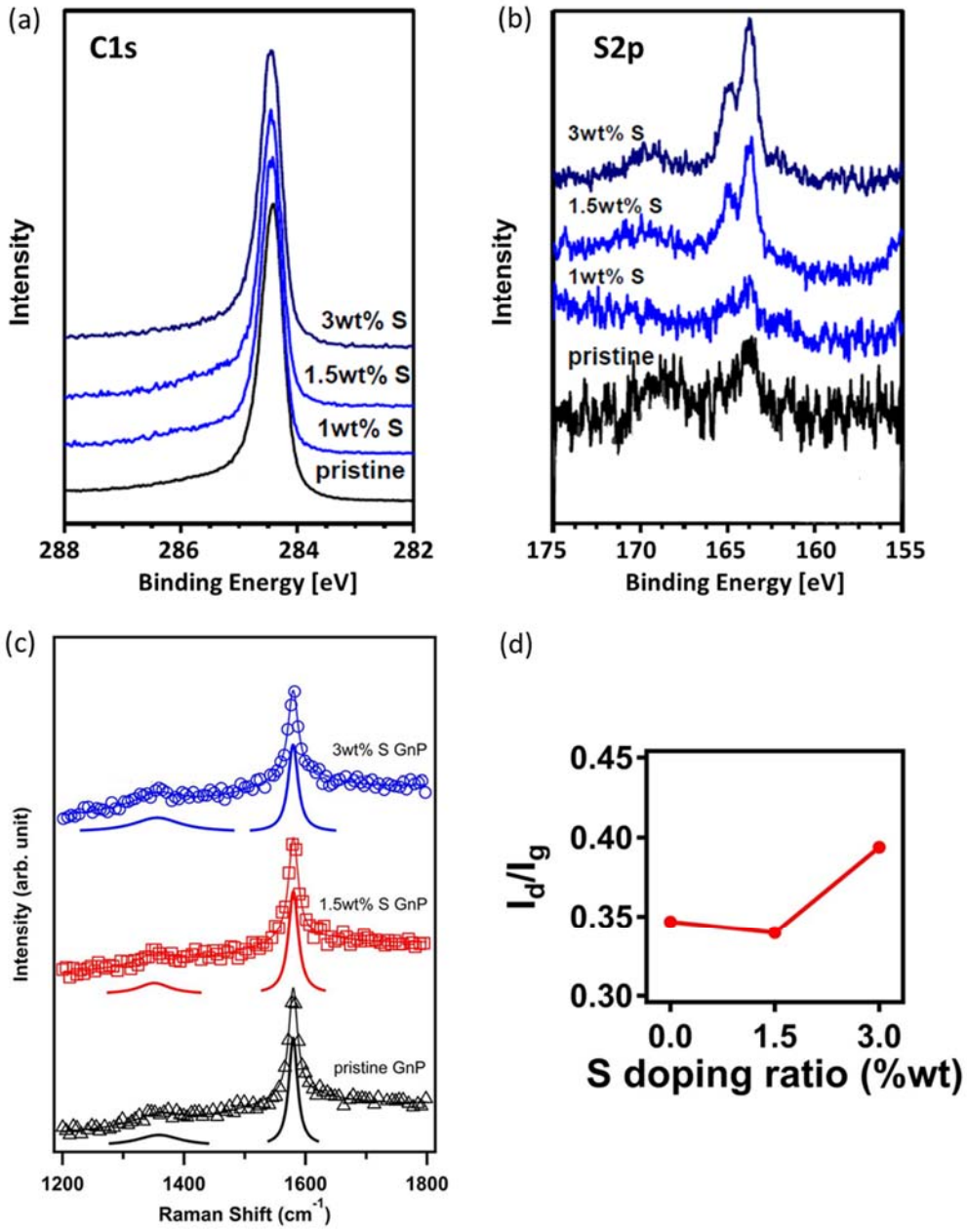

Figure 4.3.2: (a) X-ray photoelectron spectra (XPS) recorded for the C *1s* line with a photon excitation energy of 1486.6 eV for pristine, 1 wt.% S, 1.5 wt.% S as well as 3 wt.% S GnPs .(b) XPS recorded for the S *2p* line with a photon excitation energy of 1486.6 eV.(c)

Micro-Raman spectra of pristine and S doped GnPs. The solid traces below each spectrum represent the deconvoluted fits. (d) The I_D/I_G values for pristine and S doped GnPs.

All samples exhibited an excellent crystallinity as evidenced by the C *1s* peak in the XPS spectra (**Fig. 4.3.2a**). The S-dopant concentration was quantified from the relative photoemission cross-sections for the C *1s* and the corresponding S *2p* peaks (**Fig. 4.3.2b**). We inferred that pristine, 1 wt. % S, 1.5 wt. % S and 3 wt. % S nominal S-doped GnPs contained 0.05, 0.07, 0.18 and 0.25 at. % substituted sulfur, respectively. We limited our magnetization studies to pristine, 1.5, and 3 wt. % samples because the S concentration in the pristine and 1 wt. % S samples were not significantly different (see **Table 4.2.1**). Furthermore, our XPS results suggest that S is substitutionally doped, and the other common forms of S-doping (e.g., SO_2H. SO_3H) are not dominant. The Raman spectrum for pristine GnPs exhibited a weak disorder band (*D*-band) ~1350 cm^{-1} in addition to the graphitic band (*G*-band) ~1585 cm^{-1}(**Fig. 4.3.2c**). As shown in **Fig. 4.3.2d**, S-dopants did not significantly alter the intensity of *D*-band indicating that no additional structural defects (e.g., vacancies or Stone-Wales defects) were created during the doping process (will be discussed later in **Fig. 4.4.2**). Collectively, magnetization measurements, XPS and Raman spectra suggest that S-dopants predominantly altered the nature of intrinsic defects without introducing additional structural defects.

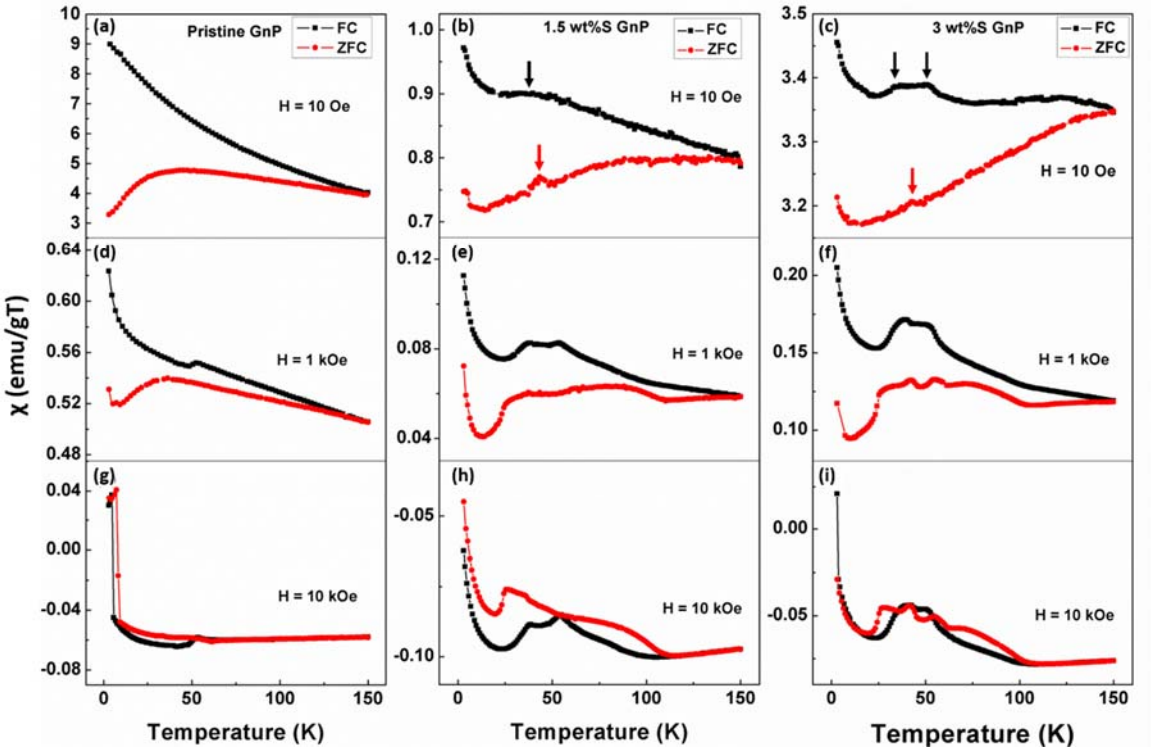

Figure 4.3.3: Temperature dependent ZFC-FC data for (a) pristine GnPs, (b)1.5 wt.% S GnPs, (c) 3 wt.% S GnPs in 10 - 10000 Oe. The down pointing arrows are S-dopant induced antiferromagnetic features as discussed in the text.

The following salient features can be gleaned from the zero field cooled and field-cooled (ZFC-FC data; **Fig. 4.3.3**): (*i*) the low temperature susceptibility (χ) of the pristine GnPs is about 9 times and 3 times higher than that of 1.5 wt. % S GnPs and 3 wt. % S GnPs, respectively, (*ii*) all samples show very strong temperature dependence in FC cycle - χ(T) is larger in FC than in ZFC conditions. This is an evidence for the presence of small superparamagnetic clusters in addition to FM domains, (*iii*) while the FC dependence of pristine GnPs (**Fig. 4.3.3a**) shows a monotonic increase of χ(T) with decreasing

temperature, the ZFC data displays a sharp downturn starting at ~ 38 K, likely due to DM of graphite, (*iv*) the ZFC data for S doped GnPs exhibit a Curie-like upturn instead of the DM downturn in pristine GnPs at ~38 K, implying that S-dopants have significantly changed the magnetic interactions in GnPs, (*v*) two new features at ~45 and 55 K, indicated by arrows in Figs. 3.3.3b and c, which appear upon S doping, are possible signatures for antiferromagnetic domains (**Fig. 4.3.4**) [110,120]. In fact, we observed that the related intensity of the local maxima increased with increasing magnetic field (**Figs. 4.3.3 d-i**), confirming such a hypothesis, and (*vi*) lastly, the splitting between ZFC-FC curves decreased at 10 kOe is consistent with the presence of superparamagnetic clusters in our samples. Interestingly, we observed that the ZFC curve is slightly above the FC (**Figs. 4.3.3 g-i**), which may be attributed to magnetostriction [121]. As evident from **Fig. 4.3.3**, the temperature dependence of χ in S-doped graphene presents several rich and intriguing features, which will be discussed in a separate publication. Nonetheless, in summary, our experimental data suggests that more than one type of magnetic behavior can arise from doping and defects in graphene. Indeed, it is evident that GnP samples exhibit a combination of superparamagnetic, ferromagnetic, anti-ferromagnetic (all arising from defects), and diamagnetic (from graphite) domains making GnP a complex magnetic system to be analyzed.

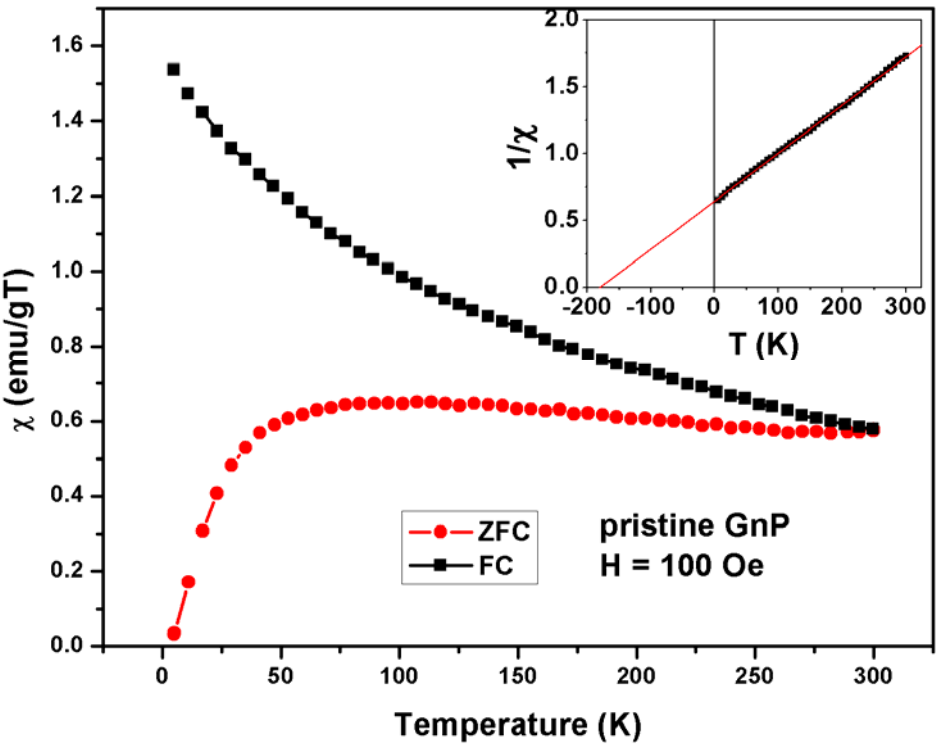

Figure 4.3.4: ZFC-FC curves for pristine GnPs ranging from 3 to 300 K. Inset: Inverse susceptibility vs. temperature from the FC data (soild black squares), shows linear behavior with a negative Curie – Weiss temperature ~ -179 K, indicating the presence of some antiferromagnetic domains.

4.4. Spin-polarized DFT calculations

To further elucidate the origin and dopant-induced changes in the magnetic properties of GnPs, we performed detailed spin-polarized DFT calculations. **Figs. 4.4.1a-e** represent magnetic structures in defected pristine graphene with multiple vacancy

configurations. Upon relaxation, the three dangling-bond sites of the mono-vacancy undergo the Jahn-Teller distortion by breaking the three-fold symmetry, and form a pentagonal and an enneahedral ring of C atoms (**Fig. 4.4.1a**) [122,123]. The relaxed dangling-bond sites constitute an isosceles triangle with two C atoms at the base forming a weak bond, while the largest magnetic moment is presented at the apex. The calculated magnetic moment for the mono-vacancy is 1.4 μ_B and the formation energy is 7.56 eV.

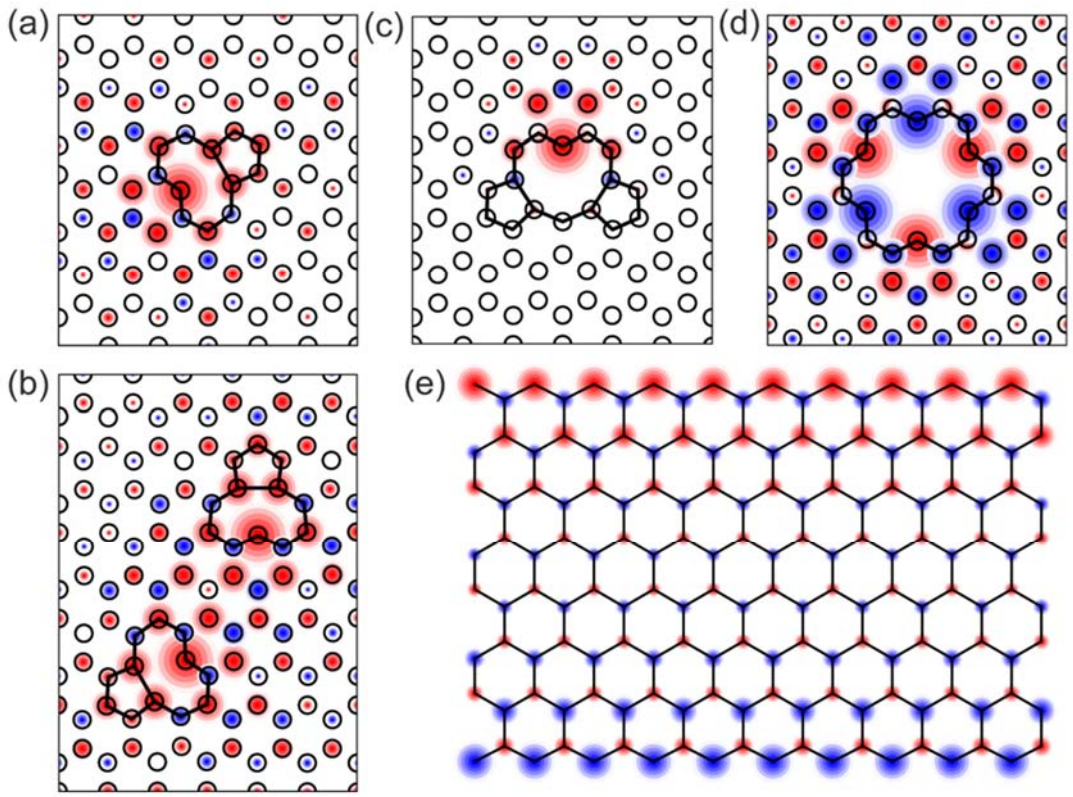

Figure 4.4.1: Magnetic structures in graphene and their local spin density plots: (a) mono-vacancy, (b) two ferromagnetically interacting mono-vacancies, (c) cluster of three vacancies, (d) clusters of six vacancies, and (e) zigzag edges. Up and down local spin

densities are represented by circles with red and blue shades, respectively. The magnitude of local moment is represented proportionally to $\log_{10}$ (radius). The net magnetic moment of each structure is (a) 1.38, (b) 2.91, (c) 0.99, and 0.00 μ_B for (d) and (e).

Similar to the interactions of other types of local magnetic moments in bulk materials, the bipartite character is important in magnetic interactions of vacancies in graphene [124,125]. Multiple mono-vacancies exhibit FM (/anti-FM) interaction if they are in the same (/different) sublattice of graphene, as seen in **Fig. 4.4.1b**. Clustering of multiple vacancies creates a void, and leaves atoms with unpaired electrons (due to dangling-bonds) along the circumference (**Figs. 4.4.1c-d**). Large vacancy-clusters can have many unpaired electrons. However, the net magnetic moment is generally small due to the anti-FM interaction between two sublattices of graphene. Unpaired electrons in the same sublattice of graphene energetically prefer the FM interaction, whereas those in different sublattices favor anti-FM ordering. In the relaxed voids, instant reconstruction of bonds occurs for some atoms with dangling bonds. Hence, the difference between the numbers of dangling-bond sites in two sublattices is generally small, typically one to three. In the case of graphene nano-ribbons, it has been predicted that the zigzag edge exhibits FM ordering as it contains atoms of only one sub-lattice type [105,126–128]. As shown in **Fig. 4.4.1e**, spin moments in GnPs are mainly distributed at the edge carbon atoms, and decay exponentially into the center of the ribbon.

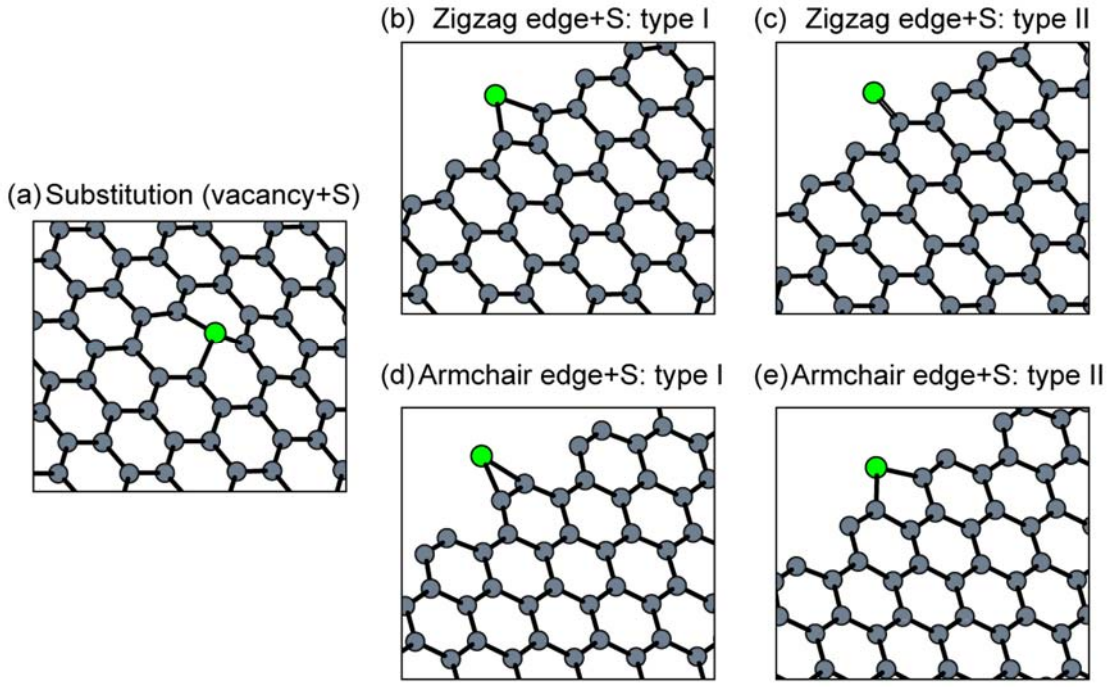

Figure 4.4.2: Optimized bond structures of graphene doped with a sulfur atom (a) occupying a vacant substitutional site, (b) bridging two carbon atoms along the zigzag edge, (c) partial double-bonding with a single carbon atom along zigzag edge, (d) bridging two carbon atoms on the same hexagonal ring along armchair edge, and (e) bridging two carbon atoms on different hexagonal rings along armchair edge.

Our calculations (**Fig. 4.4.2**) show that sulfur atoms are strongly attracted to defected sites of nano-platelets such as vacancy sites and edges, but no adatom-type bonds between S and graphene are found to be stable. We found that a sulfur atom can fill a mono-vacancy, saturate dangling-bonds, and become a substitutional defect, **Fig. 4.4.2a**. The substitutional sulfur relaxes to a non-planar position with z = 1.1 Å. The binding energy

between a sulfur atom and a monovacancy is calculated to be about -6.98 eV, based on E(binding) = E(substitutional S) – E(vacancy) + E(isolated S). Edges of GNPs are also attractive sites for sulfur atoms. **Fig. 4.4.2b-e** show various stable bonding structures between a sulfur atom and zigzag/armchair edges: bridging two carbon atoms on two neighboring hexagonal rings along the zigzag edge, partial double-bonding with a single carbon atom along the zigzag edge, bridging two carbon atoms on the same hexagonal ring along the armchair edge, and bridging two carbon atoms on different hexagonal rings along the armchair edge. Binding energies of these bonding structures are < −3.8 eV, indicating strong attachments of sulfur atoms to edges. The C-S bond lengths in our relaxed structures are in good agreement with the literature values of 1.82 Å for single and 1.72 Å for partial double bonds [129]. The circumferences of voids in the clusters of multiple vacancies provide similar attractive edge-sites.

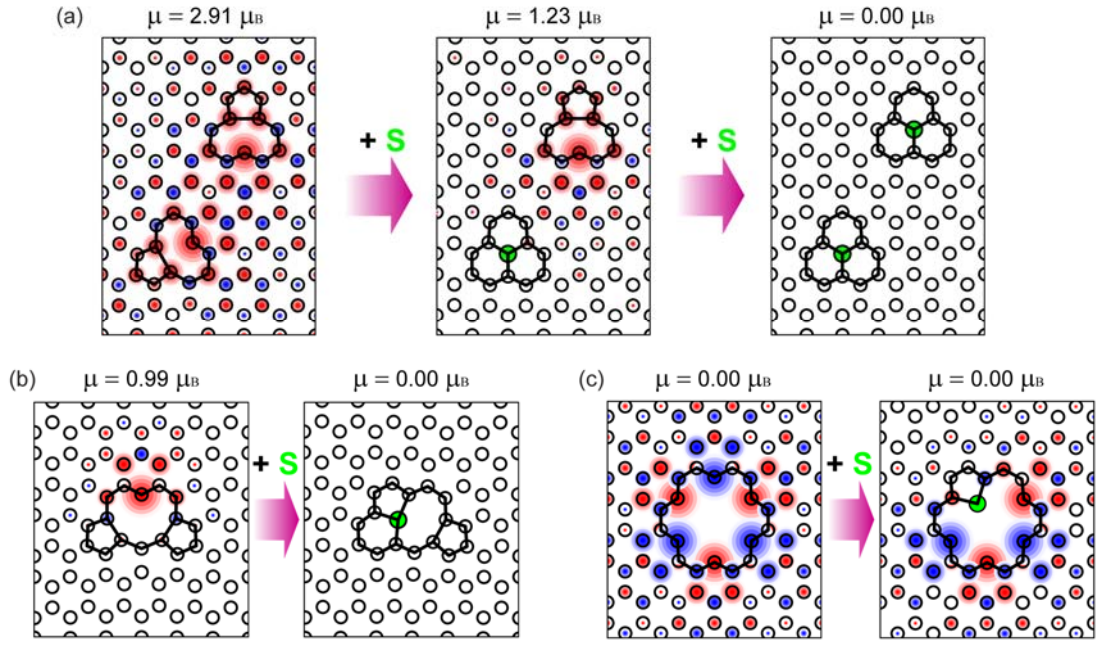

Figure 4.4.3: Demagnetization effect of sulfur in graphene with vacancies. In (a), two ferromagnetically interacting mono-vacancies are gradually demagnetized by successive additions of two sulfur atoms. Similarly, local magnetic moments of clusters of vacancies are quenched by attached sulfur atoms in (b) and (c).

Consistent with experimental results (cf. **Fig. 4.3.1**), we find that S-doping suppresses magnetic moments induced by dangling-bonds at vacancy sites in graphene lattice. As shown in **Fig. 4.4.3a**, the FM interaction between two mono-vacancies located within the interaction range (<10 nm [19, 20]), results in a net magnetic moment of 2.9 μ_B. Doping with a single sulfur atom that occupies one of the two available vacant substitutional sites leads to a loss of magnetic moment to 1.2 μ_B. Additional sulfur atom occupies the remaining vacant site and completely quenches the magnetism. Similar results

are observed for graphene with trivacancy, shown in Fig. 3.4.3b, where a substitutional sulfur atom leads to a complete loss of magnetic moment from 1.0 μ_B to zero. **Fig. 4.4.3c** shows a special case where the distribution of local magnetic moments is induced by six dangling-bond sites in the cluster of six vacancies. Up and down spin densities are symmetrically distributed in two sublattices of graphene in the vicinity of the cluster, but they balance out each other and yield no net magnetic moment. The attached sulfur atom negates nearby local moment, but the net magnetic moment of the system remains zero. In all cases we investigated, we found that the attached sulfur atom itself does not impart any magnetism to any non-magnetic structures in graphene.

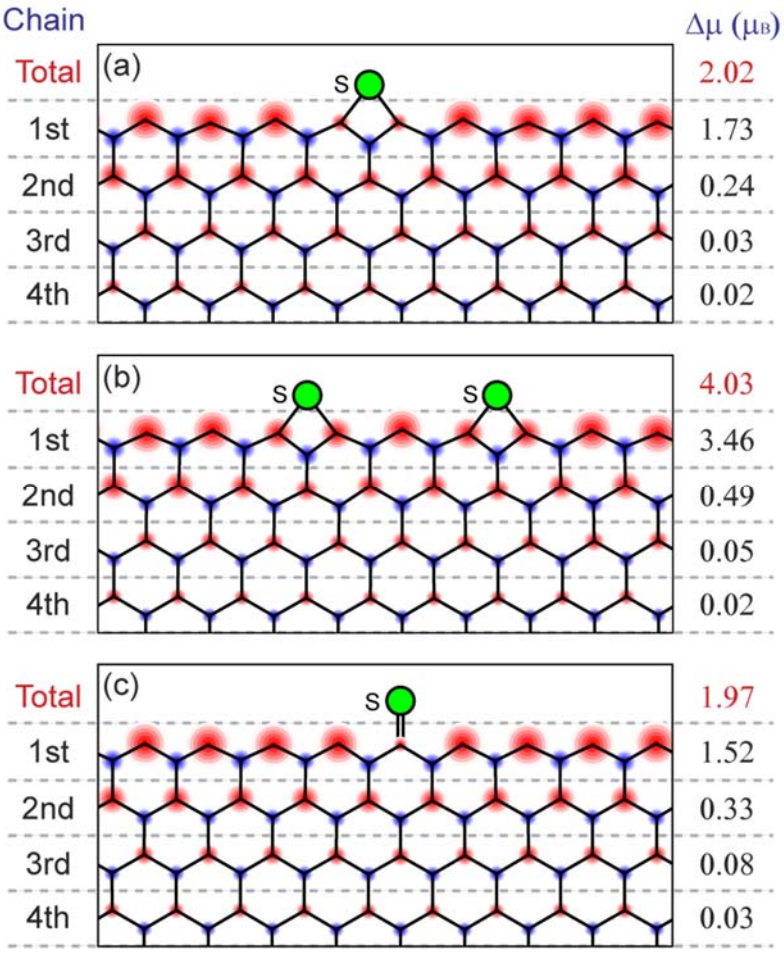

Figure 4.4.4: Demagnetization effect of sulfur in zigzag edges of graphene. Regardless of the type of bond, about 2 μ_B of reduction per sulfur atom in the total magnetic moment of the zigzag edge is observed.

The magnetic properties of the zigzag graphene edges are also affected by the addition of sulfur atoms. As shown in **Fig. 4.4.4**, S-dopants locally demagnetize graphene along zigzag edges with approximately ~2 μ_B reduction in magnetic moment per S-dopant

in the net magnetic moment. When a S-dopant is present, it quenches the local magnetic moment by bonding unpaired electrons of edge carbon atom. Nonetheless, the FM ordering of spin moments along zigzag chains remains persistent even after the addition of multiple S atoms.

4.5. Conclusions

In summary, our experiments showed that the magnetism in graphene is sensitive to the nature of the defects. While pristine graphene with naturally occurring edges and vacancies (i.e., intrinsic defects) exhibits a non-zero magnetic moment, the addition of S-dopants was found to quench this magnetic ordering. In fact, we found that sulfur doping drastically changes the magnetic behavior of the as-prepared samples. The zero-field-cooling (ZFC) and field-cooling (FC) in M vs. T measurements indicated the co-existence of large amount of super-paramagnetic domains along with antiferromagnetic domains in all the samples. From our DFT calculations, S dopants in GnPs were found to be attracted to defected sites such as vacancies, vacancy clusters, and edges. Indeed, S-dopants were observed to saturate dangling bonds and quench the local magnetic moment of defect structures and ultimately result in a diamagnetic response, weakly ferromagnetic, and antiferromagnetic ordering concurring with our experimental findings. When taken together, our experimentally observed demagnetization in S-doped GnPs and theoretical calculations confirm that the net magnetization in pristine graphene arises from the presence of entropically necessary defects and not just metal impurities.

CHAPTER 5

ROLE OF DEFECTS AND DOPANTS ON THE RAMAN SPECTROSCOPY OF GRAPHENE

5.1. Introduction

Graphene is the two-dimensional basis for many carbon allotropes including graphite, carbon nanotubes (CNTs), and fullerenes. Many unique applications of graphene are envisaged in energy, electronics, optics, and medicine based on the distinct electronic and optical properties of single-, bi-, and few-layer graphene (SLG, BLG, and FLG). While the intralayer C-C bonding within a graphene sheet (as in SLG) is considerably strong, the interlayer van der Waals interactions (as in BLG and FLG) are weak. Such an anisotropy in the graphene structure leads to unusual characteristics (e.g., massless vs. heavy fermions and an extremely wide energy range for phonons) in its electron and phonon structure.

Raman spectroscopy is one of the most powerful techniques to characterize carbon allotropes and prove their electronic and phononic properties.[130,131] In particular, the unique electronic structure of graphene leads to a resonant photo-excitation at any laser energy ensuing in the appearance of many (otherwise not prominent) features in the Raman spectrum due to the so-called double resonance (DR) mechanism.[52,132] In the DR mechanism, both the excited and scattered electrons are in simultaneous resonance with incoming photons and phonons respectively, facilitating the detection of phonons away from the Brillouin zone center of graphene.[52,130–135] While the Raman measurements

on graphene are simplistic in nature, the true complexity lies in the data interpretation. Indeed, the richness and the wealth of information that could be gleaned from the DR Raman spectra of carbon-based nanostructures (in terms of peak frequencies, widths, and phonon energy dispersions) have been intriguing spectroscopists for more than four decades.

Although most of the prominent Raman features such as the graphitic (*G*-band) and disorder (*D*-and *D'*-bands) related peaks, and their overtones (*G'* and 2*D'* bands) are well understood within the DR picture, a comprehensive understanding of the ubiquitous feature at 2450 cm^{-1} (also called the *G** band or *D*+*D*" band) still remains unclear.[8–13] Prior to the introduction of DR mechanism, to elucidate off-zone center phonons in the graphite Raman spectrum, Nemanich *et al.*[136] observed the *G** feature in graphite and attributed it to an unspecified overtone mode since it showed a polarization dependence similar to the *G'* and 2*D*' bands. However, Tan *et al*. [137] observed later that the *G** band frequency in graphite exhibited a distinct redshift with increasing excitation energy, unlike the blueshift in the *G'* and 2*D*' band frequencies. They assigned the *G** band to a combination of an in-plane transverse optical (*iTO*) and a longitudinal acoustic (*LA*) phonon. On the contrary, Shimada *et al.*[138] reported a dispersion-less peak at 2450 cm^{-1} in single- and double-walled CNTs, and attributed it to the overtone of longitudinal optical (*LO*) phonon near the *K*-point in the Brillouin zone. In the case of SLG, Mafra *et al*.[139] first assigned the *G** band to a combination of *LA* and *iTO* phonons. Recently, the *G** band in graphene was observed to possess an asymmetric tail towards higher frequencies that hinted at the presence of distinct sub-peaks (containing at least two peaks) due to multiple

phonon scattering processes. Araujo *et al.*[140] attributed the lower frequency sub-peak in the *G** band to a combination mode involving *iTO* and *LA* phonons (with a phonon wave vector $q \neq 0$), and the higher frequency peak to the combination of two dispersionless ($q = 0$) *iTO* phonons. However, May *et al*.[141] dismissed this explanation citing that the energy excitation window used by Araujo *et al.* was limited. Indeed, May *et al.* showed that both sub-peaks involved in *G** band strongly dispersed with laser excitation energy. Furthermore, they propounded theoretically that the 2*iTO* ($q = 0$) phonon couldn't be observed in the Raman spectrum due to the destructive interference in the Raman matrix element. As detailed in Ref. [141], the main contribution of the *G** band (i.e., the lower frequency sub-peak) was then assigned to the so-called inner processes, i.e., phonons from the *K*-Γ direction in the graphene Brillouin zone. Furthermore, based on theoretical analysis, the asymmetric line shape on the high frequency side of the *G** band was attributed to additional, weaker contributions from phonon wave vectors with angles deviating up to 60 degrees from the *K*-Γ line. Lastly, May *et al.* observed that this asymmetry becomes stronger with layer stacking. All of the disparate peak assignments described above show that a satisfactory experimental and theoretical explanation of the origin, asymmetry, and the effects of layer stacking on the *G** band still remain elusive.

To uncover the origin of the *G** band, we performed a comprehensive study of multiple graphene samples with varying layers and defect densities, prepared using different synthesis methods. In particular, we used mechanically exfoliated and chemical vapor deposited (CVD) SLG, BLG, and FLG and analyzed their Raman spectra with a broad range of excitation wavelengths ranging from 1.96 (633 nm) to 3.81 eV (325 nm).

Our results show that the *G** band is indeed asymmetric and is composed of two or more sub-peaks, depending on the number of graphene layers. This asymmetry clearly increases with interlayer stacking. Both sub-peaks exhibit higher sensitivity to defects and decrease in intensity with increasing presence of defects, similar to other combination modes.[52,142] Juxtaposing our results from graphene samples with different defects across multiple excitation energies, the *G** band can, for the first time, be fully understood in terms of two time-order processes within the inner phonon scattering process (along the *K*-Γ direction) between *K* and *K*' points of the graphene Brillouin zone : i) *LA* phonon scattering followed by scattering by an *iTO* phonon results in the lower frequency peak (hereafter called the *LA*-first process), and ii) *iTO* phonon scattering followed by scattering by an *LA* phonon leads to the higher frequency peak (hereafter referred to as the *iTO*-first process).

To uncover the origin of the *G** band, we performed a comprehensive study of multiple graphene samples with varying layers and defect densities, prepared using different synthesis methods. In particular, we used mechanically exfoliated and chemical vapor deposited (CVD) SLG, BLG, and FLG and analyzed their Raman spectra with a broad range of excitation wavelengths ranging from 1.96 (633 nm) to 3.81 eV (325 nm). Our results show that the *G** band is indeed asymmetric and is composed of two or more sub-peaks, depending on the number of graphene layers. This asymmetry clearly increases with interlayer stacking. Both sub-peaks exhibit higher sensitivity to defects and decrease in intensity with increasing presence of defects, similar to other combination modes.[52,142] Juxtaposing our results from graphene samples with different defects

across multiple excitation energies, the *G** band can, for the first time, be fully understood in terms of two time-order processes within the inner phonon scattering process (along the *K*-*Γ* direction) between *K* and *K*' points of the graphene Brillouin zone : i) *LA* phonon scattering followed by scattering by an *iTO* phonon results in the lower frequency peak (hereafter called the *LA*-first process), and ii) *iTO* phonon scattering followed by scattering by an *LA* phonon leads to the higher frequency peak (hereafter referred to as the *iTO*-first process).

5.2. Experiments and Characterization Methods

In our experiements, graphene samples having various layers were prepared using the standard mechanical exfoliation method from HOPG on 280 nm SiO_2/Si substrates. The mechanically exfoliated samples were previously studied in Ref. [52]. Additional graphene samples studied in Section 5.3 were obtained by standard chemical vapor deposition growth on Cu foils.[143] The presence of SLG, BLG and few layer graphene (FLG) areas were confirmed by atomic force microscopy (AFM) and micro-Raman spectroscopy (see **Fig. 5.2.1**).[52]

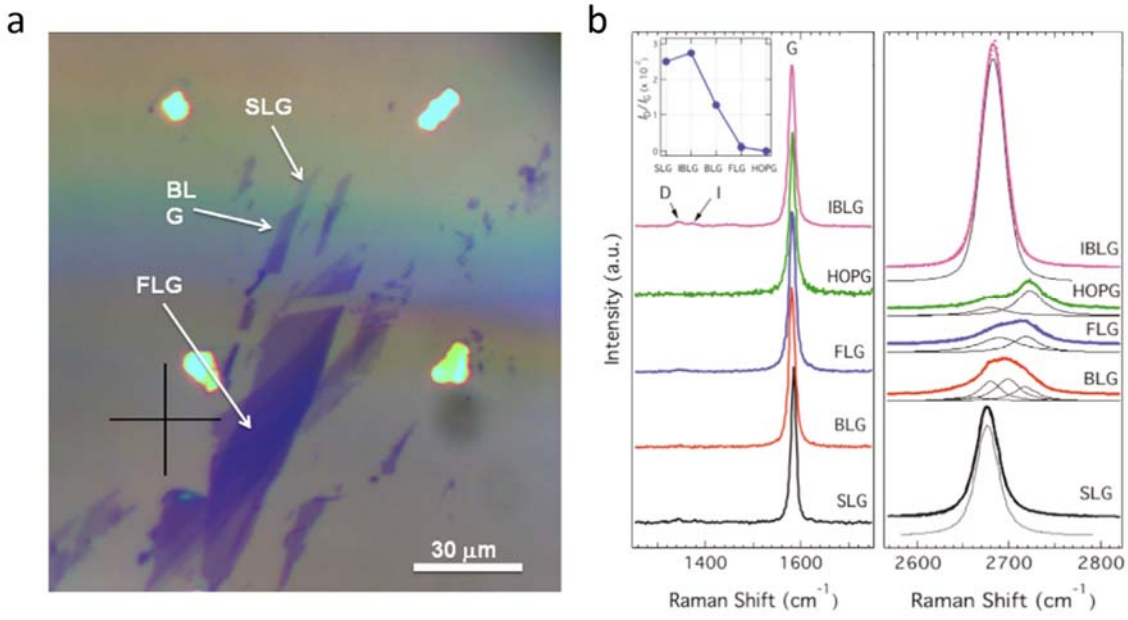

Figure 5.2.1: (a) Optical microscope (50 x magnification) image of the mechanically exfoliated graphene flakes (have parts with one, two and few layers) on 280 nm SiO2/Si substrate studied in this chapter. (b) Raman spectra of the mechanically exfoliated SLG, BLG, FLG used in this study in the *D*, *G* and *G*' band regions. (Both (a) and (b) are acquired from Ref. [52])

The Raman spectra were acquired with both a Renishaw InVia Raman microscope and a Dilor XY micro-Raman setup. The incident laser beam was focused by a 50x objective and the laser power on the samples was kept to a minimum to avoid heating. All the Raman spectra were normalized with respect to the *G* band intensity and were baseline corrected prior to Voigt lineshape analysis. Temperature dependent Raman spectra were

obtained from 25 to 250 °C by using a Linkam thermal stage (Linkam Scientific Instruments Ltd, UK).

5.3. *G**-band of graphene and the time-ordered scattering process

Figures. 5.3.1a-c show the Raman spectra of mechanically exfoliated SLG, BLG, and FLG samples in the 2200-2600 cm^{-1} region, collected with multiple excitation energies (E_l = 1.96-3.81 eV). The full Raman spectra, as well as the optical microscope image of the SLG, BLG and FLG samples were published previously in Ref. [52]. All spectra in **Fig. 5.3.1** are normalized to the intensity of their respective *G* bands, and the sub-peaks of *G** band fit with Voigt lineshapes. The following two salient features are evident in **Fig. 5.3.1**: i) the *G** band exhibits more than one sub-peak at all the excitation energies for all the samples, and ii) the *G** band frequency consistently redshifts with increasing laser energy across all samples (see also Fig. 2a). While the *G** band in SLG and BLG can be fit to two sub-peaks at all excitation energies, the *G** band in FLG can be best fit to three sub-peaks for most excitations, which is discussed further below.

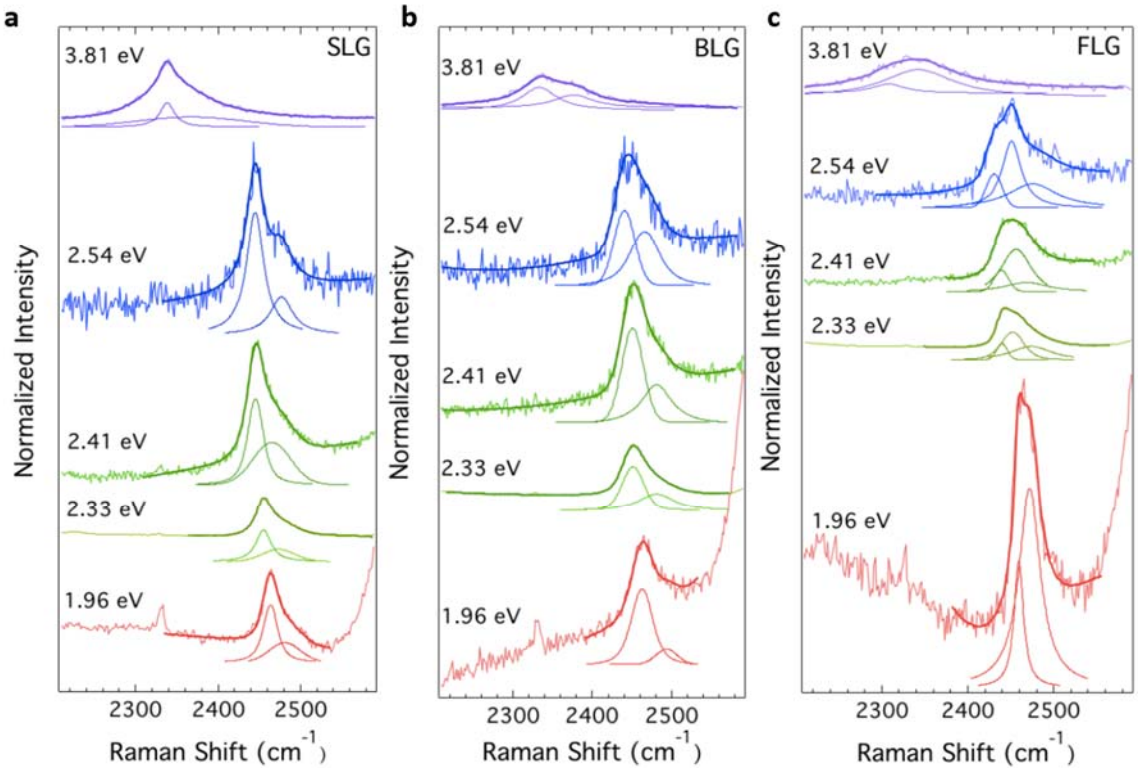

Figure 5.3.1: Raman spectra in the *G** band region for (a) SLG, (b) BLG, and (c) FLG, collected with laser excitations from 1.96 to 3.81 eV. All spectra have been normalized with respect to the *G* band intensities and the *G** band fitted with Voigt lineshapes.

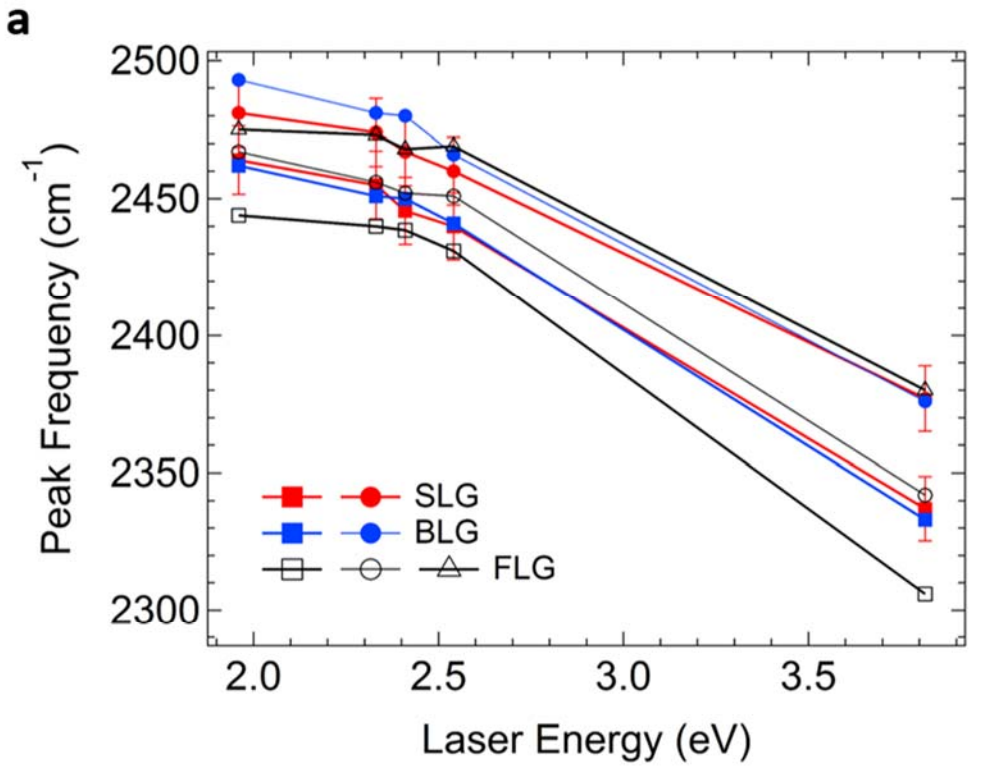
a
Peak Frequency (cm-1)
2500
2450
2400
2350
2300
SLG
BLG
FLG
2.0
2.5
3.0
3.5
Laser Energy (eV)

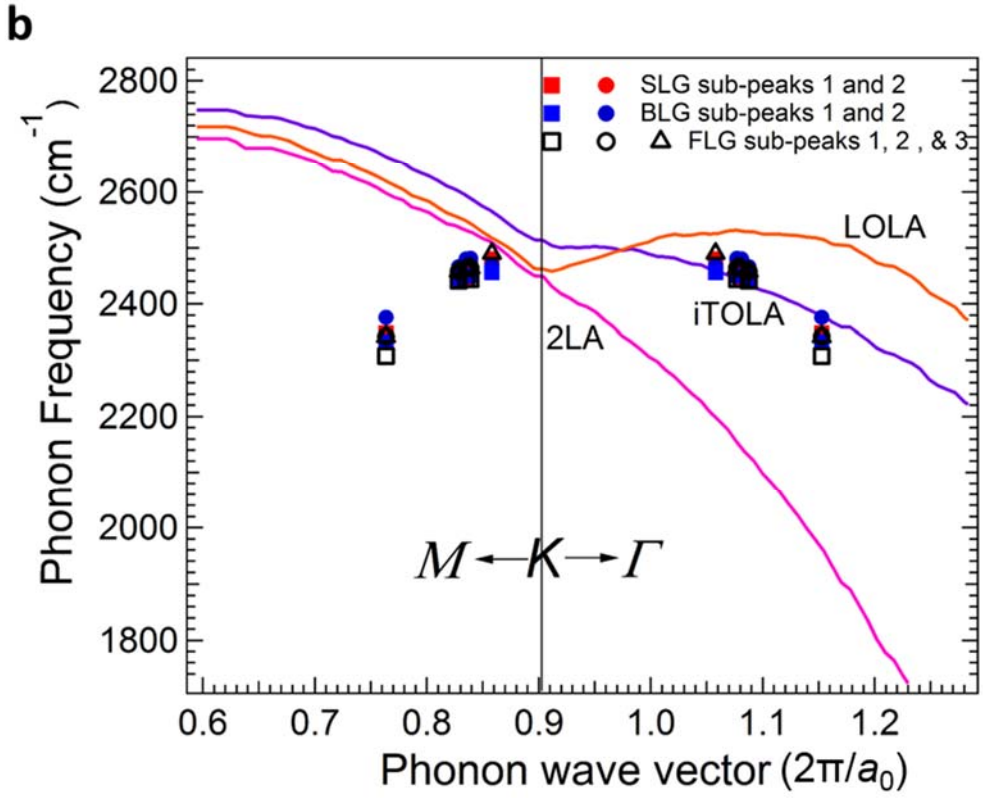
b
Phonon Frequency (cm-1)
2800
2600
2400
2200
2000
1800
SLG sub-peaks 1 and 2
BLG sub-peaks 1 and 2
FLG sub-peaks 1, 2 , & 3
LOLA
iTOLA
2LA
M ← K → Γ
0.6
0.7
0.8
0.9
1.0
1.1
1.2
Phonon wave vector (2π/a0)

Figure 5.3.2: (a) Plot of the dispersion of the *G** band peak frequencies against laser energies for SLG, BLG and FLG. The peak dispersions of all the sub-peaks are shown. (b) Frequencies of the *G** band sub-peaks plotted on the phonon dispersion of graphene in the frequency range from 1800-2800 cm^{-1}. The positions of all the *G** band sub-peaks suggest the origin of the *G** band is due to scattering from *iTO* and *LA* phonons (*iTOLA* branch) at *K*- *Γ* direction.

The frequency dispersions (against E_l) for all sub-peaks within the *G** band in mechanically exfoliated SLG, BLG and FLG are shown in **Fig. 5.3.2a**. All the sub-peaks within the *G** band exhibit similar slopes in their dispersion, in contrast to some of the previous studies, which reported a dispersionless (/weakly dispersing) higher frequency (/lower frequency) sub-peak for SLG and graphite.[138,140] Importantly, the dispersions shown in **Fig. 5.3.2a** are non-linear, compelling us to compare our data to the phonon dispersion of graphene. **Figure 5.3.2b** shows the experimental graphene phonon dispersion [48] centered around the *K* point in the frequency range from 1800 to 2800 cm^{-1}. Neglecting the 2*iTO* mode ($q \neq 0$), which is responsible for the *G'* band, there are only three other combination and overtone modes that could match the *G** band frequency, namely, 2*LA*, *iTO*+*LA* (or *iTOLA*) and *LO*+*LA* (*LOLA*). We plot the dispersions of the sub-peaks within the *G** band on top of the graphene phonon dispersion along both the *K*-*Γ* and *K*-*M* directions in **Fig. 5.3.2b**, which clearly shows that the observed non-linear dispersion of the *G** band corresponds to the *iTOLA* branch along the *K*-*Γ* direction of the graphene

Brillouin zone. Our assignment of the phonons involved in the *G** band is therefore partially consistent with previously reported results by May *et al*.[141]

As mentioned earlier, Araujo *et al.* previously assigned the higher frequency sub-peak to a double-resonant process involving two *iTO* phonons from the *K*-point.[140] However, May *et al.* pointed that such a contribution is cancelled in the full integration of the Raman cross-section due to destructive interference resulting from the intervalley electron scattering between two parallel electronic bands with the same slope and sign.[141] Juxtaposing the experimental Raman spectrum for SLG with theoretical calculations, May *et al.* suggested that the low frequency sub-peak of the *G** band originates from the so-called inner processes (i.e., phonons and electrons along *K*-*Γ* and *K*-*M* line, respectively) while the high frequency sub-peak is due to processes along other directions (e.g., outer process with phonons and electrons along *K*-*M* and *K*-*Γ* line, respectively; see **Fig. 5.3.3**).[141] In other words, according to May *et al.*, the energy dispersions (with respect to the laser excitation) for the lower frequency sub-peak match *iTOLA* along *K*-*Γ* direction while the higher frequency sub-peaks should match *iTOLA* along *K*-*M* direction. However, as shown in **Fig. 5.3.2b**, all the observed dispersions of the sub-peaks in our *G** band match very well with the *iTOLA* branch along the *K*-*Γ* direction, implying a different origin for the higher frequency sub-peak in the *G** band. Our observation is also consistentant with the theoretical conclusion by Mafra *et al.* that the electron-phonon scattering matrix elements of the *LA* phonons vanishes along the *K*-*M* direction. [139]

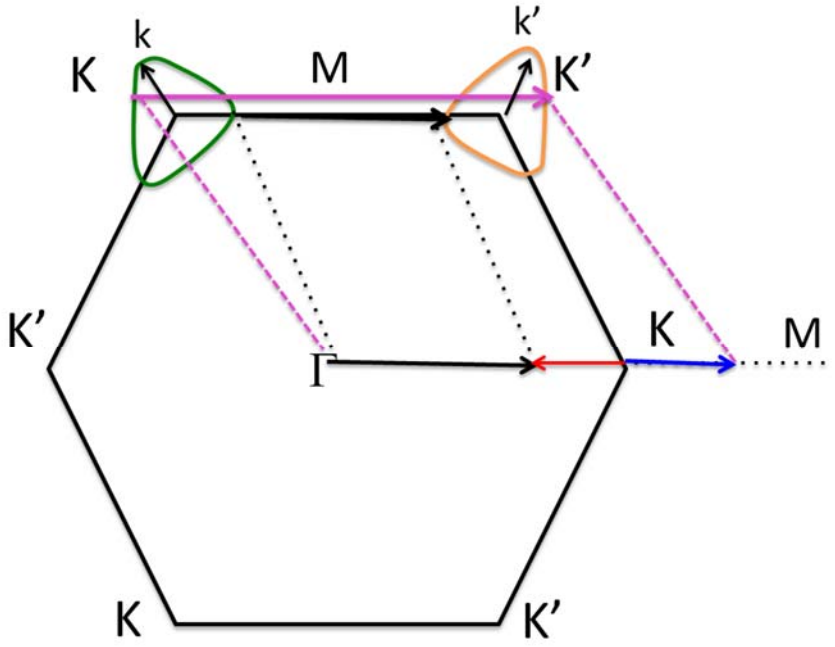

Figure 5.3.3: (a) Schematic of outer (pink arrow)/inner (black arrow) processes involving electrons on the *K*-*Γ*/*K*-*M* direction and phonons on the *K*-*M*/*K*-*Γ* (blue/red arrow, respectively) direction. The green (orange) cycles show the triangularly distorted contours mapped by the electronic momentum $\vec{\boldsymbol{k}}$ ($/\vec{\boldsymbol{k}}'$) vectors around the *K* (/*K*') point.

Here we propose that these sub-peaks arise from different time-order scattering processes of the *iTO* and *LA* phonons along the same *K*-*Γ* direction, which is rationalized further in the discussion below. As depicted in the schematic of inner DR processes[144] in **Figs. 5.3.4a and b**, the photo-excited electrons can be first scattered either by a *LA* or an *iTO* phonon (labeled *LA*-first in **Fig. 5.3.4a** and *iTO*-first in **Fig. 5.3.4b**). The

asymmetric feature of the *G** band can be understood in terms of the electronic and phonon trigonal warping and the electron-electron and electron-phonon scattering mechanisms. It is important to first note that the two-phonon DR mechanism consist of four processes: i) electronic excitation, ii) first-order phonon scattering, iii) second-order phonon scattering, and iv) recombination. The triangularly distorted contour (the distortion is a consequence of trigonal warping of electronic bands)[145] around the *K* point in **Fig. 5.3.3** is the iso-energy loop of the excited electrons involved in step (i) of the DR process. The electronic momentum ($\vec{k}$) vectors, which map the iso-energy contours (see the black arrow within the green colored iso-energy loop in **Fig. 5.3.3**), are determined by the excitation laser energy E_l. The phonon scattering of the excited electron around the *K* point results in another triangularly distorted iso-energy contour surrounding the *K*' point with the electronic momentum vectors ($\vec{k}'$shown as a black arrow within orange colored iso-energy loop, as in **Fig. 5.3.3**) now determined by energy E_l -E_{phonon}, where E_{phonon} is the energy of phonon involved in the scattering process (i.e., *LA* or *iTO*). For convenience and the ease of discussion, the scattered electronic momentum vectors are labeled as $\vec{k}_1'$ and $\vec{k}_2'$ for the *LA*-first (**Fig. 5.3.4a**) and *iTO*-first (**Fig. 5.3.4b**) processes.

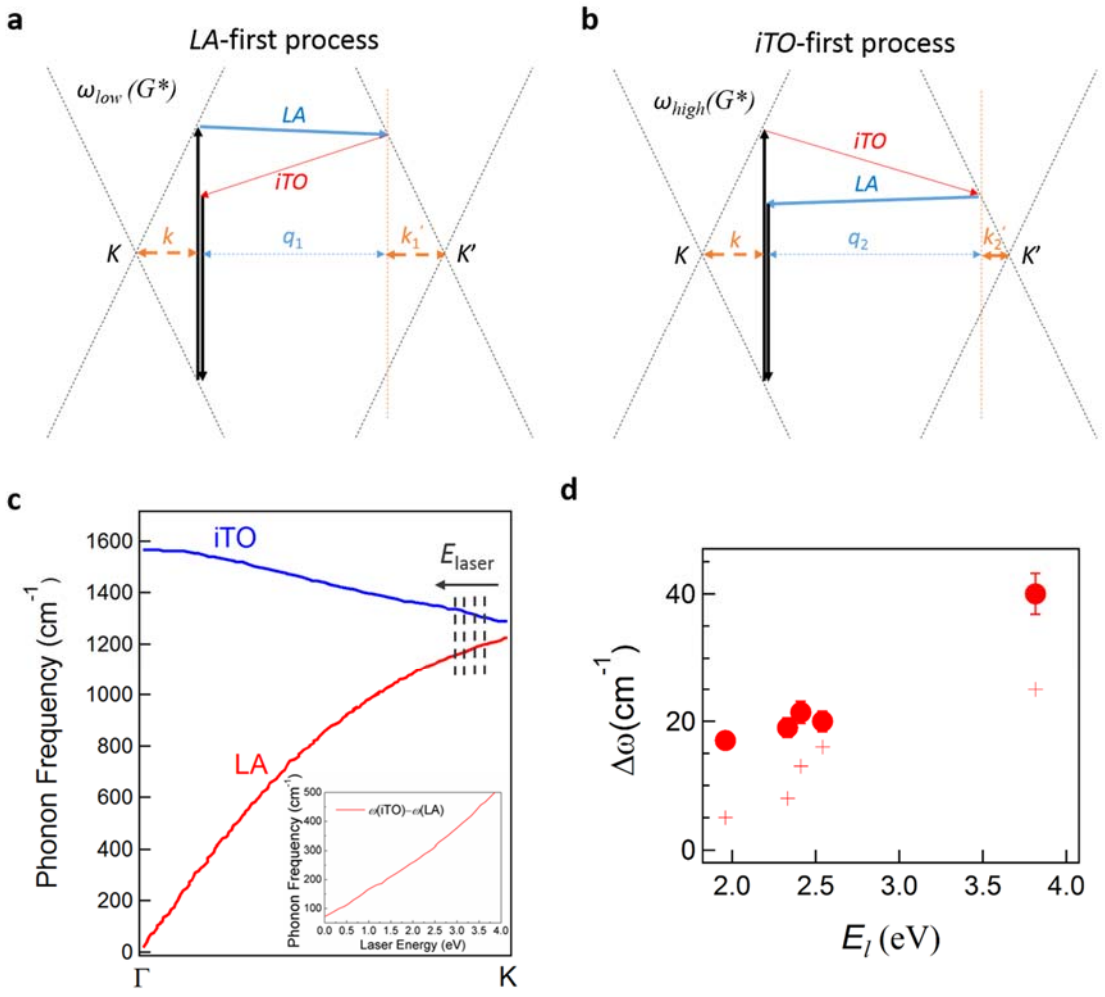

Figure 5.3.4: (a) and (b) The schematic of inner DR processes, labeled as *LA*-first in (a) and *iTO*-first in (b). (c) Dispersion of the *iTO* and *LA* phonons along the *K*-*Γ* direction. (Data obtained from Ref. [48]) The frequency of *LA* phonon is lower than that of *iTO* and the difference increases with increasing laser energy. Inset: frequency difference between the *iTO* and *LA* phonons along the *K*-*Γ* direction as a function of laser energy. (d) Frequency difference between the low- and high-frequency sub-peaks $\Delta\omega$ in the *G** band from SLG, plotted against excitation laser energy (red dots). The red crosses represents

theoretical calculated $\Delta\omega$ for each laser energy using Eq. 5.3 and graphene phonon dispersion relation from Ref. [48].

In **Fig. 5.3.4a**, the electron is first scattered (step (ii)) by an *LA* phonon resulting in an electronic momentum vector $\vec{k}_1' = (E_l - E_{LA})/\hbar$. This corresponds to a *LA* phonon wave vector:

$$\vec{q}_1 = \vec{K} - (\vec{k} + \vec{k}_1') \, . \tag{5.1}$$

Where $\vec{K}$ is the vector connecting *K* and *K*' points and $\vec{k}$ is the momentum for the excited electron. Similarly, the *iTO* phonon wave vector in **Fig. 5.3.4b** will be:

$$\vec{q}_2 = \vec{K} - (\vec{k} + \vec{k}_2') \, . \tag{5.2}$$

Thus, the scattering by the second phonon (step (iii)) by *iTO* (in **Fig. 5.3.4a**) and *LA* (in **Fig. 5.3.4b**) results in a Raman peak arising from phonons with the following wave vectors: *LA*($\vec{q}_1$)+*iTO*($\vec{q}_1$) or *iTOLA*($\vec{q}_1$) in *LA*-first process (**Fig. 5.3.4a**) and *iTO*($\vec{q}_2$)+*LA*($\vec{q}_2$) or *iTOLA*($\vec{q}_2$) in the *iTO*-first process (**Fig. 5.3.4b**). From **Figs. 5.3.4a** and **5.3.4b**, $|\vec{k}_1'| > |\vec{k}_2'|$ because the *LA* phonon frequency near the *K* point is always lower than that of the *iTO* phonon (**Fig. 5.3.4c**). Therefore, $|\vec{q}_2| > |\vec{q}_1|$ suggesting that the Raman peak for *iTO*-first process (i.e., *iTOLA*($\vec{q}_2$))) corresponds higher frequency than *LA*-first process (i.e., *iTOLA*($\vec{q}_1$)). Based on this, we assign the lower and higher frequency sub-peaks in the *G** band to time-ordered *LA*-first and *iTO*-first processes, respectively.

Below we provide three strong evidences that support time-ordered processes as the origin for the observed asymmetry in the G^* band. Firstly, we observe that the frequency difference ($\Delta\omega$) between the higher and lower frequency sub-peaks increases with E_l (**Fig. 5.3.4d**). Considering that the inner/outer processes cannot be used to rationalize the difference between lower and higher frequency sub-peaks (see discussion regarding **Fig. 5.3.2b**), the observed monotonic increase of $\Delta\omega$ as a function of E_l could be explained using the time-ordered approach. In this picture, $\Delta\omega = iTOLA(\vec{q}_2)$ - $iTOLA(\vec{q}_1)$ increases as a consequence of the increase in the difference between $|\vec{q}_2|$ and $|\vec{q}_1|$ (see **Figs. 5.3.4a** and **5.3.4b**) with E_l. By combining the Eqs. 5.1 and 5.2 derived above, it can be seen that

$$|\vec{q}_2| - |\vec{q}_1| = (E_{iTO} - E_{LA})/\hbar \, . \tag{5.3}$$

The difference between the energies of *iTO* and *LA* branches clearly diverges in the *K*-Γ direction, which is reflected in the E_l dependence of $\Delta\omega$. We used Eq. 5.3 and the phonon dispersion relation to calculated theoretical values of $\Delta\omega$ at each laser energy, and see a similar increasing trend as our experimental data (**Fig. 5.3.4d**).

5.4. Dependence of G*-bands on defects and temperature

A second evidence for the above discussed time-ordered processes involves defects. Since our time-ordered approach involves the *iTO* phonon (through the *iTOLA* mode), it should therefore be possible to differentiate between *LA*-first and *iTO*-first

processes by examining the influence of defects on the lineshape of the *G** band. The Raman scattering cross-section (*Q*) for a two-phonon process may be expressed as follows:

$$Q = \sum_{a,b,c} \frac{M_{fc} M_{cb} M_{ba} M_{ai}}{(E_l - E_{ai} - i\hbar\lambda)(E_l - \hbar\omega - E_{bi} - i\hbar\gamma)(E_l - \hbar\omega - E_{ci} - i\hbar\gamma)} . \quad (5.4)$$

In Eq. 5.4, M_{xy} (*x, y= a, b, and c*) is the matrix element for scattering over the intermediate states *x* and *y*, E_l and $E_l - \hbar\omega$ are the energies of the incoming and outgoing photon, E_{pi} (*p=a, b,* and *c*) is difference in the energy of electronic level *p* and the initial level *i*, and γ is the broadening parameter of the electronic transition between *p* and *i*. All the Raman scattering processes are inhomogeneously broadened by the parameter γ, which is inversely proportional to the electron-phonon (denoted by a characteristic timescale $t_{\text{el-ph}}$) and electron–electron scattering ($t_{\text{el-el}}$) time of the photo-excited carriers. The electron-electron scattering rate ($1/t_{\text{el-el}}$) for relaxing the hot carriers is proportional to $(E_l - E_F)^2$ while $1/t_{\text{el-ph}}$ varies as $(E_l - E_F)$, where E_F is the Fermi energy. From the standpoint of equation 4, the presence of a defect in the graphene lattice is expected to result in two important changes: i) an increase in the parameter γ through the introduction of new electron-defect scattering mechanisms, leading to the broadening of the sub-peaks in the *G** band, and ii) a decrease in the probability of two-phonon scattering processes due to the emergence of electron-defect scattering. An increase in the probability of an electron being scattered from one energy state to another by a defect (for example the *D* band process) rather than a phonon decreases the probability of electron being scattered by phonons alone (second order combination modes) at any fixed excitation energy and incident intensity. The

implications of the above points should be manifested in significant changes in the intensities of the *G** band sub-peaks in SLG with varying defect densities.

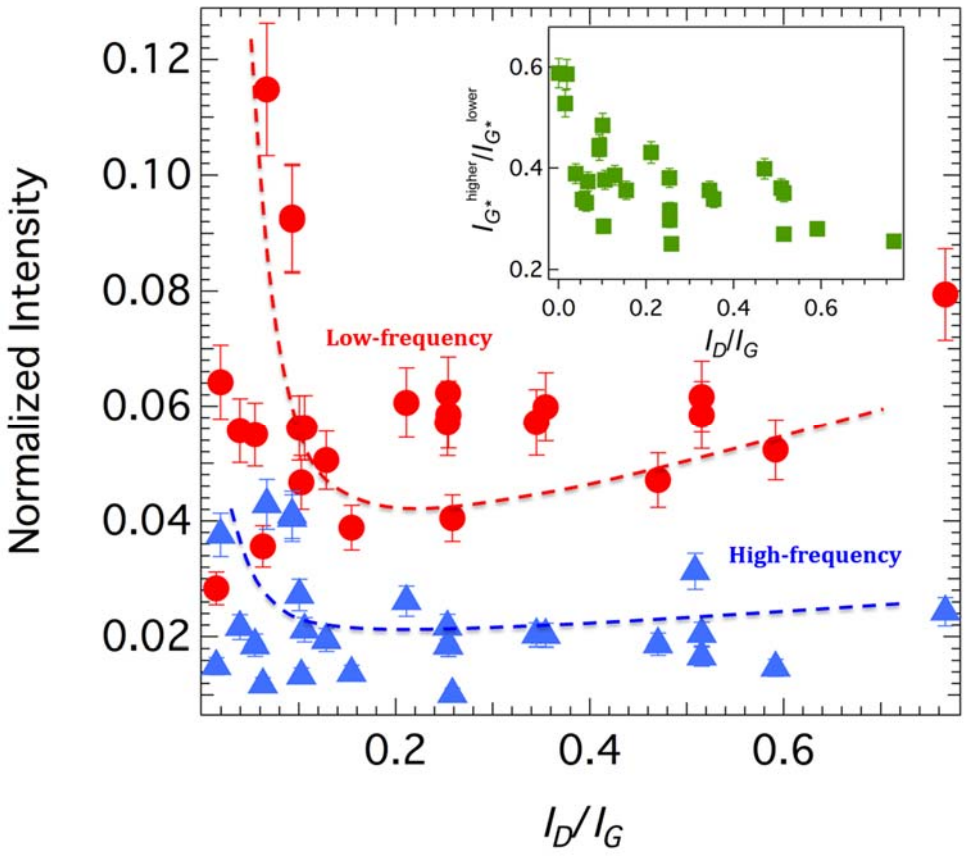

Figure 5.4.1: Plot of the intensity (normalized to the *G* band intensity) of the high-frequency sub-peak and the low-frequency sub peak in the *G** band against I_D/I_G ratios for several CVD-grown and mechanically exfoliated SLG samples. The dotted line is a general guide to the eye. The inset shows that the intensity ratio of the high-frequency to low-frequency sub-peaks decreases with increasing defects due to the presence of additional defect-scattering mechanisms.

Figure 5.4.1 illustrates the changes in the *G** band sub-peak intensities with varying defect density in SLG. We plot the intensities of the two sub-peaks within the *G** band against the I_D/I_G ratios from several CVD-grown and mechanically exfoliated SLG samples. Note that the defects in these graphene samples were not created intentionally. They occurred naturally during the exfoliation or CVD growth process. It can be seen clearly from Fig. 4 that the intensity of both sub-peaks decreases markedly with increasing defect density for SLG, as expected. This obvious decrease in intensity of the *G** band clearly validates our assertion that the addition of defects to the graphene lattice lowers the probability of the *iTO* scattering process owing to an increase in the probability of scattering by the defect. We also see that the higher frequency sub-peak (*iTO*-first process) exhibits a steeper drop in intensity with increasing I_D/I_G compared to the lower frequency peak. This is shown in the inset in Fig. 4d, where the ratio of intensities between the higher frequency to lower frequency sub-peaks clearly decreases with increasing defects. The photo-excited carriers that are initially scattered by *iTO (/LA)* can achieve larger momentum changes (and hence rapidly cool down) by scattering with defects (e.g., *iTO*+defect or defect+*iTO*, responsible for the *D* band) rather than with *LA* (/*iTO*) phonons (*iTO*+*LA*).

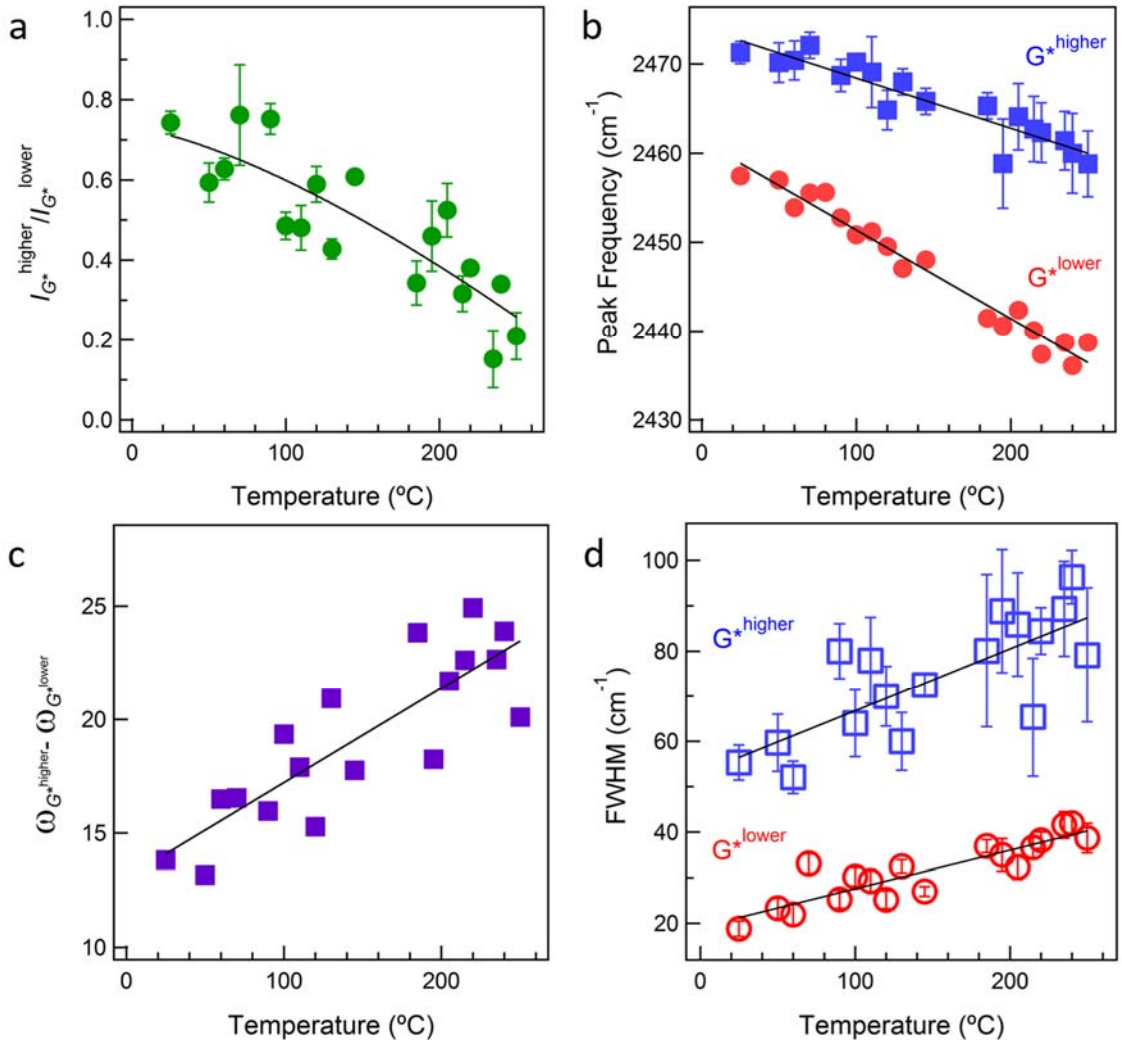

Figure 5.4.2: (a) The intensity ratio of the high-frequency to low-frequency sub-peaks decreases with increasing temperature. (b) Plots of the dispersion of the *G** band sub-peak frequencies against temperature for mechanically exfoliated SLG. (c) The temperature dependence of frequency difference between the high-frequency and low-frequency *G** band sub-peaks. (d) The temperature dependence of the FWHM of *G** band sub-peaks.

In order to further explore the origin of *G** band, we collected Raman spectra of mechanically exfoliated SLG for temperatures ranging from 25 to 250 ^{o}C (**Fig. 5.4.2**). The ratio of high and lower frequency sub-peak intensities was found to decrease with increasing temperature. From the phonon-dispersion relations of graphene, the frequency (and hence the energy) of *LA* phonons is always lower than *iTO* phonons. Thus, the average number of *LA* phonons at higher temperatures is greater than *iTO* phonons. This difference in *LA* and *iTO* phonon populations, at higher temperatures, is expected to increase the probability of the *LA*-first resonance process. The observed decrease in the intensity ratio of the higher frequency (*iTO*-first) to the lower frequency (*LA*-first) sub-peaks (**Fig. 5.4.2a**) supports such an assertion.

The temperature dependence of Raman-active modes could be described using

$$\omega_i(T) = \omega_{0i} + \Delta_i(T)\ , \tag{5.5}$$

where ω_{0i} is the harmonic frequency of the Raman-active modes [146]. $\Delta(T)$ is the temperature dependent perturbation of the real of the phonon self-energy. $\Delta(T)$ could be expressed as

$$\Delta_i(T) = \Delta_i^1(T) + \Delta_i^2(T), \tag{5.6}$$

where $\Delta_i^1(T)$ describes the contribution of thermal-expansion and $\Delta_i^2(T)$ arises from phonon-phonon coupling. The first term in Eq. 5.6 depends mainly on material properties such as the Gruneisen parameter and coefficient of thermal expansion rather than the type and nature of phonon and phonon-phonon interactions. On the other hand, $\Delta_i^2(T)$ arises from higher-order anharmonic terms in the Hamilotonian and includes the coupling between phonons.

We found that both sub-peaks exhibit red-shift with increasing temperature, as shown in **Fig. 5.4.2b**. The lower frequency peak appears to exhibit a higher slope (~ -0.09 cm^{-1}/K) than that of the higher frequency sub-peak (~ -0.056 cm^{-1}/K). Interestingly, these slopes are much higher than those for the *G* (~-0.015-0.03 cm^{-1}/K) reported in the literature [147] but are on the same scale as other two-phonon modes such as *G*' (-0.08-0.09 cm^{-1}/K) and 2*D*' bands (-0.09 cm^{-1}/K) concurring with the fact that *G** is a two-phonon process. In other words, the anharmonic term $\Delta_i^2(T)$ involving phonon-phonon interactions contributes significantly to the thermal shifts observed in the *G** band. We found that the difference between higher and lower peaks increased with increasing temperature, which may be as explained below. From Eqs. 5.5 and 5.6, this difference may be written as

$$\omega_{higher}(T) - \omega_{lower}(T) = d\omega_{0i} + \left(\Delta^2_{higher}(T) - \Delta^2_{lower}(T)\right), \tag{5.7}$$

where $d\omega_{0i}$ is a term representing the energy difference between the lower and higher peaks along with the thermal expansion effects (i.e., $\Delta_i^1(T)$ terms). For an optical phonon of energy E_{ph}, the anharmonic term involving phonon-phonon coupling is,

$$\Delta_i^2(T) = A + \frac{B}{e^{x_1} - 1} + \frac{C}{e^{x_2} - 1}, \tag{5.8}$$

where $x_1 + x_2 = E_{ph}/k_B T$ and *A*, *B*, and *C* are the anharmonic coupling constants. The exponential terms in Eq. 5.8 couples one optical phonon of energy E_{ph} to decay into two daughter acoustic phonons of energy E_1 and E_2 (Klemens process). For higher temperature processes ($E_{ph} < k_B T$), the anharmonic term may be estimated as

$$\Delta_i^2(T) = A + \frac{B}{x_1} + \frac{C}{x_2} = A + \left(\frac{BE_2 + CE_1}{E_1 E_2}\right) k_B T. \tag{5.9}$$

Based on Eqs. 5.6 and 5.9,

$$\omega_{higher}(T) - \omega_{lower}(T) = d\omega_{0i} + \left(\frac{B_h E_{2h} + C_h E_{1h} - B_l E_{2l} - C_l E_{1l}}{E_1 E_2} \right) k_B T \ , \qquad (5.10)$$

where the subscript *h* and *l* correspond to higher and lower frequency sub-peaks.

The energies of *iTO* phonon in the higher and lower frequency sub-peaks are different due to the time-order process. Thus, the daughter phonons arising from the decay of *iTO* phonon would have different energies for higher and lower frequency sub-peaks leading to a linear temperature dependent term in Eq. 5.10. **Fig. 5.4.2c** shows the experimental results of $\omega_{higher} - \omega_{lower}$ with respect to temperature, the plots can be fitted linearly, which matches with our prediction in Eq. 5.10. A complete picture of the difference in anharmonic terms for higher and lower peaks warrants detailed theoretical work. Nevertheless, the simple picture described above reveals the origin of temperature dependence and indirectly validates the time-order processes. Lastly, the width of higher and lower frequency sub-peaks also varied differently (**Fig. 5.4.2d**), which could also be attributed to the difference in $\Delta_i^2(T)$ terms for higher and lower frequency sub-peaks.

Following the above discussion, the time-ordered picture can also be extended to explain the richness of the *G** band in BLG and FLG samples. For instance, the three sub-peaks which were observed in FLG (see **Fig. 5.3.1c**) may be understood in terms of time-ordered scattering processes between different sub-bands. However, it may not be possible to readily deconvolute the individual processes due to a large number of possibilities for interband scattering (similar to the case of *G*' band)[134] and the limited resolution of the Raman spectrometer.

5.5. Conclusions

In conclusion, by systematically studying several SLG and FLG samples with varying defect densities across a wide range of laser energies, we have achieved a comprehensive understanding of the asymmetric *G** band at ~2450 cm^{-1} in the Raman spectrum of graphene. This band arises from a combination of *iTO* and *LA* phonons around the *K* point and along the *K*-Γ direction of the graphene Brillouin zone. In SLG, the *G** band can be deconvoluted into two peaks with the lower frequency (/higher frequency) peak occurring from *LA (/iTO)*-first DR process. The asymmetry of the *G** band is strongly influenced by layer stacking, and at least three sub-peaks are necessary to explain the structure of the *G** band in FLG. The time-ordered scattering processes have been supported by three strong experiment observations: *i*) The sub-peaks diverges with increasing laser energy. *ii*) The increase in defect density in graphene was found to result in the disappearance of the higher frequency components of the *G** band. *iii*) The intensity ratio of the higher frequency to the lower frequency sub-peaks decreases with temperature.

CHAPTER 6

SUMMARY AND FUTURE WORK

Defects are often perceived as performance limiters. Contrary to this notion, this thesis demonstrates that defects in graphene, a one atom thick allotrope of carbon, can be used to elicit enhanced material‘s performance, beyond predicted limits. Defects are inevitable and entropically present which stabilize nanomaterials such as graphene. My research found that the *defect configuration* and its local environment, rather than amount of defects present in graphene, are critical for: i) overcoming fundamental limitations posed by the so-called quantum capacitance and opening new channels for ion diffusion, ii) inducing ferromagnetism in graphene to enable future spintronic devices, and iii) gaining insights into fundamental time-ordered carrier scattering processes. In addition to these fundamental discoveries at the nanoscale, my work also led to the realization of flexible pouch supercapacitors based on defect-engineered graphene with energy densities of 500% higher than the state-of-the-art.

In Chapter 3, we demonstrated the use of defects to improve accessibilty of the interlayer spaces present in graphene, which alleviated the quantum capacitance bottleneck and led to a new paradigm in energy storage. The specific capacitance of graphene supercapacitor electrodes proved more sensitive to the defect configuration rather than defect concentration, where defect was either in the form of pores or the nitrogen dopants. It will be interesting to explore the effects of other dopants (e.g., B, S, O) and the presence

of functional groups (e.g., SiOC) in graphene on its energy storage capacity in Li-ion batteries, Li-air batteries, etc.

In Chapter 4, we elucidated that defects and S-dopants in graphene are responsible for the observed magnetization in graphene, which decreased upon sulfur doping suggesting that S-dopants demagnetized vacancies and edges. Also, our density functional theory calculations provided evidence for a net magnetization in graphene arising from its zig-zag edges, suggesting that the contradictory conclusions on graphene magnetism reported in the literature may stem from the magnetic properties due to different defect-types. Interestingly, we observed peculiar local maxima in the temperature dependent magnetizations that suggest the coexistence of different magnetic phases within the same graphene samples. A deeper study is needed in the future to unravel the role of dopant configuration on the magnetism, or superconductivity, in carbon nanomaterials.

In Chapter 5, we used a time-ordered scattering model to explain the origin of *G**-band ~ 2450 cm^{-1} in the Raman spectrum of graphene. The intensity of the *G**-band has shown to be sensitive to the concentration of defects. In addition to the *G**-band, there are also other combination Raman modes of graphene. It will be of great interest to understand the dependence of these combination modes on the defects concentration, configuration, and the edge states.

APPENDIX

Glossary of acronyms used in this dissertation

1. 2D: Two-dimensional
2. CNT: Carbon nanotube
3. SLG: Single-layer graphene
4. BLG: Bi-layer graphene
5. FLG: Few layered graphene
6. BZ: Brillouin zone
7. CVD: Chemical vapor deposition
8. EDLC: Electrical double layer capacitor
9. DOS: Density of states
10. QC: Quantum capacitance
11. CV: Cyclic voltammetry
12. HOMO: Highest occupied molecular orbitals
13. LUMO: Lowest unoccupied molecular orbitals
14. ESR: Equivalent series resistance
15. EIS: Electrochemical impedance spectroscopy
16. LA: Longitudinal acoustic
17. iTA: In-plane transverse acoustic
18. oTA: Out-of-plane transverse acoustic
19. LO: Longitudinal optic
20. iTO: In-plane transverse optic
21. oTO: Out-of-plane transverse optic
22. DR: Double-resonance
23. SC: Supercapacitor
24. DFT: Density function theory
25. GF: Graphene foam

26. XPS: X-ray photoelectron spectroscopy
27. SEM: Scanning electron microscopy
28. TEM: Tunneling electron microscopy
29. $TEABF_4$: Tetraethylammonium tetrafluoroborate
30. $TBAPF_6$: Tetrabutylammonium hexafluorophosphate
31. ACN: Acetonitrile
32. TEA^+: Tetraethylammonium
33. TBA^+: Tetrabutylammonium
34. PGF: Plasma etched graphene foam
35. NGF: N-doped graphene foam
36. FM: Ferromagnetic
37. GnP: Graphene nanoplatelets
38. NMP: N-Methylpyrrolidone
39. VSM: Vibrating sample magnetometer
40. SQUID: Superconducting quantum interference device
41. ZFC: Zero-field-cooled
42. FC: Field-cooled
43. ICP-MS: Inductively coupled plasma mass spectrometry
44. AFM: Atomic force microscopy

REFERENCES

[1] D. R. Cooper, B. D'Anjou, N. Ghattamaneni, B. Harack, M. Hilke, A. Horth, N. Majlis, M. Massicotte, L. Vandsburger, et al., "Experimental Review of Graphene," *ISRN Condens. Matter Phys.* **2012**, 1–56 (2012).

[2] H. X. Wang, Q. Wang, K. G. Zhou, and H. L. Zhang, "Graphene in light: Design, synthesis and applications of photo-active graphene and graphene-like materials," *Small* **9**, 1266–1283 (2013).

[3] F. Banhart, J. Kotakoski, and A. V. Krasheninnikov, "Structural defects in graphene," *ACS Nano* **5**, 26–41 (2011).

[4] A. Hashimoto, K. Suenaga, A. Gloter, K. Urita, and S. Iijima, "Direct evidence for atomic defects in graphene layers," *Nature* **430**, 870–873 (Nature Publishing Group, 2004).

[5] L. Tapasztó, G. Dobrik, P. Nemes-Incze, G. Vertesy, P. Lambin, and L. P. Biró, "Tuning the electronic structure of graphene by ion irradiation," *Phys. Rev. B* **78**, 233407 (American Physical Society, 2008).

[6] B. Anand, M. Karakaya, G. Prakash, S. S. Sankara Sai, R. Philip, P. Ayala, A. Srivastava, A. K. Sood, A. M. Rao, et al., "Dopant-configuration controlled carrier scattering in graphene," *RSC Adv.* **5**, 59556–59563 (The Royal Society of Chemistry, 2015).

[7] N. Ketabi, T. de Boer, M. Karakaya, J. Zhu, R. Podila, A. M. Rao, E. Z. Kurmaev, and A. Moewes, "Tuning the electronic structure of graphene through nitrogen doping: experiment and theory," *RSC Adv.* **6**, 56721–56727 (Royal Society of Chemistry, 2016).

[8] J. Tuček, P. Błoński, Z. Sofer, P. Šimek, M. Petr, M. Pumera, M. Otyepka, and R. Zbořil, "Sulfur Doping Induces Strong Ferromagnetic Ordering in Graphene: Effect of Concentration and Substitution Mechanism," *Adv. Mater.* **28**, 5045–5053 (2016).

[9] R. R. Nair, M. Sepioni, I.-L. Tsai, O. Lehtinen, J. Keinonen, A. V. Krasheninnikov, T. Thomson, A. K. Geim, and I. V. Grigorieva, "Spin-half paramagnetism in graphene induced by point defects," *Nat. Phys.* **8**, 199–202 (Nature Publishing Group, 2012).

[10] R. Podila, J. Chacón-Torres, J. T. Spear, T. Pichler, P. Ayala, and a. M. Rao, "Spectroscopic investigation of nitrogen doped graphene," *Appl. Phys. Lett.* **101**, 123108 (2012).

[11] H. Wang, T. Maiyalagan, and X. Wang, "Review on Recent Progress in Nitrogen-Doped Graphene: Synthesis, Characterization, and Its Potential Applications," *ACS Catal.* **2**, 781–794 (American Chemical Society, 2012).

[12] Y. Hernandez, V. Nicolosi, M. Lotya, F. M. Blighe, Z. Sun, S. De, I. T. McGovern,

B. Holland, M. Byrne, et al., “High-yield production of graphene by liquid-phase exfoliation of graphite,” *Nat. Nanotechnol.* **3**, 563–568 (Nature Publishing Group, 2008).

[13] K. S. Subrahmanyam, L. S. Panchakarla, A. Govindaraj, and C. N. R. Rao, “Simple Method of Preparing Graphene Flakes by an Arc-Discharge Method,” *J. Phys. Chem. C* **113**, 4257–4259 (American Chemical Society, 2009).

[14] S. Stankovich, D. A. Dikin, R. D. Piner, K. A. Kohlhaas, A. Kleinhammes, Y. Jia, Y. Wu, S. T. Nguyen, and R. S. Ruoff, “Synthesis of graphene-based nanosheets via chemical reduction of exfoliated graphite oxide,” *Carbon N. Y.* **45**, 1558–1565 (2007).

[15] K. S. Kim, Y. Zhao, H. Jang, S. Y. Lee, J. M. Kim, K. S. Kim, J.-H. Ahn, P. Kim, J.-Y. Choi, et al., “Large-scale pattern growth of graphene films for stretchable transparent electrodes,” *Nature* **457**, 706–710 (Nature Publishing Group, 2009).

[16] P. W. Sutter, J.-I. Flege, and E. A. Sutter, “Epitaxial graphene on ruthenium,” *Nat. Mater.* **7**, 406–411 (Nature Publishing Group, 2008).

[17] X. Li, W. Cai, J. An, S. Kim, J. Nah, D. Yang, R. Piner, A. Velamakanni, I. Jung, et al., “Large-area synthesis of high-quality and uniform graphene films on copper foils.,” *Science* **324**, 1312–1314 (American Association for the Advancement of Science, 2009).

[18] L. Baraton, Z. B. He, C. S. Lee, C. S. Cojocaru, M. Châtelet, J.-L. Maurice, Y. H. Lee, and D. Pribat, “On the mechanisms of precipitation of graphene on nickel thin films,” *EPL (Europhysics Lett.* **96**, 46003 (2011).

[19] G. A. López and E. J. Mittemeijer, “The solubility of C in solid Cu,” *Scr. Mater.* **51**, 1–5 (2004).

[20] M. Winter and R. J. Brodd, “What are batteries, fuel cells, and supercapacitors?,” *Chem. Rev.* **104**, 4245–4269 (2004).

[21] K. Kierzek, E. Frackowiak, G. Lota, G. Gryglewicz, and J. Machnikowski, “Electrochemical capacitors based on highly porous carbons prepared by KOH activation,” *Electrochim. Acta* **49**, 515–523 (2004).

[22] E. Raymundo-Piñero, K. Kierzek, J. Machnikowski, and F. Béguin, “Relationship between the nanoporous texture of activated carbons and their capacitance properties in different electrolytes,” *Carbon N. Y.* **44**, 2498–2507 (2006).

[23] E. Raymundo-Piñero, F. Leroux, and F. Béguin, “A High-Performance Carbon for Supercapacitors Obtained by Carbonization of a Seaweed Biopolymer,” *Adv. Mater.* **18**, 1877–1882 (2006).

[24] L. L. Zhang, R. Zhou, and X. S. Zhao, “Graphene-based materials as supercapacitor electrodes,” *J. Mater. Chem.* **20**, 5983 (The Royal Society of Chemistry, 2010).

[25] E. Frackowiak and F. Béguin, “Carbon materials for the electrochemical storage of

energy in capacitors," *Carbon N. Y.* **39**, 937–950 (2001).

[26] A. K. Geim and K. S. Novoselov, "The rise of graphene.," *Nat. Mater.* **6**, 183–191 (2007).

[27] S. Luryi, "Quantum capacitance devices," *Appl. Phys. Lett.* **52**, 501 (AIP Publishing, 1988).

[28] A. J. Bard and L. R. Faulkner, *Electrochemical methods : fundamentals and applications*, 2nd ed. (Wiley, 2001).

[29] G. A. Mabbott, "An introduction to cyclic voltammetry," *J. Chem. Educ.* **60**, 697–702 (1983).

[30] R. K. Emmett, M. Karakaya, R. Podila, M. R. Arcila-Velez, J. Zhu, A. M. Rao, and M. E. Roberts, "Can Faradaic processes in residual iron catalyst help overcome intrinsic EDLC limits of carbon nanotubes?," *J. Phys. Chem. C* **118**, 26498–26503 (2014).

[31] Y. Yang, B. Wang, J. Zhu, J. Zhou, Z. Xu, L. Fan, J. Zhu, R. Podila, A. M. Rao, et al., "Bacteria Absorption-Based $Mn_2P_2O_7$–Carbon@Reduced Graphene Oxides for High-Performance Lithium-Ion Battery Anodes," *ACS Nano*, acsnano.6b02036 (2016).

[32] S. S. K. Mallineni, J. Shannahan, A. J. Raghavendra, A. M. Rao, J. M. Brown, and R. Podila, "Biomolecular Interactions and Biological Responses of Emerging Two-Dimensional Materials and Aromatic Amino Acid Complexes," *ACS Appl. Mater. Interfaces* **8**, 16604–16611 (2016).

[33] B. Sengupta, W. E. Gregory, J. Zhu, S. Dasetty, M. Karakaya, J. M. Brown, A. M. Rao, J. K. Barrows, S. Sarupria, et al., "Influence of carbon nanomaterial defects on the formation of protein corona," *Rsc Adv.* **5**, 82395–82402 (Royal Society of Chemistry, 2015).

[34] S. S. Zhang, K. Xu, and T. R. Jow, "Electrochemical impedance study on the low temperature of Li-ion batteries," *Electrochim. Acta* **49**, 1057–1061 (2004).

[35] M. R. Arcila-Velez, J. Zhu, A. Childress, M. Karakaya, R. Podila, A. M. Rao, and M. E. Roberts, "Roll-to-roll synthesis of vertically aligned carbon nanotube electrodes for electrical double layer capacitors," *Nano Energy* **8**, 9–16 (Elsevier, 2014).

[36] M. Karakaya, J. Zhu, A. J. Raghavendra, R. Podila, S. G. Parler, J. P. Kaplan, and A. M. Rao, "Roll-to-roll production of spray coated N-doped carbon nanotube electrodes for supercapacitors," *Appl. Phys. Lett.* **105**, 2012–2016 (2014).

[37] P. Verma, P. Maire, and P. Novák, "A review of the features and analyses of the solid electrolyte interphase in Li-ion batteries," *Electrochim. Acta* **55**, 6332–6341 (2010).

[38] J. F. McCann and S. P. S. Badwal, "Equivalent Circuit Analysis of the Impedance

Response of Semiconductor/Electrolyte/Counterelectrode Cells," *J. Electrochem. Soc.* **129**, 551–559 (The Electrochemical Society, 1982).

[39] I. Epelboin, M. Keddam, and H. Takenouti, "Use of impedance measurements for the determination of the instant rate of metal corrosion," *J. Appl. Electrochem.* **2**, 71–79 (Kluwer Academic Publishers).

[40] W. J. Lorenz and F. Mansfeld, "Determination of corrosion rates by electrochemical DC and AC methods," *Corros. Sci.* **21**, 647–672 (Pergamon, 1981).

[41] I. Epelboin, M. Joussellin, and R. Wiart, "Impedance measurements for nickel deposition in sulfate and chloride electrolytes," *J. Electroanal. Chem. Interfacial Electrochem.* **119**, 61–71 (Elsevier, 1981).

[42] D. R. Franceschetti and J. R. Macdonald, "Small-Signal A-C Response Theory for Electrochromic Thin Films," *J. Electrochem. Soc. Electrochem. Sci. Technol.* **129**, 551–559 (1982).

[43] M. Etman, C. Koehler, and R. Parsons, "A pulse method for the study of the semiconductor-electrolyte interface," *J. Electroanal. Chem. Interfacial Electrochem.* **130**, 57–66 (Elsevier, 1981).

[44] A. Smekal, "Zur Quantentheorie der Dispersion," *Naturwissenschaften* **11**, 873–875 (Springer-Verlag, 1923).

[45] C. V. RAMAN and K. S. KRISHNAN, "The Optical Analogue of the Compton Effect," *Nature* **121**, 711–711 (1928).

[46] R. Rao, "Raman Spectroscopic Evidence for Anharmonic Phonon Lifetimes and Blueshifts in 1D Structures," *All Diss.* **73** (2007).

[47] L. M. Malard, M. A. Pimenta, G. Dresselhaus, and M. S. Dresselhaus, "Raman spectroscopy in graphene," *Phys. Rep.* **473**, 51–87 (2009).

[48] M. S. Dresselhaus, A. Jorio, and R. Saito, "Characterizing Graphene, Graphite, and Carbon Nanotubes by Raman Spectroscopy," *Annu. Rev. Condens. Matter Phys.* **1**, 89–108 (2010).

[49] M. S. Dresselhaus, G. Dresselhaus, R. Saito, and A. Jorio, "Raman spectroscopy of carbon nanotubes," *Phys. Rep.* **409**, 47–99 (2005).

[50] M. S. Dresselhaus, G. Dresselhaus, A. Jorio, A. G. Souza Filho, and R. Saito, "Raman spectroscopy on isolated single wall carbon nanotubes," *Carbon N. Y.* **40**, 2043–2061 (2002).

[51] L. G. Cançado, K. Takai, T. Enoki, M. Endo, Y. A. Kim, H. Mizusaki, A. Jorio, L. N. Coelho, R. Magalhães-Paniago, et al., "General equation for the determination of the crystallite size L[sub a] of nanographite by Raman spectroscopy," *Appl. Phys. Lett.* **88**, 163106 (AIP Publishing, 2006).

[52] R. Rao, R. Podila, R. Tsuchikawa, J. Katoch, D. Tishler, A. M. Rao, and M. Ishigami, "Effects of layer stacking on the combination Raman modes in graphene.,"

ACS Nano **5**, 1594–1599 (American Chemical Society, 2011).

[53] R. Saito, A. Jorio, A. G. Souza Filho, G. Dresselhaus, M. S. Dresselhaus, and M. A. Pimenta, "Probing Phonon Dispersion Relations of Graphite by Double Resonance Raman Scattering," *Phys. Rev. Lett.* **88**, 27401 (American Physical Society, 2001).

[54] P. Tan, C. Hu, J. Dong, W. Shen, and B. Zhang, "Polarization properties, high-order Raman spectra, and frequency asymmetry between Stokes and anti-Stokes scattering of Raman modes in a graphite whisker," *Phys. Rev. B* **64**, 214301 (American Physical Society, 2001).

[55] C. Liu, Z. Yu, D. Neff, A. Zhamu, and B. Z. Jang, "Graphene-Based Supercapacitor with an Ultrahigh Energy Density," *Nano Lett.* **10**, 4863–4868 (2010).

[56] M. D. Stoller, S. Park, Y. Zhu, J. An, and R. S. Ruoff, "Graphene-based ultracapacitors.," *Nano Lett.* **8**, 3498–3502 (2008).

[57] Y. Zhu, S. Murali, M. D. Stoller, K. J. Ganesh, W. Cai, P. J. Ferreira, A. Pirkle, R. M. Wallace, K. A. Cychosz, et al., "Carbon-Based Supercapacitors Produced by Activation of Graphene," *Science (80-.).* **332**, 1537–1541 (2011).

[58] Y. Wang, Z. Shi, Y. Huang, Y. Ma, C. Wang, M. Chen, and Y. Chen, "Supercapacitor Devices Based on Graphene Materials," *J. Phys. Chem. C* **113**, 13103–13107 (American Chemical Society, 2009).

[59] R. Narayanan, H. Yamada, M. Karakaya, R. Podila, A. M. Rao, and P. R. Bandaru, "Modulation of the Electrostatic and Quantum Capacitances of Few Layered Graphenes through Plasma Processing.," *Nano Lett.* **15**, 3067–3072 (2015).

[60] H. Yamada and P. R. Bandaru, "Limits to the magnitude of capacitance in carbon nanotube array electrode based electrochemical capacitors," *Appl. Phys. Lett.* **102**, 1–5 (2013).

[61] L. L. Zhang, X. Zhao, H. Ji, M. D. Stoller, L. Lai, S. Murali, S. Mcdonnell, B. Cleveger, R. M. Wallace, et al., "Nitrogen doping of graphene and its effect on quantum capacitance, and a new insight on the enhanced capacitance of N-doped carbon," *Energy Environ. Sci.* **5**, 9618 (2012).

[62] B. Anand, M. Karakaya, G. Prakash, S. S. Sankara Sai, R. Philip, P. Ayala, A. Srivastava, A. K. Sood, A. M. Rao, et al., "Dopant-configuration controlled carrier scattering in graphene," *RSC Adv.* **5**, 59556–59563 (Royal Society of Chemistry, 2015).

[63] S. Radic, N. K. Geitner, R. Podila, A. Käkinen, P. Chen, P. C. Ke, and F. Ding, "Competitive Binding of Natural Amphiphiles with Graphene Derivatives," *Sci. Rep.* **3**, 2273 (Macmillan Publishers Limited. All rights reserved, 2013).

[64] B. Anand, M. Karakaya, G. Prakash, S. S. Sankara Sai, R. Philip, P. Ayala, A. Srivastava, A. K. Sood, A. M. Rao, et al., "Dopant-configuration controlled carrier scattering in graphene," *RSC Adv.* **5**, 59556–59563 (Royal Society of Chemistry, 2015).

[65] Y. Shim and H. J. Kim, "Nanoporous Carbon Supercapacitors in an Ionic Liquid: A Computer Simulation Study," *ACS Nano* **4**, 2345–2355 (American Chemical Society, 2010).

[66] P. Wu, J. Huang, V. Meunier, B. G. Sumpter, and R. Qiao, "Complex Capacitance Scaling in Ionic Liquids-Filled Nanopores," *ACS Nano* **5**, 9044–9051 (American Chemical Society, 2011).

[67] G. Feng and P. T. Cummings, "Supercapacitor capacitance exhibits oscillatory behavior as a function of nanopore size," *J. Phys. Chem. Lett.* **2**, 2859–2864 (2011).

[68] C. Largeot, C. Portet, J. Chmiola, P. L. Taberna, Y. Gogotsi, and P. Simon, "Relation between the ion size and pore size for an electric double-layer capacitor," *J. Am. Chem. Soc.* **130**, 2730–2731 (2008).

[69] C. Merlet, C. Péan, B. Rotenberg, P. a Madden, B. Daffos, P.-L. Taberna, P. Simon, and M. Salanne, "Highly confined ions store charge more efficiently in supercapacitors.," *Nat. Commun.* **4**, 2701 (2013).

[70] P. Simon and Y. Gogotsi, "Materials for electrochemical capacitors.," *Nat. Mater.* **7**, 845–854 (2008).

[71] J. Chmiola, G. Yushin, Y. Gogotsi, C. Portet, P. Simon, and P. L. Taberna, "Anomalous Increase in Carbon Capacitance at Pore Sizes Less Than 1 Nanometer," *Science (80-.).* **313**, 1760–1763 (2006).

[72] L. Xing, J. Vatamanu, O. Borodin, and D. Bedrov, "On the atomistic nature of capacitance enhancement generated by ionic liquid electrolyte confined in subnanometer pores," *J. Phys. Chem. Lett.* **4**, 132–140 (2013).

[73] L. Liu, X. Yue, J. Zhao, Q. Cheng, and J. Tang, "Graphene antidot lattices as potential electrode materials for supercapacitors," *Phys. E Low-dimensional Syst. Nanostructures* **69**, 316–321 (2015).

[74] L. G. Cançado, A. Jorio, E. H. M. Ferreira, F. Stavale, C. A. Achete, R. B. Capaz, M. V. O. Moutinho, A. Lombardo, T. S. Kulmala, et al., "Quantifying defects in graphene via Raman spectroscopy at different excitation energies.," *Nano Lett.* **11**, 3190–3196 (American Chemical Society, 2011).

[75] L. G. Cançado, K. Takai, T. Enoki, M. Endo, Y. A. Kim, H. Mizusaki, A. Jorio, L. N. Coelho, R. Magalhães-Paniago, et al., "General equation for the determination of the crystallite size L[sub a] of nanographite by Raman spectroscopy," *Appl. Phys. Lett.* **88**, 163106 (AIP Publishing, 2006).

[76] G. Luo, L. Liu, J. Zhang, G. Li, B. Wang, and J. Zhao, "Hole defects and nitrogen doping in graphene: implication for supercapacitor applications.," *ACS Appl. Mater. Interfaces* **5**, 11184–11193 (American Chemical Society, 2013).

[77] J. Gamby, P. L. Taberna, P. Simon, J. F. Fauvarque, and M. Chesneau, "Studies and characterisations of various activated carbons used for carbon/carbon supercapacitors," *J. Power Sources* **101**, 109–116 (2001).

[78] Z. Jiang, Z. Jiang, X. Tian, and W. Chen, "Amine-functionalized holey graphene as a highly active metal-free catalyst for the oxygen reduction reaction," *J. Mater. Chem. A* **2**, 441–450 (2014).

[79] M. M. Sk and C. Y. Yue, "Layer-by-layer (LBL) assembly of graphene with p-phenylenediamine (PPD) spacer for high performance supercapacitor applications," *RSC Adv.* **4**, 19908–19915 (2014).

[80] K. Zhang, L. L. Zhang, X. S. Zhao, and J. Wu, "Graphene/Polyaniline Nanofiber Composites as Supercapacitor Electrodes," *Chem. Mater.* **22**, 1392–1401 (2010).

[81] D. Yu, K. Goh, H. Wang, L. Wei, W. Jiang, Q. Zhang, L. Dai, and Y. Chen, "Scalable synthesis of hierarchically structured carbon nanotube-graphene fibres for capacitive energy storage," *Nat Nano* **9**, 555–562 (Nature Publishing Group, 2014).

[82] J. J. Yoo, K. Balakrishnan, J. Huang, V. Meunier, B. G. Sumpter, A. Srivastava, M. Conway, A. L. M. Reddy, J. Yu, et al., "Ultrathin planar graphene supercapacitors.," *Nano Lett.* **11**, 1423–1427 (2011).

[83] Z. Wu, K. Parvez, X. Feng, and K. Müllen, "Graphene-based in-plane micro-supercapacitors with high power and energy densities," *Nat Commun* **4** (Nature Publishing Group, a division of Macmillan Publishers Limited. All Rights Reserved., 2013).

[84] H. Y. Jung, M. B. Karimi, M. G. Hahm, P. M. Ajayan, and Y. J. Jung, "Transparent, flexible supercapacitors from nano-engineered carbon films.," *Sci. Rep.* **2**, 773 (Nature Publishing Group, 2012).

[85] Z. Chen, W. Ren, L. Gao, B. Liu, S. Pei, and H.-M. Cheng, "Three-dimensional flexible and conductive interconnected graphene networks grown by chemical vapour deposition.," *Nat. Mater.* **10**, 424–428 (Nature Publishing Group, 2011).

[86] M. J. Allen, V. C. Tung, and R. B. Kaner, "Honeycomb carbon: A review of graphene," *Chem. Rev.* **110**, 132–145 (2010).

[87] Z. H. Ni, L. a. Ponomarenko, R. R. Nair, R. Yang, S. Anissimova, I. V. Grigorieva, F. Schedin, P. Blake, Z. X. Shen, et al., "On resonant scatterers as a factor limiting carrier mobility in graphene," *Nano Lett.* **10**, 3868–3872 (2010).

[88] C. R. Dean, a F. Young, I. Meric, C. Lee, L. Wang, S. Sorgenfrei, K. Watanabe, T. Taniguchi, P. Kim, et al., "Boron nitride substrates for high-quality graphene electronics.," *Nat. Nanotechnol.* **5**, 722–726 (Nature Publishing Group, 2010).

[89] L. E. Hueso, J. M. Pruneda, V. Ferrari, G. Burnell, J. P. Valdés-Herrera, B. D. Simons, P. B. Littlewood, E. Artacho, A. Fert, et al., "Transformation of spin information into large electrical signals using carbon nanotubes.," *Nature* **445**, 410–413 (2007).

[90] K. Tsukagoshi, B. W. Alphenaar, and H. Ago, "Coherent transport of electron spin in a ferromagnetically contacted carbon nanotube," 572–574 (1999).

[91] J. W. McClure, “Diamagnetism of Graphite,” *Phys. Rev.* **104**, 666–671 (American Physical Society, 1956).

[92] P. Esquinazi, A. Setzer, R. Höhne, C. Semmelhack, Y. Kopelevich, D. Spemann, T. Butz, B. Kohlstrunk, and M. Lösche, “Ferromagnetism in oriented graphite samples,” *Phys. Rev. B* **66**, 24429 (American Physical Society, 2002).

[93] P. O. Lehtinen, A. S. Foster, Y. Ma, A. V Krasheninnikov, and R. M. Nieminen, “Irradiation-induced magnetism in graphite: a density functional study.,” *Phys. Rev. Lett.* **93**, 187202 (American Physical Society, 2004).

[94] O. V Yazyev, “Magnetism in disordered graphene and irradiated graphite.,” *Phys. Rev. Lett.* **101**, 37203 (American Physical Society, 2008).

[95] K. Sawada, F. Ishii, M. Saito, S. Okada, and T. Kawai, “Phase control of graphene nanoribbon by carrier doping: appearance of noncollinear magnetism.,” *Nano Lett.* **9**, 269–272 (American Chemical Society, 2009).

[96] K. Wakabayashi, M. Fujita, H. Ajiki, and M. Sigrist, “Electronic and magnetic properties of nanographite ribbons,” *Phys. Rev. B* **59**, 8271–8282 (American Physical Society, 1999).

[97] K. Kusakabe and M. Maruyama, “Magnetic nanographite,” *Phys. Rev. B* **67**, 92406 (American Physical Society, 2003).

[98] T. L. Makarova, B. Sundqvist, R. Höhne, P. Esquinazi, Y. Kopelevich, P. Scharff, V. A. Davydov, L. S. Kashevarova, and A. V Rakhmanina, “Magnetic carbon.,” *Nature* **413**, 716–718 (2001).

[99] A. V. Rode, E. G. Gamaly, A. G. Christy, J. G. Fitz Gerald, S. T. Hyde, R. G. Elliman, B. Luther-Davies, A. I. Veinger, J. Androulakis, et al., “Unconventional magnetism in all-carbon nanofoam,” *Phys. Rev. B* **70**, 54407 (American Physical Society, 2004).

[100] H. Ohldag, T. Tyliszczak, R. Höhne, D. Spemann, P. Esquinazi, M. Ungureanu, and T. Butz, “pi-electron ferromagnetism in metal-free carbon probed by soft x-ray dichroism.,” *Phys. Rev. Lett.* **98**, 187204 (American Physical Society, 2007).

[101] A. H. Castro Neto, N. M. R. Peres, K. S. Novoselov, and A. K. Geim, “The electronic properties of graphene,” *Rev. Mod. Phys.* **81**, 109–162 (American Physical Society, 2009).

[102] D. Soriano, F. Muñoz-Rojas, J. Fernández-Rossier, and J. J. Palacios, “Hydrogenated graphene nanoribbons for spintronics,” *Phys. Rev. B* **81**, 165409 (American Physical Society, 2010).

[103] F. J. Culchac, A. Latgé, and A. T. Costa, “Spin waves in zigzag graphene nanoribbons and the stability of edge ferromagnetism,” *New J. Phys.* **13**, 33028 (IOP Publishing, 2011).

[104] H. Feldner, Z. Y. Meng, T. C. Lang, F. F. Assaad, S. Wessel, and A. Honecker,

"Dynamical signatures of edge-state magnetism on graphene nanoribbons.," *Phys. Rev. Lett.* **106**, 226401 (American Physical Society, 2011).

[105] Y.-W. Son, M. L. Cohen, and S. G. Louie, "Half-metallic graphene nanoribbons.," *Nature* **444**, 347–349 (2006).

[106] O. V Yazyev, "Emergence of magnetism in graphene materials and nanostructures," *Reports Prog. Phys.* **73**, 56501 (IOP Publishing, 2010).

[107] M. Sepioni, R. R. Nair, S. Rablen, J. Narayanan, F. Tuna, R. Winpenny, A. K. Geim, and I. V Grigorieva, "Limits on intrinsic magnetism in graphene.," *Phys. Rev. Lett.* **105**, 207205 (American Physical Society, 2010).

[108] Y. Wang, Y. Huang, Y. Song, X. Zhang, Y. Ma, J. Liang, and Y. Chen, "Room-temperature ferromagnetism of graphene.," *Nano Lett.* **9**, 220–224 (American Chemical Society, 2009).

[109] H. S. S. R. Matte, K. S. Subrahmanyam, and C. N. R. Rao, "Novel Magnetic Properties of Graphene: Presence of Both Ferromagnetic and Antiferromagnetic Features and Other Aspects," *J. Phys. Chem. C* **113**, 9982–9985 (American Chemical Society, 2009).

[110] S. S. Rao, S. N. Jammalamadaka, A. Stesmans, V. V Moshchalkov, J. van Tol, D. V Kosynkin, A. Higginbotham-Duque, and J. M. Tour, "Ferromagnetism in graphene nanoribbons: split versus oxidative unzipped ribbons.," *Nano Lett.* **12**, 1210–1217 (American Chemical Society, 2012).

[111] R. Podila, W. Queen, A. Nath, J. T. Arantes, A. L. Schoenhalz, A. Fazzio, G. M. Dalpian, J. He, S. J. Hwu, et al., "Origin of FM ordering in pristine micro- and nanostructured ZnO.," *Nano Lett.* **10**, 1383–1386 (American Chemical Society, 2010).

[112] B. B. Straumal, A. A. Mazilkin, S. G. Protasova, A. A. Myatiev, P. B. Straumal, G. Schütz, P. A. van Aken, E. Goering, and B. Baretzky, "Magnetization study of nanograined pure and Mn-doped ZnO films: Formation of a ferromagnetic grain-boundary foam," *Phys. Rev. B* **79**, 205206 (American Physical Society, 2009).

[113] T. Tietze, P. Audehm, Y.-C. Chen, G. Schütz, B. B. Straumal, S. G. Protasova, A. A. Mazilkin, P. B. Straumal, T. Prokscha, et al., "Interfacial dominated ferromagnetism in nanograined ZnO: a μSR and DFT study.," *Sci. Rep.* **5**, 8871 (Nature Publishing Group, 2015).

[114] S. G. Protasova, B. B. Straumal, A. A. Mazilkin, S. V. Stakhanova, P. B. Straumal, and B. Baretzky, "Increase of Fe solubility in ZnO induced by the grain boundary adsorption," *J. Mater. Sci.* **49**, 4490–4498 (2014).

[115] P. E. Blöchl, "Projector augmented-wave method," *Phys. Rev. B* **50**, 17953–17979 (American Physical Society, 1994).

[116] G. Kresse, "From ultrasoft pseudopotentials to the projector augmented-wave method," *Phys. Rev. B* **59**, 1758–1775 (American Physical Society, 1999).

[117] G. Kresse, "Efficient iterative schemes for ab initio total-energy calculations using a plane-wave basis set," *Phys. Rev. B* **54**, 11169–11186 (American Physical Society, 1996).

[118] G. Kresse and J. Furthmüller, "Efficiency of ab-initio total energy calculations for metals and semiconductors using a plane-wave basis set," *Comput. Mater. Sci.* **6**, 15–50 (1996).

[119] J. P. Perdew, K. Burke, and M. Ernzerhof, "Generalized Gradient Approximation Made Simple," *Phys. Rev. Lett.* **77**, 3865–3868 (American Physical Society, 1996).

[120] E. Z. Kurmaev, A. V. Galakhov, A. Moewes, S. Moehlecke, and Y. Kopelevich, "Interlayer conduction band states in graphite-sulfur composites," *Phys. Rev. B* **66**, 193402 (American Physical Society, 2002).

[121] B. C. Zhao, Y. Q. Ma, W. H. Song, and Y. P. Sun, "Magnetization steps in the phase separated manganite La0.275Pr0.35Ca0.375MnO3," *Phys. Lett. A* **354**, 472–476 (2006).

[122] Y. Ma, P. O. Lehtinen, A. S. Foster, and R. M. Nieminen, "Magnetic properties of vacancies in graphene and single-walled carbon nanotubes," *New J. Phys.* **6**, 68–68 (IOP Publishing, 2004).

[123] A. A. El-Barbary, R. H. Telling, C. P. Ewels, M. I. Heggie, and P. R. Briddon, "Structure and energetics of the vacancy in graphite," *Phys. Rev. B* **68**, 144107 (American Physical Society, 2003).

[124] H. Park, A. Wadehra, J. W. Wilkins, and A. H. Castro Neto, "Spin-polarized electronic current induced by sublattice engineering of graphene sheets with boron/nitrogen," *Phys. Rev. B* **87**, 85441 (American Physical Society, 2013).

[125] H. Park, A. Wadehra, J. W. Wilkins, and A. H. Castro Neto, "Magnetic states and optical properties of single-layer carbon-doped hexagonal boron nitride," *Appl. Phys. Lett.* **100**, 253115 (AIP Publishing, 2012).

[126] F. Wu, E. Kan, H. Xiang, S.-H. Wei, M.-H. Whangbo, and J. Yang, "Magnetic states of zigzag graphene nanoribbons from first principles," *Appl. Phys. Lett.* **94**, 223105 (AIP Publishing, 2009).

[127] L. Chen, L. Guo, Z. Li, H. Zhang, J. Lin, J. Huang, S. Jin, and X. Chen, "Towards intrinsic magnetism of graphene sheets with irregular zigzag edges.," *Sci. Rep.* **3**, 2599 (Nature Publishing Group, 2013).

[128] S.-Q. Zhao, Y. Lü, W.-G. Lü, W.-J. Liang, and E.-G. Wang, "Modulating magnetism of nitrogen-doped zigzag graphene nanoribbons," *Chinese Phys. B* **23**, 67305 (IOP Publishing, 2014).

[129] R. C. Weast, Ed., *CRC Handbook of Chemistry and Physics*, 63rd ed. (CRC Press LLC, 1984).

[130] A. C. Ferrari and D. M. Basko, "Raman spectroscopy as a versatile tool for studying

the properties of graphene.," *Nat. Nanotechnol.* **8**, 235–246 (Nature Publishing Group, a division of Macmillan Publishers Limited. All Rights Reserved., 2013).

[131] A. Jorio, M. S. Dresselhaus, R. Saito, and G. Dresselhaus, *Raman Spectroscopy in Graphene Related Systems* (Wiley-VCH, 2011).

[132] R. Podila, R. Rao, R. Tsuchikawa, M. Ishigami, and A. M. Rao, "Raman spectroscopy of folded and scrolled graphene.," *ACS Nano* **6**, 5784–5790 (American Chemical Society, 2012).

[133] C. Thomsen and S. Reich, "Double resonant raman scattering in graphite," *Phys. Rev. Lett.* **85**, 5214–5217 (American Physical Society, 2000).

[134] L. M. Malard, M. A. Pimenta, G. Dresselhaus, and M. S. Dresselhaus, "Raman spectroscopy in graphene," *Phys. Rep.* **473**, 51–87 (2009).

[135] R. Saito, A. Jorio, A. G. Souza Filho, G. Dresselhaus, M. S. Dresselhaus, and M. A. Pimenta, "Probing phonon dispersion relations of graphite by double resonance Raman scattering.," *Phys. Rev. Lett.* **88**, 27401 (American Physical Society, 2002).

[136] R. J. Nemanich and S. A. Solin, "First- and second-order Raman scattering from finite-size crystals of graphite," *Phys. Rev. B* **20**, 392–401 (American Physical Society, 1979).

[137] P. Tan, Y. Deng, and Q. Zhao, "Temperature-dependent Raman spectra and anomalous Raman phenomenon of highly oriented pyrolytic graphite," *Phys. Rev. B* **58**, 5435–5439 (American Physical Society, 1998).

[138] T. Shimada, T. Sugai, C. Fantini, M. Souza, L. G. Cançado, A. Jorio, M. A. Pimenta, R. Saito, A. Grüneis, et al., "Origin of the 2450cm−1 Raman bands in HOPG, single-wall and double-wall carbon nanotubes," *Carbon N. Y.* **43**, 1049–1054 (2005).

[139] D. L. Mafra, G. Samsonidze, L. M. Malard, D. C. Elias, J. C. Brant, F. Plentz, E. S. Alves, and M. A. Pimenta, "Determination of LA and TO phonon dispersion relations of graphene near the Dirac point by double resonance Raman scattering," *Phys. Rev. B* **76**, 233407 (American Physical Society, 2007).

[140] P. T. Araujo, D. L. Mafra, K. Sato, R. Saito, J. Kong, and M. S. Dresselhaus, "Phonon self-energy corrections to nonzero wave-vector phonon modes in single-layer graphene.," *Phys. Rev. Lett.* **109**, 46801 (American Physical Society, 2012).

[141] P. May, M. Lazzeri, P. Venezuela, F. Herziger, G. Callsen, J. S. Reparaz, A. Hoffmann, F. Mauri, and J. Maultzsch, "Signature of the two-dimensional phonon dispersion in graphene probed by double-resonant Raman scattering," *Phys. Rev. B* **87**, 75402 (American Physical Society, 2013).

[142] Z. Luo, C. Cong, J. Zhang, Q. Xiong, and T. Yu, "The origin of sub-bands in the Raman D-band of graphene," *Carbon N. Y.* **50**, 4252–4258 (2012).

[143] X. Li, W. Cai, J. An, S. Kim, J. Nah, D. Yang, R. Piner, A. Velamakanni, I. Jung, et al., "Large-area synthesis of high-quality and uniform graphene films on copper

foils.," *Science* **324**, 1312–1314 (American Association for the Advancement of Science, 2009).

[144] D. L. Mafra, E. A. Moujaes, S. K. Doorn, H. Htoon, R. W. Nunes, and M. A. Pimenta, "A study of inner process double-resonance Raman scattering in bilayer graphene," *Carbon N. Y.* **49**, 1511–1515 (2011).

[145] P. Venezuela, M. Lazzeri, and F. Mauri, "Theory of double-resonant Raman spectra in graphene: Intensity and line shape of defect-induced and two-phonon bands," *Phys. Rev. B* **84**, 35433 (American Physical Society, 2011).

[146] H. H. Burke and I. P. Herman, "Temperature dependence of Raman scattering in Ge 1 − x Si x alloys," *Phys. Rev. B* **48**, 15016–15024 (American Physical Society, 1993).

[147] I. Calizo, A. A. Balandin, W. Bao, F. Miao, and C. N. Lau, "Temperature Dependence of the Raman Spectra of Graphene and Graphene Multilayers," *Nano Lett.* **7**, 2645–2649 (2007).